Physical Mechanisms governing
Self-Excited Pressure Oscillations in Francis Turbines

PAR

Andres MÜLLER

EPFL

ÉCOLE POLYTECHNIQUE
FÉDÉRALE DE LAUSANNE

Suisse
2014

The cleverest of all, in my opinion,
is the man who calls himself a fool at least once a month.
— Fyodor M. Dostoyevsky

Acknowledgements

Acknowledgements

and the test rig included in this work. Georges Crittin, with his tremendous knowledge of the test facilities and the instrumentation, was always my first address after each use of the panic button on the test rig. Special thanks go to Isabelle Stoudmann-Schmutz for administrative support and her kindness. Finally, this document would not exist without the support of the EPFL doctoral school, especially Cécile Taverney at EDEY and Sandra Roux at the registrar's office.

Je me permets de rédiger cette partie "inofficielle" en français. Tout d'abord, je remercie mes parents, Marie-Catherine et Peter Müller-Bouquet. Je n'oublierai jamais leur soutien inconditionnel, quelque soit mon choix de carrière. Je remercie aussi le reste de ma famille, Jan et Béatrice avec Aaron, Benjamin et Matilda, ainsi que Per et Noëmi pour leur patience, leurs encouragements et les bons moments partagés lors des différentes rencontres familiales.

Pour mon travail de recherche, j'ai beaucoup profité de l'expérience des anciens du laboratoire, comme le Dr Christophe Nicolet. Je tiens à le remercier sincèrement pour ses nombreux conseils, sa disponibilité et évidemment les 1, 2, 3 ... 15 bières.

Passons maintenant à mes chers et chères collègues au laboratoire. Comme je ne sais pas par qui commencer, je procèderai donc par un ordre plus ou moins chronologique. Quand je suis arrivé au LMH, toute une fine équipe que je connaissais des études à l'EPFL m'attendait déjà : les docteurs Olivier Pacot, Martino Reclari, Steven Roth et Marc Tinguely. Je remercie ces amis pour les moments agréables et arrosés durant tout le long de la thèse. Apparemment je parlais tellement fort au téléphone que j'ai fait fuir Olivier, qui était à côté de moi, jusqu'à l'autre bout de la terre. Nos weekends dans les quatre coins du Japon fûrent très agréables (les voyages de retour pas toujours autant que ça). Merci à Martino, le bricoleur surdoué, de nous avoir fait découvrir les grotto du Tessin avec Martina. Un grand merci à Steven pour nos nombreuses discussions durant les pauses et en dehors du travail, pour notre lutte commune contre la clope (on pouvait toujours compter sur l'autre pour une rechute) et pour son intégrité. Marc m'a toujours fasciné par son calme et par sa tenacité, que ce soit pour la recherche ou pour la noce. Il nous a tous couché à Stockholm. Nos "working dinners" me resteront toujours en mémoire. Il y a ensuite mon prédécesseur, Sébastien Alligné, ou papa Séb, qui a si bien préparé le terrain pour ma recherche et qui m'a beaucoup aidé par la suite grâce sa grande compétence dans le domaine. Je ne connais encore personne qui l'ait battu au bras de fer ou dans l'art du disc jockeying. Merci aussi à Cécile Münch-Alligné pour sa bonne humeur et sa patience quand on a forcé son mari à faire des détours avant de rentrer à la maison. Ensuite mon ami de 1005, Matthieu Dreyer. Quelle découverte. Merci de m'avoir accompagné dans la neige avec mon panneau de circulation, et lors de deux voyages au Japon. Merci aussi de m'avoir fait redécouvrir ma moitié Fribourgeoise. Je ne sais toujours pas si c'était une bonne chose ou pas. Merci Christian Landry d'avoir supporté les nombreuses blagues sur le Valais et pour ta disponibilité pour des questions sur les machines hydrauliques ou l'orthographe française. Merci Christian Vessaz de nous pousser à des exploits culinaires dans la cafét' du labo. Rappelle toi, la réponse est toujours oui. Je suis encore choqué que tu soies arrivé à nous

faire participer à un tir en campagne dans la Broye. Ça sera difficile d'oublier les premiers jours d'Arthur Favrel au laboratoire... Quelle entrée en service ! Nous devons absolument poursuivre notre projet littéraire. Merci aussi pour la préparation méticuleuse de la compagne expérimentale en 2013 avec Christian Landry. Merci à Vlad Hasmatuchi pour ses conseils et Ebrahim Jahanbakhsh pour avoir toléré le niveau sonore dans notre bureau. Je remercie beaucoup Keita Yamamoto pour son aide durant mon séjour à Osaka et je lui souhaite bonne chance pour sa thèse à Lausanne. Je souhaite aussi tout de bon aux "nouveaux" doctorants, Simon Pasche, Quentin Fabien, Outi Supponen et Elena Vagnoni, ainsi qu'au nouveau post-doc Loïc Andolfatto, que je remercie particulièrement pour m'avoir fait découvrir un petit bistro sympathique à Paris. Merci à Alberto Bullani pour son excellent travail durant son projet de master et l'approvisionnement en charcuterie tessinoise. Finalement, je remercie Georges, Alain et le Prof. Avellan pour un séjour aussi instructif qu'agréable au Chili, en particulier pour leur aide à San Fernando.

Un grand merci est aussi de rigueur pour mes amis en dehors du laboratoire pour m'avoir supporté durant ces 4 ans. Les weekends réguliers à Stockholm et les soirées télé avec Till Junge fûrent un excellent contraste. Un grand merci aussi à Till et à Sandra pour leur hospitalité quand je marchais avec des béquilles. Merci à Fabian Jabas pour les nombreux souvenirs de voyage et les bons repas dans 12 pays sur 3 continents. Merci Markus & Sawsan Studer et Karolina Durrer pour votre amitié. Merci à toute l'équipe du Festival Balélec pour une expérience extraordinaire durant mon passage dans le comité d'organisation. Merci à mes amis de voyage Will Ooi et Penelope Marles, en particulier pour leur accueil en Australie. Merci à Leefke & Julien Grosjean de m'avoir aidé à conserver un lien avec la Suède et en particulier pour les vacances au stugan. Merci à Axel Brunk, Jeremy Binder, Pierre-Alain Blanc, Lucas Jaquet et Mario Schwertberger pour des soirées (presque) inoubliables à Lausanne, Fribourg, en Belgique et en Bavière.

Sapporo, 16 mai 2014 A. M.

Abstract

The importance of renewable energy sources for the electrical power supply has grown rapidly in the past decades. Their often unpredictable nature however poses a threat to the stability of the existing electric grid. Hydroelectric powerplants play an important role in regulating the integration of renewable energy sources into the network by supplying on-demand load balancing as well as primary and secondary power network control. Therefore, the operating ranges of hydraulic machines has to be continuously extended, which potentially produces undesirable flow phenomena involving cavitation. An example is the formation of a gaseous volume in the swirling flow leaving a Francis turbine runner at off-design operating conditions. At high load, this so called vortex rope is shaped axisymmetrically and may enter a self-excited oscillation, measurable through significant fluctuations of the pressure throughout the system and the mechanical torque transferred to the generator. The main objective of the present work is the identification of the physical mechanisms governing this self-sustained, unstable behavior by measurement. Furthermore, the key parameters of numerical approaches using one-dimensional hydroacoustic flow models or CFD require experimental validation. For this purpose, the measurements provide a comprehensive data base of various flow and system parameters at varying operating conditions.

Two test cases are studied, a small scale hydraulic circuit with a micro-turbine as well as a reduced scale physical model of an existing Francis turbine. On the first test case, the study of the flow rate fluctuations up- and downstream of the oscillating vortex rope in the draft tube, together with the volume of the cavity, revealed the destabilizing effect of the flow swirl in the draft tube inlet. The second test case accurately simulates the behavior of an actual hydraulic power plant. Investigations range from a local study of the flow field in the draft tube cone by means of LDV, PIV, high speed visualization and wall pressure measurements to a global analysis, considering the response of the hydraulic and mechanical system to the excitation by the vortex rope oscillation. Among the main observations is a periodical variation of the flow swirl in the draft tube, synchronized with the pressure oscillations. This is likely to be caused by a cyclically appearing volume of cavitation on the runner blades, modifying the relative flow angle at the outlet. The interaction of the blade cavitation and the vortex rope oscillation via the flow swirl is found to play a crucial role in the occurrence of self-excited pressure oscillations in Francis turbines.

Keywords: Francis turbine, full load, pressure fluctuations, cavitation, vortex rope, swirl, self-oscillation, experimental investigation.

Résumé

Les centrales hydroélectriques jouent un rôle important dans l'intégration des sources d'énergie renouvelables dans le réseau électrique existant en garantissant sa stabilité. L'accomplissement de cette fonction nécessite une extension continue du domaine de fonctionnement des machines hydrauliques. Les régimes en dehors du point de meilleur rendement sont cependant caractérisés par des champs de vitesse et de pression inhomogènes dans le diffuseur en sortie de roue, avec une forte composante tournante. La naissance d'écoulements cavitants est ainsi souvent observée. A forte charge, cette cavitation prend la forme d'un volume de vapeur axisymétrique attaché au moyeu de la roue et, selon les conditions de fonctionnement, la cavité peut se mettre à pulser et entrer en auto-oscillation avec le système. Cette instabilité est accompagnée par de fortes pulsations de pression et de couple sur l'arbre de la roue, ce qui peut mettre en péril la stabilité de la machine et du réseau électrique auquel elle est connectée. Les mécanismes physiques liés à ce comportement instable ne sont, à cette date, pas entièrement connus. Ce travail consiste en l'établissement d'une base de données expérimentales permettant dans un premier temps de décrire le phénomène de manière quantitative. Les cas d'étude choisis sont un modèle réduit d'une turbine Francis ainsi qu'un cas-test simplifié avec une micro-turbine. Les résultats des mesures sur la micro-turbine permettent de suivre le comportement des paramètres hydroacoustiques nécessaires aux modèles monodimensionnels usuels pour simuler l'écoulement dans le diffuseur et valider certaines approches de modélisation. Sur le modèle réduit, le champ de vitesse en sortie de roue est décrit en détail avec des mesures locales de LDV, PIV et de pression aux parois. Dans une approche plus globale, la réponse du système hydraulique et mécanique à l'excitation créée par l'écoulement diphasique pulsant est étudiée. Une importante variation du flux du moment angulaire est mise en évidence, accompagnée de l'apparition et du collapse périodique des poches de cavitation sur l'extrados des aubes de la turbine. L'interaction entre cette cavitation sur les aubes et l'auto-oscillation de la cavité dans le cône du diffuseur est identifiée comme mécanisme clé dans l'apparition et le maintien de l'instabilité.

Mots-clés : Turbine Francis, forte charge, fluctuations de pression, cavitation, swirl, auto-oscillation, expérimental.

Nomenclature

Acronyms

BEP	**B**est **E**fficiency **P**oint
BSA	**B**urst **S**pectrum **A**nalyzer
DTFT	**D**iscrete-**T**ime **F**ourier **T**ransform
EPFL	**É**cole **p**olytechnique **f**édérale de **L**ausanne
FFT	**F**ast **F**ourier **T**ransform
fps	**f**rames **p**er **s**econd
LDA	**L**aser **D**oppler **A**nemometry
HA	**H**ydro**a**coustic
LDV	**L**aser **D**oppler **V**elocimetry
NRE	**N**ew and **R**enewable **E**nergy
OP	**O**perating **P**oint
PCI	**P**eripheral **C**omponent **I**nterconnect
PIV	**P**article **I**mage **V**elocimetry
PXI	**P**CI e**X**tensions for **I**nstrumentation
ROI	**R**egion **o**f **I**nterest
rpm	**r**evolutions **p**er **m**inute
std	**st**andard **d**eviation
TTL	**T**ransistor-**T**ransistor **L**ogic

Subscripts

1	runner inlet reference section
$\bar{1}$	runner outlet reference section
c	cavity (vortex rope)
I	power unit high pressure reference section
$\bar{I}$	power unit low pressure reference section
$\bar{B}$	tail water reservoir reference section
m	mechanical
p	prototype
ref	power unit reference level (horizontal spiral case symmetry plane)

Latin letters

Cm	axial (meridional) velocity component	(m s^{-1})
Cu	tangential velocity component	(m s^{-1})
Cr	radial velocity component	(m s^{-1})
C_Q	mean discharge speed	(m s^{-1})
g	gravitational acceleration	(m s^{-2})
h	piezometric head; $h = z + p/(\rho g)$	(m)
n	runner rotational frequency	(Hz)
z	elevation	(m)
C_c	cavitation compliance; $C_c = \partial V_c / \partial h$	(m^2)
D	diameter	(m)
E	specific Energy; $E = g \cdot H = \Delta\left(\frac{p}{\rho} + gz\right)_{I-\bar{I}} + \frac{1}{2}\bar{Q}^2 \frac{1}{A_I^2 - A_{\bar{I}}^2}$	(J kg^{-1})
f	frequency	(Hz)
H_s	$z_{\text{ref}} - z_{\overline{B}}$	(m)
L	angular momentum	(J s)
N	runner speed	(min^{-1})
NPSE	net Positive Suction Energy; NPSE=$(p_b - p_v)/\rho - gH_s + \frac{1}{2}C_{\bar{I}}^2$	(J kg^{-1})
NPSH	net Positive Suction Head; NPSH=NPSE/g	(m)
p_b	downstream reservoir pressure	(Pa)
p_v	vapor pressure	(Pa)
Q	volumetric discharge or flow rate	(m^3 s^{-1})
R	radius	(m)
S	swirl number	(-)
T	torque	(Nm)
U	peripheral velocity	(m s^{-1})
V	volume	(m^3)

Greek letters

β	relative flow angle	(deg)
ρ	density	(kg m^{-3})
ω	angular velocity	(rad s^{-1})
χ	mass flow gain factor; $\chi = \partial V_c / \partial Q$	(s)

Non-dimensional variables

c_p	pressure factor; $c_p = (p - \overline{p})/(\rho E)$	(-)
Fr	Froude number; $Fr = \sqrt{H/D_{\bar{I}}}$	(-)
n_{ED}	speed factor; $n_{ED} = (n \cdot D)/\sqrt{E}$	(-)
Q_{ED}	discharge factor; $Q_{ED} = Q/(D^2\sqrt{E})$	(-)

φ	flow coefficient; $\varphi = Q/(\pi\omega R^3)$	(-)
ψ	energy coefficient; $\psi = 2E/(\omega^2 R^2)$	(-)
ν	specific speed; $\nu = \sqrt{\varphi}/\psi^{-(3/4)}$	(-)
σ	Thoma number or cavitation number; $\sigma = \text{NPSE}/E$	(-)

Contents

Contents

List of Figures

List of Tables

Introduction

0.1 Research context

Hydraulic powerplants provided 58.7% of Switzerland's total electricity production in 2012 [20]. Globally speaking, in 2012, an estimated 16.5% of the worldwide electricity production is attributed to hydropower. A share of 5.2% originated from other renewable energy sources and 78.3% came from fossil fuel and nuclear powerplants [21]. This distribution is subject to constant change, motivated by environmental concerns as well as shifting geological, economical and geopolitical realities. As a consequence, the installed renewable power capacity is on a constant rise, as documented in Table 2. Main technologies include solar and wind power, biomass & waste-to-energy, biofuels, geothermal and ocean energy. This development is often given a political frame through the definition of energy policies on a national and supranational level. To name one example, the European Union has recently defined a set of objectives under the name of the *2020 climate and energy package*. The latter targets a 20% reduction of the greenhouse gas emissions from 1990 levels, a raise of the renewable energy resources' share in the electricity consumption to 20% and an improvement of the energy efficiency of 20% [51]. In a similar effort, the Swiss government has defined the *Energy Perspectives 2050* [19], following the decision of the Federal Council from May 25, 2011, to gradually phase out nuclear energy as part of its new energy strategy.

Table 2: Selected indicators of renewable energy sources development from [21]

Year		2010	2011	2012
Renewable power capacity (without hydro)	GW	315	395	480
Hydropower capacity	GW	935	960	990
Total renewable power capacity	GW	1'250	1'355	1'470
Countries with policy targets	#	109	118	138
Annual investment in new renewable capacity	billion USD	227	279	244

In order to support and accelerate the development of renewable energy resources (NRE), their smooth integration into the existing power network has to be guaranteed. In the past, energy sources characterized by an unsteady, unpredictable output have been known to critically challenge the stability of the electrical grid. Typical examples are solar or wind power, which depend heavily on the weather conditions. Hydropower plants contribute decisively to the

mitigation of this issue by providing the necessary storage capacity needed for load balancing as well as primary and secondary frequency regulation capabilities. This goes however along with a continuous extension of the operating range of the hydraulic machines, causing the kind of undesired flow instabilities addressed in this work.

The present investigation concentrates on the high load or overload behavior of Francis turbines. The corresponding operating range is defined by flow rates which are higher than the value producing the highest efficiency of the turbine, called the Best Efficiency Point. Due to their adaptability to a wide range of site conditions in terms of head and discharge, Francis turbines cover the largest part of the installed hydropower capacity in the world. Owing their name to the British-American engineer James B. Francis in the 1840s, the most recent milestone in their development is the delivery of a 812 MW runner to the Xianjiaba Dam spanning the Jinsha river in China, representing the world's largest single unit output.

0.2 Off-design operation of hydraulic machines

At off-design operating conditions, the velocity field of the flow leaving the runner has, in addition to the axial component Cm in the main flow direction, also a tangential or swirling component Cu. This is illustrated in Figure 1 and Figure 2, defining the relative and absolute flow velocity vectors $\vec{W}_{\bar{1}}$ and $\vec{C}_{\bar{1}}$ at the runner outlet as well as the peripheral velocity $\vec{U}_{\bar{1}}$. The direction of the relative flow vector $\vec{W}_{\bar{1}}$ is set by the geometry of the runner blades. Depending on the load case, the tangential flow either rotates in the same or in the opposite direction of the runner. This swirl leads to an inhomogeneous pressure distribution in the draft tube cone, due to the fact that the fluid mass is being pushed towards the walls under the influence of centrifugal forces. When the pressure in the center of the cone reaches the vapor pressure p_v, the water locally evaporates and a cavitating vortex rope is formed.

At part load, the vortex rope is shaped like a corkscrew, wrapped around a recirculation zone in the center [45, 60]. At full load on the other hand, the cavity has a nearly axisymmetric shape along the draft tube centerline. Figure 3 shows a waterfall diagram with power spectral densities of the wall pressure fluctuations in the draft tube over a broad load range for the test case described in Section 1.1.1. The BEP is located at a discharge factor of $Q_{ED} = 0.2$, surrounded by a cavitation-free zone. The dominant contribution in the wall pressure signal comes from a periodic, forced precession movement of the vortex rope, which acts as an external excitation source. The resonance observed at $Q_{ED} = 0.166$, or at 82% of the discharge at the BEP, occurs when the frequency of the vortex rope precession matches the first hydroacoustic eigenfrequency of the system, as reported by Favrel *et al.* [18]. The pressure oscillations at full load are of self-excited nature, implying an independence from a periodic external excitation. Self-excited oscillations are also known as "self-oscillations", "auto-oscillations" or "self-sustained" and "self-induced" oscillations and arise from an interaction between the oscillator's motion and the attached power source, causing negative damping and feeding energy into the oscillation [31].

2
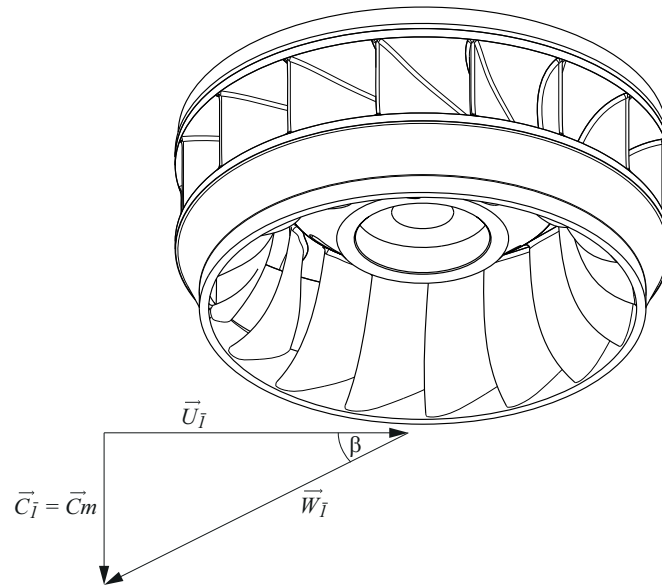
Figure 1: Definition of the velocity triangles at the outlet of a Francis turbine runner.
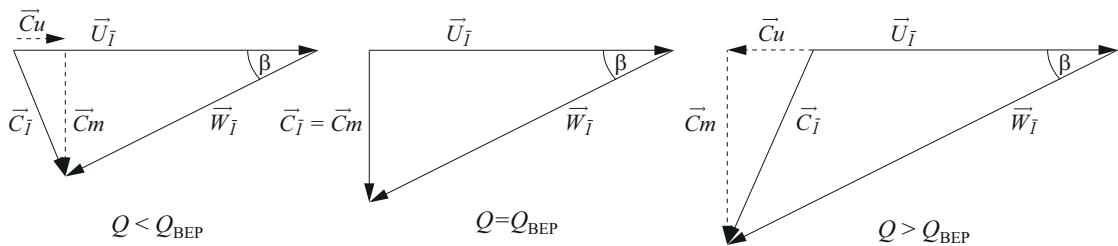
Figure 2: Velocity triangles in the draft tube for partial load, BEP and full load operation.

0.3 State of the art

Cavitation is a long known and well-studied phenomenon, occurring in a large variety of applications [22, 68]. Among the problems caused by its appearance in fluid machinery is the dynamic interaction with the surrounding system. In Francis turbines, a violent instability is observed at full load, exhibiting an oscillating vortex rope volume in the draft tube cone, alongside with self-excited pressure oscillations in the entire system. Extensive experimental investigations of this phenomenon, often referred to as pressure surge, were performed on reduced scale physical models by Prénat and Jacob between 1986 and 1996 [28, 29, 30, 52]. First reports of power swings in hydroelectric plants due to draft tube surges date however as far back as 1912, and the topic increasingly received attention from the 1930s onwards [53].

Efforts to develop analytical and numerical descriptions of the unsteady two-phase flow in industrial applications have their origin in the early 1960s, when a critical instability, called the POGO effect, was observed in several vehicles used for space flight, arising from the interaction of longitudinal structural vibration with the liquid propulsion system. The most important transient parameters for the dynamic modelling of the propulsion system were identified

3
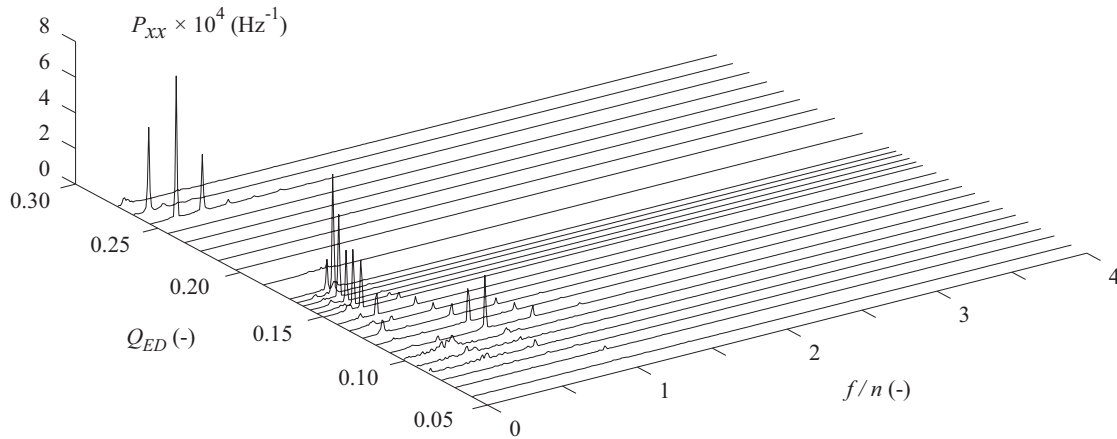
Figure 3: Power spectral densities of the pressure fluctuations in the draft tube cone of a Francis turbine at $\sigma = 0.11$ over a load range of 30% to 137%.

by Rubin [54], such as the compliance, describing the oscillatory source/sink behaviour of the pump due to the fluctuating cavity volume. Analytical solutions for the flow in the inducer and resulting values of the local and overall compliance are presented by Brennen and Acosta in 1973 [11], using quasi-steady free streamline cascade theory. In 1976, the same authors introduced a second parameter, called the mass flow gain factor χ, as part of a transfer function, relating the fluctuating pressure and mass flow rates at the inlet of a turbo pump to the same quantities at the outlet [10, 12]. This quantity, representing the change in the cavity volume with respect to the change in mass flow, was not only proven to be non-zero as previously assumed, but was attributed a major dynamic effect. In 1980 Braisted and Brennen [7] experimentally investigate the character of the excitation of the auto-oscillation by the cavitation in turbo pumps. They assessed the influence of the cavitation number σ and the flow coefficient φ, among other flow parameters at the inducer and the outlet, on the onset point and the dominant frequency of the auto-oscillation, reaching the conclusion that the auto-oscillation is a system instability which is primarily caused by the active dynamic characteristics of the turbo pump. The dominant role played by the mass flow gain factor as part of the transfer function in the onset of the instability is reconfirmed. A stability analysis based on the models developed to describe the POGO effect and further interpretations of the transfer matrix were added by Oppenheim and Rubin [46, 55]. Tsujimoto *et al.* report that a positive mass flow gain factor causes rotating cavitation as a result of a linear, quasi-steady analysis [61]. The solutions are presented in a plane limited by the compliance and mass flow gain factor axes for different values of the cavitation number σ, identifying the stable and unstable operating ranges. The predicted modes are identified experimentally with pressure fluctuation measurements [63]. A nonlinear calculation of rotating cavitation preceded the measurements by the same authors [62]. Koutnik and Pulpitel applied a transfer matrix model to Francis turbines in 1996 for the purpose of a stability analysis [34], using the discharge and pressure values downstream of the cavity for their calculation. They presented a similar mapping of stable and unstable operating ranges as Tsujimoto *et al.* in a compliance - mass

4

flow gain factor plane. Chen *et al.* presented in 2008 a further developed stability analysis, using both the up- and downstream pressure and mass flow variations to account for the destabilizing effects of the swirling flow and the conical shape of the diffuser [13]. The transfer matrix method was recently validated experimentally by Yamamoto *et al.* [66] on a simplified test configuration for several values of the flow resistance, inertance and compliance.

Further developments of mathematical models of the two-phase flow in Francis turbines were recently proposed by Kuibin *et al.* [35, 36] and Resiga *et al.* [59]. One-dimensional approaches based on electrical analogies are introduced by several authors (the reader may refer to Nicolet [44] and Dörfler *et al.* [15, 16]). The hydroacoustic parameters of such models may be determined by means of CFD calculations with the ultimate goal of identifying the underlying causes leading to full load surge. Alligné *et al.* [2, 3] reproduced the unstable behavior observed on a reduced scale model by introducing an additional thermodynamic damping parameter to the hydroacoustic model. Dörfler *et al.* identifies the runner outlet swirl as the main destabilizing variable [17]. Chirkov *et al.* [14] managed to reproduce the self-excited pressure oscillations at full load with a 1D-3D hybrid approach. Rudolf *et al.* identified the eigenmodes in the swirling draft tube flow by Proper Orthogonal Decomposition [56]. Landry *et al.* extended the 1-D model to include the unsteady friction in the draft tube [38]. The most recent contribution by Alligné *et al.* includes the convective terms in the momentum equation and finds the divergent draft tube geometry to be the destabilizing parameter, ultimately inducing the self-oscillation of the flow [4].

0.4 Thesis objective

The primary aim of this research project is the determination of the underlying physical mechanisms leading to self-excited pressure oscillations in hydraulic turbines by performing a series of measurements on a reduced scale physical model of a Francis turbine as well as on a small scale test facility with a micro-turbine. It is achieved by studying the unsteady, two-phase flow in the the draft tube of the turbine with state of the art measurement techniques, such as LDV, PIV and high-speed visualization, and by developing the appropriate post-processing tools for the analysis. Furthermore, an important aspect is to quantify how the instability interacts with its surrounding system, for instance by measuring the fluctuations of the torque and the runner frequency.

The different existing one-dimensional modeling approaches are aimed to be evaluated by studying the behavior of the hydroacoustic draft tube parameters on a simplified test case with a micro-turbine. This is reached by the measurement of the instant flow rate fluctuations with pressure transducers and the estimation of the instant vortex rope volume.

Finally, the data obtained from the various measurements at a large set of operating conditions shall form a comprehensive data base for the validation and further development of analytical and numerical flow models.

0.5   Document structure

Chapter 1 treats the external aspects of overload pressure surge and is a qualitative introduction to the phenomenon at hand. It describes how the instability manifests itself throughout the hydraulic system and displays its tangible facets, such as the pressure pulsations at different locations and the two-phase flow with the oscillating vortex rope that can be observed in the draft tube cone.

Chapter 2 describes the investigations on a simplified test case with a micro-turbine and a conical diffuser. Important physical insights are gained by reproducing the instability and by measuring the temporal discharge and vortex rope volume variations in the upstream and downstream flow during self-sustained pressure oscillations. The behavior of the hydroacoustic draft tube parameters is analyzed.

Chapter 3 includes a detailed description of the draft tube flow observed on a 1:16 reduced scale physical model of a Francis turbine. Velocity components are measured by means of LDV and fluorescent PIV, synchronized with pressure fluctuation measurements. The result is a comprehensive characterization of the flow during self-excited pressure oscillations under various operating conditions. Chapter 3 also contains a description of the measurement techniques and post-processing tools used for the analysis of the result.

Chapter 4 finally contains the calculation of the draft tube swirl based on the velocity measurements presented in the foregoing Chapter 3. It also describes the interaction between the vortex rope and the blade cavitation, as well as the instant variations of the runner frequency and the torque.

Throughout the document, experimental methods and results are documented for several operating conditions. For the reduced scale model tests in chapters 3 and 4, the operating conditions are summarized in Table B.1 of Appendix B. They are mainly divided into two levels of the speed factor, $n_{ED} = 0.273$ and $n_{ED} = 0.288$. The latter is the specified value at the BEP of the model machine. As shown in the following analysis, the appearance in terms of the vortex rope shape or the amplitudes of the pressure fluctuations changes significantly between the two n_{ED}-values. Different discharge levels are exploited, and systematical variations of the discharge factor Q_{ED} are performed in some cases. The reference value for the draft tube pressure level is expressed by a cavitation number of $\sigma = 0.11$, corresponding to the nominal value of the prototype machine. Systematic variations of this parameter are also performed. For the tests on the simplified test configuration with a micro-turbine, the operating conditions are summarized in Table C.1 in Appendix C.

1 Characterization of self-excited pressure oscillations in Francis turbines

1.1 Experimental observations

1.1.1 Test setup

A test setup with a 1:16 reduced scale physical model of a Francis turbine with a specific speed of $\nu = 0.27$ is installed on the EPFL test rig PF3 of the Laboratory for Hydraulic Machines, shown in Figure 1.1. It offers the possibility of a highly accurate simulation of an actual prototype according to IEC standards [27]. The real generating unit, featuring a rated power of 444 MW, is located in a power plant in the Canadian province of British Columbia and experiences serious overload pressure surge. Figure 1.2 displays a close view of the model geometry with its inlet pipe and diffuser, including the location of the wall pressure sensors.
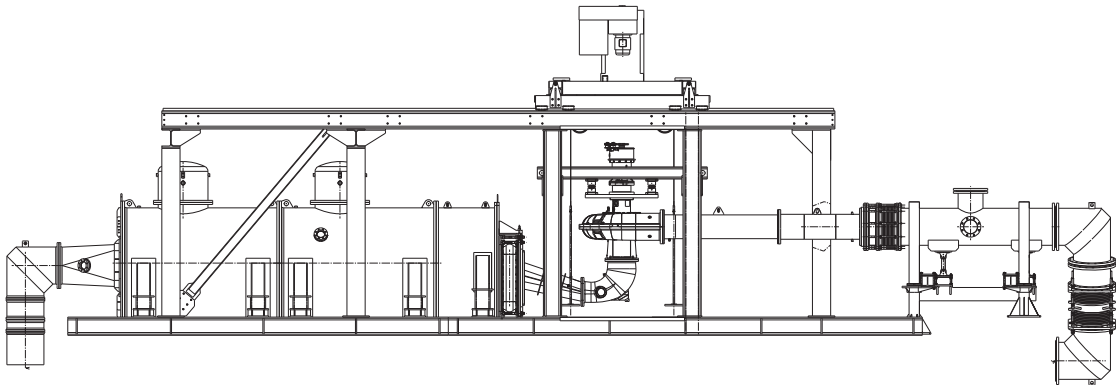
Figure 1.1: Reduced scale model of the Francis turbine on the EPFL test rig PF3.

The test rig is operated in a closed loop configuration, driven by two axial double-volute pumps. A generator regulates the rotating speed of the runner. The pressure level in the draft tube, characterized by the cavitation number σ, is set by adjusting the pressure in the downstream reservoir with a vacuum pump. The hydraulic head is adjusted via the pump speed and the discharge is controlled by the guide vane opening.

(a) Cut through Section A-A

(b) Top view
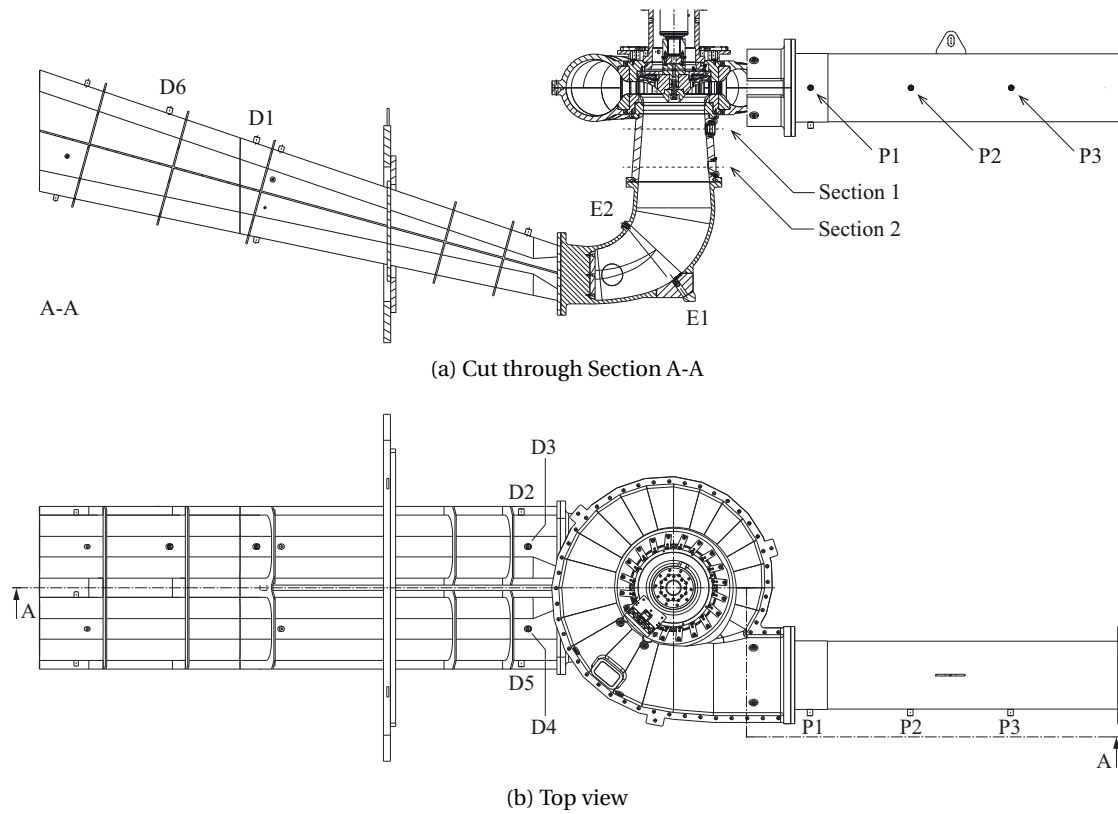
Figure 1.2: Close view of the reduced scale model with diffuser in two branches, elbow, draft tube cone, spiral case and inlet pipe. Pressure sensors are numbered D1-D6 in the diffuser, E1-E2 in the elbow and P1-P3 in the inlet pipe.

The wall pressure in the draft tube cone is measured at two streamwise levels, referred to as Section 1 and Section 2, situated $0.39 \times D_{\bar{1}}$ and $1.0 \times D_{\bar{1}}$ below the runner exit, as illustrated in Figure 1.2a. Two different Plexiglas versions of the cone are manufactured for the various measurement purposes, a first one accommodating 2×4 pressure sensors and a second one with 2×2 sensors. The horizontal measurement sections 1 and 2 are shown for both cones in Figure 1.3. The second cone in Figure 1.3b is furthermore equipped with a water filled window attached to its outer surface. This so called waterbox with a flat vertical cover minimizes the optical distortion effects when using cameras for flow visualization or PIV measurements.

1.1.2 Vortex rope and pressure oscillations

The self-excited regime of the vortex rope oscillation in the draft tube is illustrated in Figure 1.4 for the operating conditions OP#1 at 131% of the nominal discharge. The sequence of 5×4 photos covers a single cycle and shows the different stages of the oscillation. The period of the oscillation is $T = 0.358$ s and the time increment between the photos is $\Delta t = 18.8$ ms. Counting from the top left, the first 9 pictures show the growing phase of the cavity. Next, the introduction of bubbles into the surrounding flow from above is indicated by a change in

(a) Basic measurement configuration

(b) Configuration for flow visualizations and PIV measurements
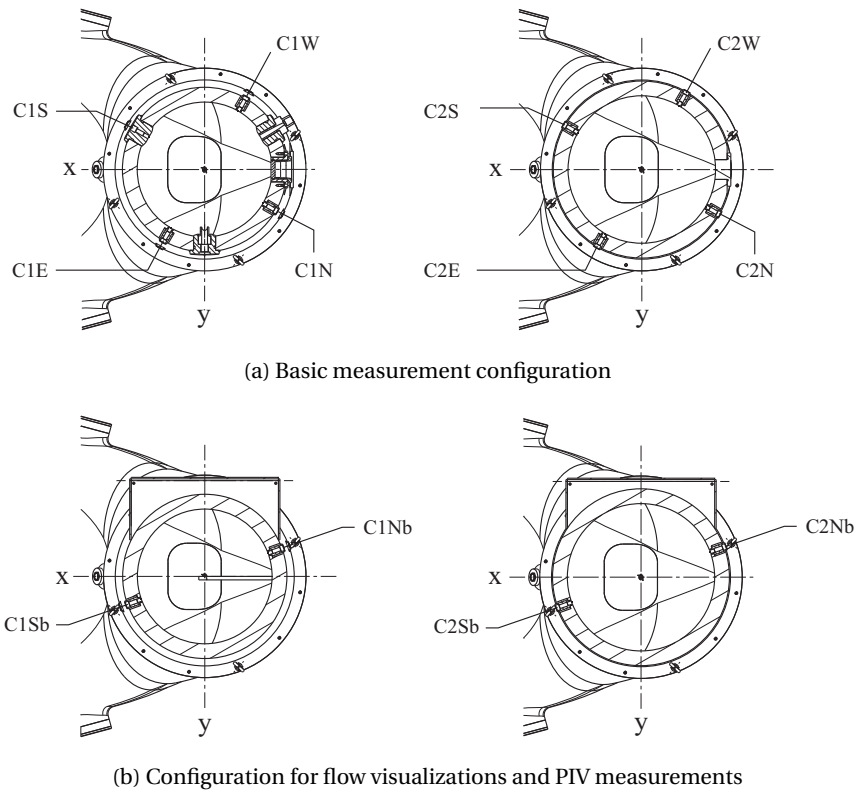
Figure 1.3: Horizontal wall pressure measurement planes in the draft tube cone at $0.39 \times D_{\bar{I}}$ (left) and $1.0 \times D_{\bar{I}}$ (right) below the runner exit with absolute frame of reference (x and y axes).

luminance. As shown in a later section of this work, these bubbles originate from cavitation on the blades of the turbine runner. After the main body of the cavity seemingly stretches in streamwise direction in pictures 10 to 12, the vortex rope collapses back upon itself, starting from the node at the lower end of its main body. This is illustrated by the cavity becoming increasingly non-transparent from the bottom to the top in pictures 13 to 16. Finally, pictures 17 to 20 show the terminal stage of the collapse and the beginning of the comeback, which coincides with expulsion of the remaining bubbles in the surrounding flow.

Figure 1.4: High-speed visualization of the cavitating vortex rope at OP#1.

The above described cycle is manifestly coupled with significant pressure pulsations throughout the circuit. Typical wall pressure signals at various locations of the reduced scale model are shown in Figure 1.5. For this particular operating point, the pressure peaks seem to correspond to the collapse of the vortex rope, whereas the pressure minima are reached when the cavity is at its maximum volume. This is however not generally valid, as shown in Section 3.4. Since the pressure is made non-dimensional with ρE, it follows that the amplitude of the oscillation reaches up to 15% of the specific energy at the given operating point in the draft tube cone. The amplitudes remain on a high level in the inlet pipe and the elbow before being damped in the diffuser pipe.

The collapse of the cavity is initiated shortly after a cycles's global wall pressure minimum. This phase is characterized by a local pressure bump before the global rise in the lower section of the draft tube cone, the inlet pipe, the elbow and in the diffuser entry (see Figures 1.5a, 1.5b, 1.5d, 1.5e, 1.5f and 1.5g), while only a highly fluctuating signal is observed at the same time in the wall pressure closest to the runner exit in the draft tube cone (see Figure 1.5c).

The regularity of the self-excited pressure fluctuations is confirmed in the frequency domain. Figure 1.6 displays the power spectral density of the wall pressure factor at four locations, namely in the inlet pipe, the draft tube cone and the diffuser. The spectra are estimated with the Welch's method [64], taking into account three windows of 2^{15} data points each, with an overlap of 50%. The synchronous nature of the pressure fluctuations throughout the draft tube, confirming the existence of a standing plane wave, was already confirmed by Alligné in 2011 [2] for the same test case. The fundamental frequency in this case is located at 2.76 Hz and the vortex rope oscillates hence at 25% of the runner frequency. Its amplitude is higher in the upstream inlet pipe than in the draft tube cone and rapidly decreasing towards the diffuser. A synchronous contribution corresponding to the runner frequency is not detected.

(a) Inlet pipe (P3)

(b) Inlet pipe (P1)

(c) Draft tube cone (C1Nb)

(d) Draft tube cone (C2Nb)

(e) Elbow, upper side (E2)

(f) Diffuser inlet, left branch (D4)

(g) Diffuser inlet, right branch (D3)

(h) Diffuser, right branch (D1)
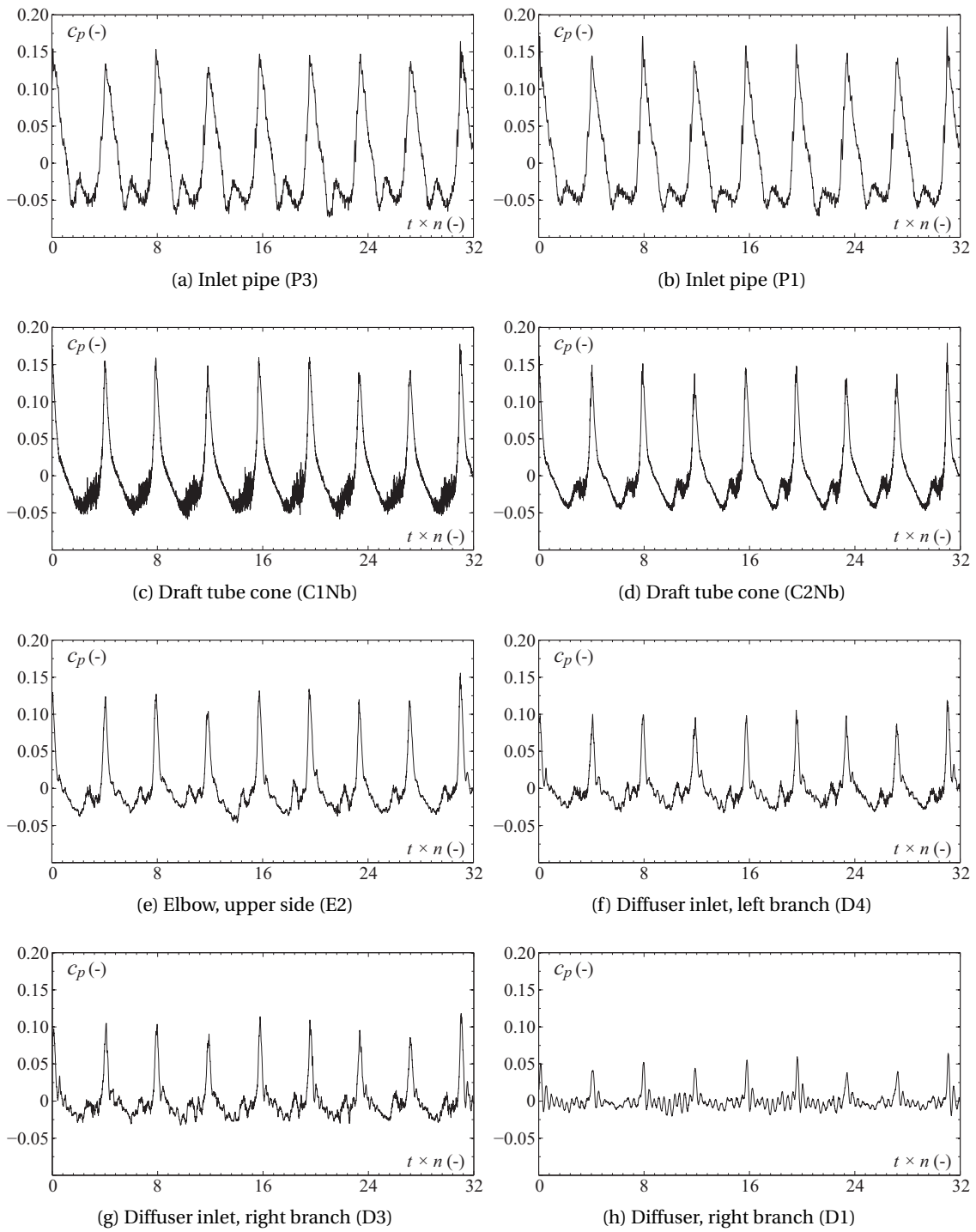
Figure 1.5: Fluctuation of the pressure factor c_p throughout the reduced scale model as a function of the number of runner revolutions at OP#1. The measurement locations are marked in Figures 1.2 and 1.3.

(a) Inlet pipe (P1)

(b) Draft tube cone, Section 1 (C1Nb)

(c) Draft tube cone, Section 2 (C2Nb)

(d) Diffuser inlet, right branch (D3)
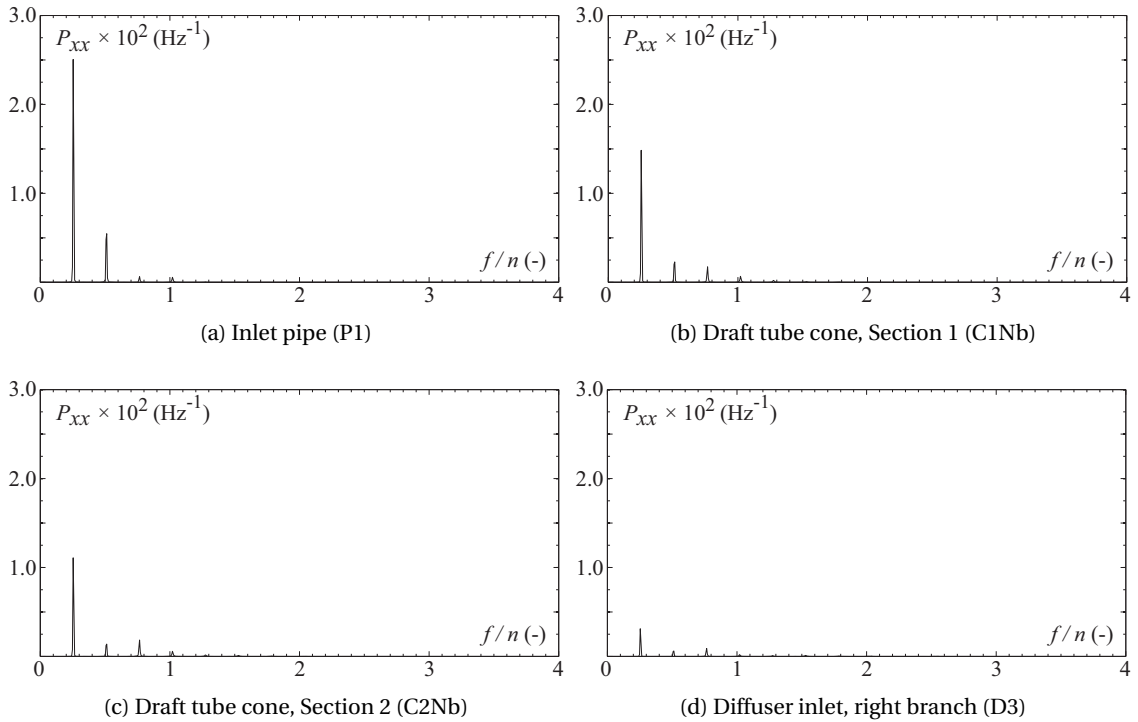
Figure 1.6: Power spectral densities of the wall pressure factor c_p in the inlet pipe, the draft tube cone and the diffuser inlet.

1.1.3 Effects of a change in the discharge and draft tube pressure level

Among the perceivable properties of the vortex rope oscillation are the frequency at which the pressure fluctuations occur as well as the shape and volume of the cavity. These properties are strongly influenced by the pressure level in the draft tube, expressed by the cavitation number σ, and the load level, represented by the discharge factor Q_{ED}. In the following, systematic variations of σ and Q_{ED} are performed around two different reference points and the influence on the dominant frequency of the oscillation in the draft tube cone as well as the cavity shape is investigated.

The evolution of the dominant surge frequency for a variation of the draft tube pressure level at OP#6 is shown in Figure 1.7. Ten different cavitation numbers between $\sigma = 0.10$ and $\sigma = 0.163$ are investigated, while keeping the remaining variables defining the operating conditions constant. The power spectral densities for each measuring point are displayed in the waterfall diagram of Figure 1.7a and the behavior of the fundamental frequency and amplitude are displayed in Figure 1.7b and Figure 1.7c, respectively. The surge frequency, normalized by the mean runner frequency, increases linearly with a growing σ in a least square sense. So does the corresponding amplitude, oscillating around the linear approximation.

As mentioned beforehand, it can be expected that a variation of the draft tube pressure level

(a) Waterfall diagram

(b) Fundamental frequency evolution

(c) Fundamental amplitude evolution
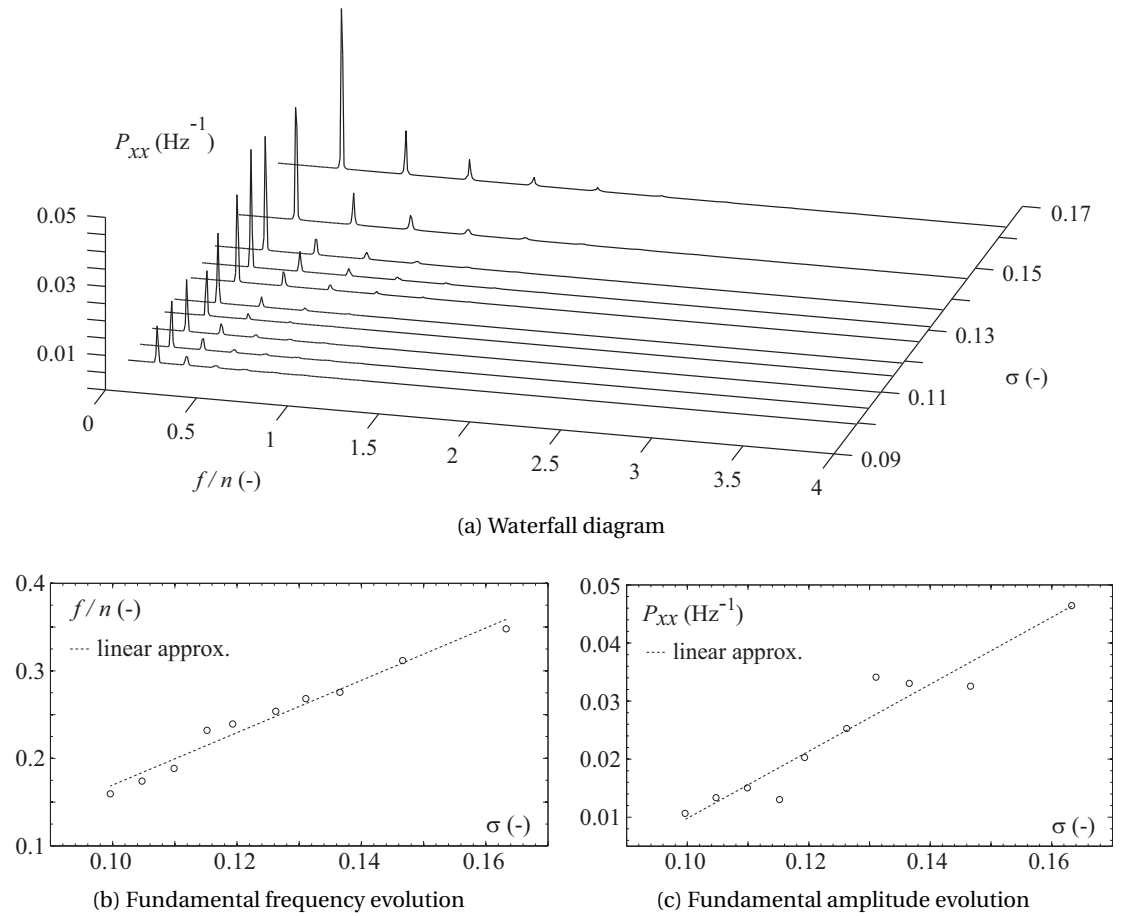
Figure 1.7: Power spectral density of c_p in the draft tube cone (sensor C1Nb) and evolution of the dominant frequency and amplitude for different σ-values around OP#6.

has an impact on the cavity volume. This is illustrated in Figure 1.8, showing one snapshot of the vortex rope at each of the investigated σ-values. The pictures are taken at the half time of the given cycle, the latter being defined as the period between two peaks of the cone wall pressure signal (sensor C1Nb). As a side note, that same definition of a complete cycle is used in Figure 1.4. In a first observation, the tendency of the vortex rope volume to increase with a decreasing cavitation number σ seems confirmed. This is however to be taken with caution, as the shape and constitution of the cavity as well as the concentration of bubbles in the surrounding flow clearly suggest that the time $t = 0.5 \times T$ does not consistently define the same stage of the vortex rope oscillation. In other words, the duration of the growing and collapsing phase are not proportional to the relative period between two pressure peaks. A further discussion requires an estimation of the vortex rope volume, which is presented in Chapter 3.

(a) $\sigma = 0.163$ (b) $\sigma = 0.147$ (c) $\sigma = 0.137$ (d) $\sigma = 0.131$ (e) $\sigma = 0.126$

(f) $\sigma = 0.119$ (g) $\sigma = 0.115$ (h) $\sigma = 0.110$ (i) $\sigma = 0.105$ (j) $\sigma = 0.100$
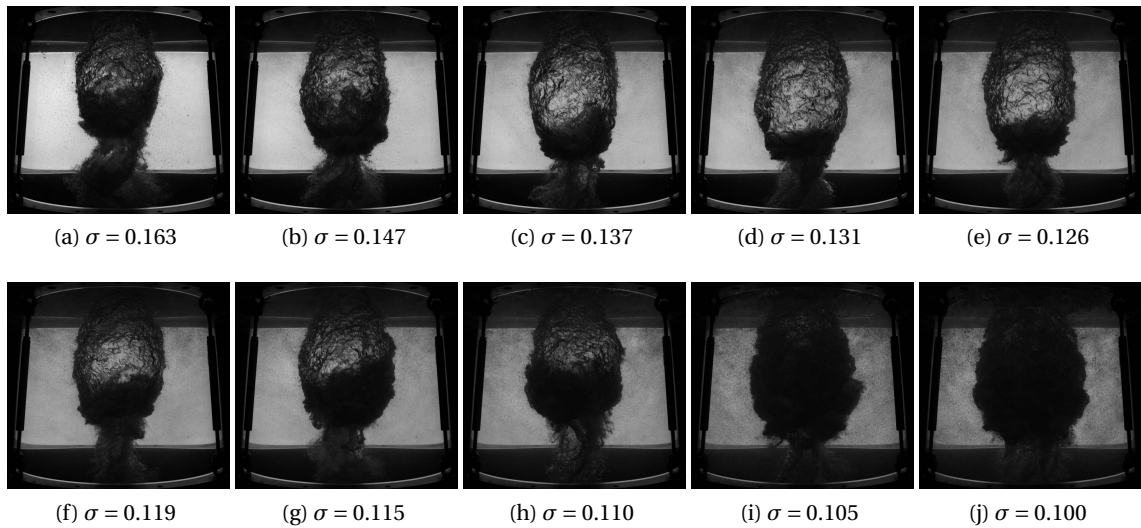
Figure 1.8: Vortex rope shape at $t = 0.5 \times T$ for different values of σ around OP#6.

The effect of a variation of the discharge factor Q_{ED} around OP#1 is shown in Figure 1.9. While the dominant surge frequency in Figure 1.9b decreases linearly with an increasing load, no such conclusion can be supported by the available data for the amplitude in Figure 1.9c. A snapshot of the vortex rope at mid-cycle ($t = 0.5 \times T$) is shown for each value of the discharge factor Q_{ED} in Figure 1.10. The same remarks as stated in case of the σ-variation apply to the present case. While the vortex rope collapse is already being initiated in Figure 1.10a, it has barely reached its maximum volume at the lower end of the tested Q_{ED}-range in Figure 1.10e.

1.1.4 Notions of instability

The notion of *instability* or *unstable operation* of Francis turbines commonly refers to the self-excited character of the pressure oscillations in the machine. As already reported in [2] for the same test case, the corresponding flow parameters fundamentally differ from a *stable* configuration. At a so called stable operating point, for instance, the pressure fluctuations have a significantly lower amplitude and a more random appearance. Furthermore, if the pressure level in the draft tube favors cavitation, a stable vortex rope fluctuates around a mean volume, whereas it completely disappears and reappears again at unstable conditions as shown previously. These aspects are further discussed in Section 2.5.3.

(a) Waterfall diagram

(b) Fundamental frequency evolution

(c) Fundamental amplitude evolution
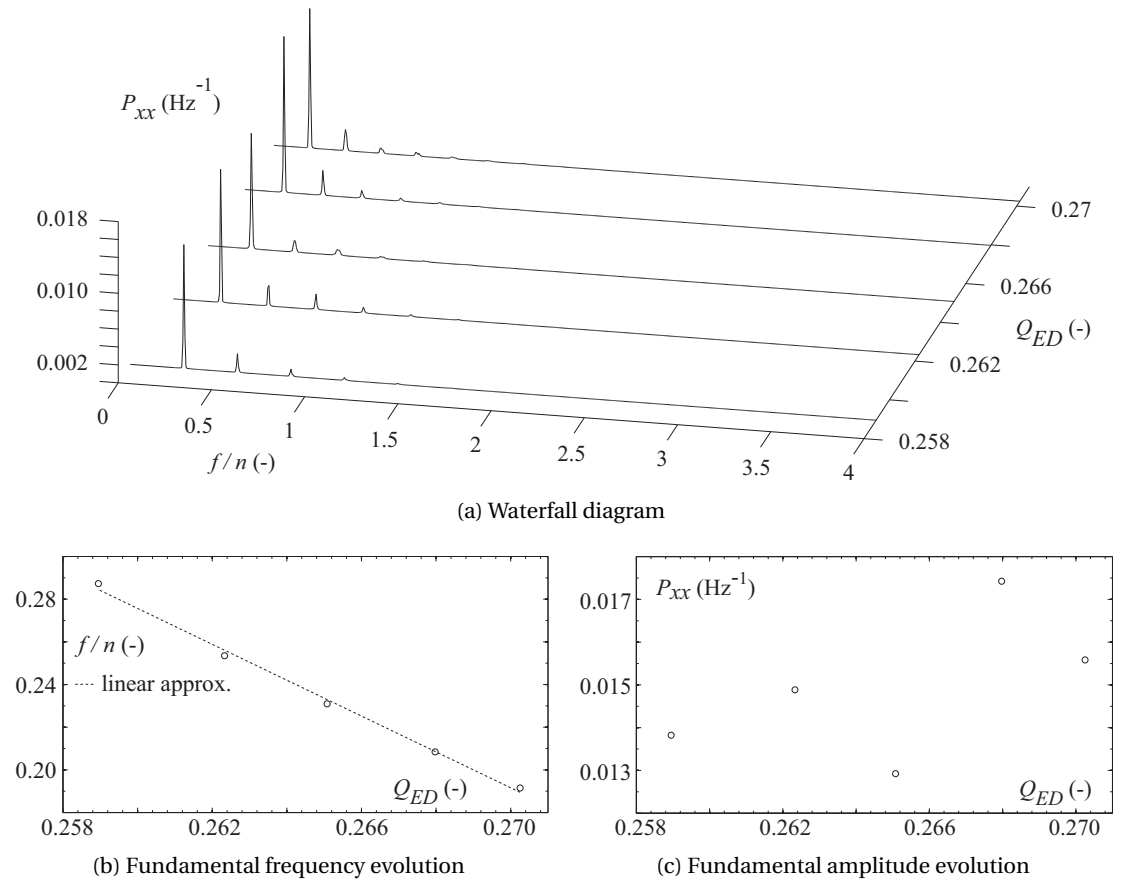
Figure 1.9: Power spectral density of c_p in the draft tube cone (sensor C1Nb) and evolution of the dominant frequency and amplitude for different Q_{ED}-values around OP#1.

(a) $Q_{ED} = 0.2703$ (b) $Q_{ED} = 0.2680$ (c) $Q_{ED} = 0.2651$ (d) $Q_{ED} = 0.2623$ (e) $Q_{ED} = 0.2590$
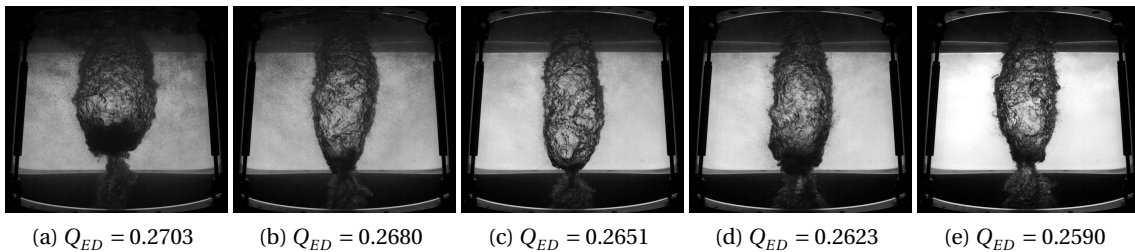
Figure 1.10: Vortex rope shape at $t = 0.5 \times T$ for different values of Q_{ED} around OP#1.

1.2 Introduction to an analytical and numerical description

1.2.1 Mass balance in the draft tube

The presence of a gaseous volume in the draft tube cone significantly changes the physics of the local flow. For instance the local speed of sound, which depends essentially on the volume of the cavity and is determining the Eigenfrequencies of the hydraulic system. Another issue is the impact of the pulsating vortex rope on the local mass balance. In the following, these effects are addressed by analysing the flow across a control volume whose limits completely incorporate the vortex rope. Such a control volume is illustrated in Figure 1.11.
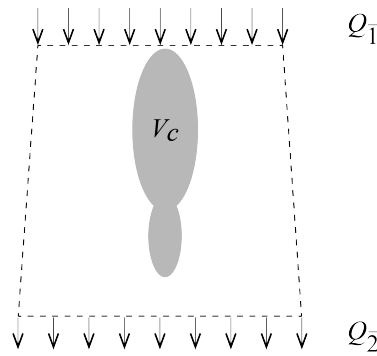
Figure 1.11: Control volume in the draft tube containing the volume V_c of the vortex rope.

In Figure 1.11, the flow rates $Q_{\bar{1}}$ and $Q_{\bar{2}}$ enter and exit the control volume, respectively. The remaining area is a material surface, representing the inner draft tube cone wall. In order to respect the conservation of mass, the difference of the two flow rates must correspond to the total change in the vortex rope volume, expressed as

$$Q_{\bar{1}} - Q_{\bar{2}} = \frac{\mathrm{d}V_c}{\mathrm{d}t} \; . \tag{1.1}$$

Furthermore, it is assumed that cavity volume is a function of the inlet and outlet flow rates, as well as the pressure level in the draft tube. Hence,

$$V_c = f\left(Q_{\bar{1}}, Q_{\bar{2}}, h_{\bar{1}+\frac{1}{2}}\right) , \tag{1.2}$$

where $h_{\bar{1}+\frac{1}{2}}$ is the piezometric head in the middle of the draft tube cone, between the nodes $\bar{1}$

and $\bar{2}$. The development of the total derivative in eq. (1.1) then yields

$$
\frac{\mathrm{d}V_c}{\mathrm{d}t} = \underbrace{\left.\frac{\partial V_c}{\partial Q_{\bar{1}}}\right|_{Q_{\bar{2}},h}}_{-\chi_{\bar{1}}} \cdot \frac{\mathrm{d}Q_{\bar{1}}}{\mathrm{d}t} + \underbrace{\left.\frac{\partial V_c}{\partial Q_{\bar{2}}}\right|_{Q_{\bar{1}},h}}_{-\chi_{\bar{2}}} \cdot \frac{\mathrm{d}Q_{\bar{2}}}{\mathrm{d}t} + \underbrace{\left.\frac{\partial V_c}{\partial h}\right|_{Q_{\bar{1}},Q_{\bar{2}}}}_{-C_c} \cdot \frac{\mathrm{d}h}{\mathrm{d}t} \,,
\tag{1.3}
$$

where the partial derivatives of the vortex rope volume with respect to the flow rates and the piezometric head are defined as the hydroacoustic parameters of the draft tube flow. Namely, they are

- $\chi_{\bar{1}}$ Upstream mass flow gain factor

- $\chi_{\bar{2}}$ Downstream mass flow gain factor

- C_c Cavitation compliance

Similar formalisms are used by many authors for the hydroacoustic modelling and stability analysis [2, 4, 15, 33]. As clarified later, several one-dimensional model exist, based on a diverging significance attributed to the individual hydroacoustic flow parameters. One of the present work's goals is to provide an experimental data set allowing to assess the physical accuracy of the different modelling approaches.

1.2.2   Calculation of the hydroacoustic draft tube flow parameters

The two mass flow gain factors $\chi_{\bar{1}}$ and $\chi_{\bar{2}}$ may be determined by measuring the instantaneous vortex rope volume and the upstream and downstream flow rate fluctuations. In order to simplify the calculation of the vortex rope compliance C_c based on measurement, the piezometric head h can be expressed as a function of the the cavitation number σ as follows. The net positive suction energy (NPSE) is defined as

$$
\mathrm{NPSE} = gH_{\bar{1}} - gZ_{\mathrm{ref}} - \frac{p_v}{\rho} \,,
\tag{1.4}
$$

where $gH_{\bar{1}}$ is the specific hydraulic energy at the power unit low pressure reference section, Z_{ref} the elevation of the power unit reference level, p_v the vapor pressure and ρ the water density. The hydraulic energy at an arbitrary point $\bar{x}$ in the diffuser can be expressed as the sum of the specific hydraulic energy $gH_{\bar{1}}$ and the losses between the two points. This translates

to

$$gH_{\bar{I}} = gH_{\bar{x}} - gH_{r_{\bar{x} \div \bar{I}}} \longleftrightarrow H_{\bar{I}} = \underbrace{\underbrace{\frac{p_{\bar{x}}}{g \cdot \rho} + Z_{\bar{x}}}_{h_{\bar{x}}} + \frac{C_{\bar{x}}}{2g}}_{H_{\bar{x}}} - H_{r_{\bar{x} \div \bar{I}}} \,, \tag{1.5}$$

where $gH_{r_{\bar{x} \div \bar{I}}}$ are the hydraulic energy losses between the points $\bar{x}$ and $\bar{I}$, and $h_{\bar{x}}$ is the piezometric head at the arbitrary point $\bar{x}$. Finally, using eq. (1.5) in eq. (1.4), the NPSE becomes

$$\text{NPSE} = gh_{\bar{x}} + \frac{C_{\bar{x}}}{2} - gH_{r_{\bar{x} \div \bar{I}}} - gZ_{\text{ref}} - \frac{p_v}{\rho} \,. \tag{1.6}$$

Differentiating the vortex rope volume V_c with respect to the NPSE instead of the piezometric head entails the change in variables

$$\frac{\partial V_c}{\partial h} = \frac{\partial V_c}{\partial (\text{NPSE})} \cdot \frac{\partial (\text{NPSE})}{\partial h} \,. \tag{1.7}$$

In eq. (1.6) only one term depends on h. Taking into account the definition of the cavitation number, $\sigma = \text{NPSE}/E$, the derivative therefore simply becomes

$$\frac{\partial V_c}{\partial h} = \frac{\partial V_c}{\partial (\text{NPSE})} \cdot g = \frac{\partial V_c}{\partial \left(\frac{\cdot \text{NPSE}}{g} \right)} = \frac{\partial V_c}{\partial \left(\frac{E}{g} \cdot \sigma \right)} = \frac{\partial V_c}{\partial \left(\frac{1}{H} \cdot \sigma \right)} \,, \tag{1.8}$$

where H is the head of the machine. Assuming that H is constant at a given operating point, it can be taken out of the derivative and the cavitation compliance is finally defined as

$$C_c = \frac{1}{H} \frac{\partial V_c}{\partial \sigma} \,. \tag{1.9}$$

1.3 Summary and discussion

Chapter 1 contains a qualitative description of the self-sustained pressure oscillations in a reduced scale physical model of a Francis turbine. Several characteristic aspects are introduced, such as the regularity and the synchronous nature of the wall pressure fluctuations throughout the system, as well as the growth and almost total collapse of the vortex rope during one cycle of the pressure oscillation. Furthermore, a periodically changing concentration of bubbles in the surrounding flow is observed.

The dominant frequency of the pressure oscillation varies linearly with the cavitation number σ and the discharge factor Q_{ED}. The same can be said for the corresponding amplitude as a function of σ. The relative duration of the different phases of the vortex rope oscillation with respect to the period between two pressure peaks is not constant. A decreasing sigma appears to decelerate the vortex rope growth, where the cavity almost seems more inert with its increased mean volume. The same effect has an increase of the discharge factor Q_{ED}.

Finally, the analytical background of currently available one-dimensional models to describe the two-phase flow in the draft tube is introduced and the main hydroacoustic parameters are defined.

2 Simplified test case

2.1 Motivation and context

In order to develop a deeper understanding of how the the main flow parameters behave during self-sustained pressure oscillations, measurements are performed on a small scale hydraulic circuit featuring a micro-turbine and a horizontal conical diffuser. The simplified configuration bears the advantage of a rather straight forward access to the relevant system variables by measurement, such as the flow rate fluctuations upstream and downstream of the turbine as well as the vortex rope volume. These quantities, necessary for the calculation of the hydroacoustic draft tube model parameters, are not easily obtained on a reduced scale physical model, which remains of considerable size and complexity.

In a first step, the properties of the self-excited pressure oscillation discussed in Chapter 1 are compared to their counterparts on the simplified test configuration, in order to verify that the two flow regimes are equal. Based on the measurements of the flow rates and an estimation of the vortex rope volume from high-speed flow visualizations, the behavior of the mass flow gain factor and the cavitation compliance is discussed for several operating conditions.

2.2 Experimental setup

The test rig is shown in Figure 2.1 is part of the experimental facilities of the Graduate School for Engineering Sciences at the University of Osaka in Japan. It consists of a closed loop hydraulic circuit driven by a centrifugal pump, featuring a micro-turbine with a horizontal conical diffuser. The latter is followed by a sudden expansion with vortex fences to reduce the swirl before the pressure measurements for the discharge determination. The flow rate is set via the pump speed and the runner speed is controlled with a small AC servo motor. The cavitation number is changed with a vacuum pump connected to the downstream reservoir.
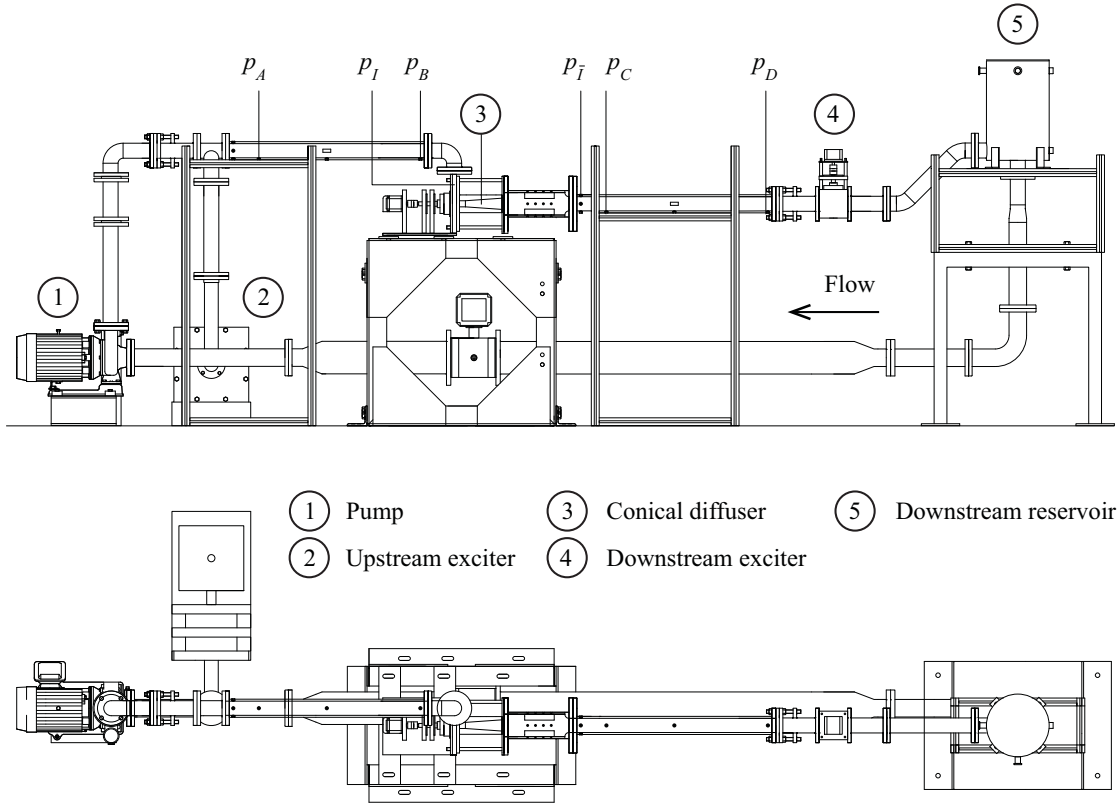
Figure 2.1: Small scale test facility simulating a hydropower power plant from [67].

Six absolute wall pressure signals are measured at three streamwise locations of the conical diffuser, using piezoresistive sensors with a 1 MPa range. The corresponding locations are shown in Figure 2.2. Three sensors are mounted vertically on the top of the cone, the other three sensors horizontally. The inlet and outlet diameter $D_{\bar{1}}$ and D_{cone} of the conical diffuser are $3.1 \cdot 10^{-2}$ m and $5.7 \cdot 10^{-2}$ m, respectively. The dimensions of L_1 and L_2 are $5.8 \cdot 10^{-2}$ m and $18.6 \cdot 10^{-2}$ m. The unsteady upstream and downstream flow rate is calculated based on the wall pressure signals p_A & p_B and p_C & p_D with the method presented in Section 2.3.2. The corresponding measuring locations are specified in Figure 2.1 and the used pressure transducers are of piezoresistive differential type with a range of 10 kPa and an accuracy of 0.04 %. The vortex rope oscillation is recorded with a high speed camera.

The test rig also contains two flow exciters in form of an oscillating piston and a siren valve at positions upstream of the micro-turbine and downstream of the conical diffuser, respectively (items 2 and 4 in Figure 2.1. They may be used to establish the dynamic transfer functions of the pressure and the discharge. This is not further discussed in the present work and the reader may refer to [66].
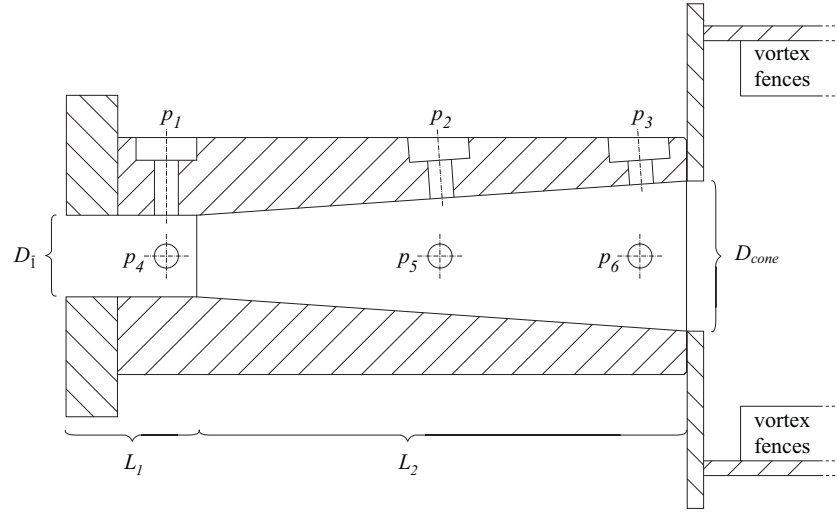
Figure 2.2: Simplified vertical cut of the circular turbine outlet, the conical draft tube with pressure sensor locations p_1 - p_6 and the sudden expansion with vortex fences.

2.3 Methodology

2.3.1 Definition of operational parameters

The operating conditions for the measurements are summarized in Table C.1. For the determination of the cavitation number σ as well as the speed and discharge factors n_{ED} and Q_{ED}, the specific energy is defined as

$$E = \Delta\left(\frac{p}{\rho} + gz\right)_{I-\bar{I}} + \Delta\frac{1}{2}C^2 = \frac{p_I - p_{\bar{I}}}{\rho} + \frac{1}{2}\left(\frac{\bar{Q}^2}{A_I^2 - A_{\bar{I}}^2}\right), \tag{2.1}$$

where $\bar{Q}$ is the mean discharge measured by an electromagnetic flow meter, A_I the upstream reference section area at the turbine inlet and $A_{\bar{I}}$ the downstream reference section area at $p_{\bar{I}}$ in Figure 2.1; $p_I - p_{\bar{I}}$ is the pressure difference between these two reference sections. The cavitation number is then calculated according to

$$\sigma = \frac{1}{E}\left(\frac{p_b - p_v}{\rho} - gH_s + \frac{1}{2}\frac{\bar{Q}^2}{A_{\bar{I}}^2}\right), \tag{2.2}$$

where p_b is the pressure in the downstream reservoir, p_v the vapor pressure, and H_s stands for the difference in altitude between the water level in the downstream reservoir and the horizontal symmetry axis of the draft tube.

2.3.2   Flow rate estimation through differential pressure measurement

The following procedure is the result of a projection of the equation of momentum conservation for inviscid, irrotational and incompressible pipe flow, assuming uniform distributions of the pressure p, the density ρ and the velocity C in a given cross-section A [44]. The integral form of the momentum equation is given by

$$\int\limits_V \rho \frac{\mathrm{D}C}{\mathrm{D}t}\mathrm{d}V = \int\limits_V \frac{\partial}{\partial t}\left(\rho\cdot\vec{C}\right)\mathrm{d}V + \int\limits_{\partial V} \rho\vec{C}\left(\vec{C}-\vec{u}\right)\cdot\vec{n}\,\mathrm{d}A = \Sigma\vec{F}, \tag{2.3}$$

where $\vec{u}$ represents the velocity vector of the pipe displacement and $\Sigma\vec{F}$ the sum of external forces acting on a given control volume. Neglecting the displacement and the friction in the pipe and considering only pressure and gravitational forces, the projection of eq. (2.3) on the x-axis is simplified to

$$\frac{1}{\rho}\frac{\partial p}{\partial x} + \frac{\partial C}{\partial t} + C\frac{\partial C}{\partial x} + g\sin\alpha = 0, \tag{2.4}$$

where α stands for the inclination angle. Due to the horizontal configuration the term $\sin\alpha$ vanishes and the integration of eq. (2.4) between two arbitrary points a and b in the pipe yields

$$\int\limits_a^b \frac{1}{\rho}\frac{\partial p}{\partial x}\,\mathrm{d}x + \int\limits_a^b \frac{\partial C}{\partial t}\,\mathrm{d}x + \int\limits_a^b C\frac{\partial C}{\partial x}\,\mathrm{d}x = \frac{1}{\rho}\left(p_b - p_a\right) + \frac{1}{A}\frac{\partial Q}{\partial t}\underbrace{\left(x_b - x_a\right)}_{L} + \frac{1}{2}\left(C_b^2 - C_a^2\right) = 0. \tag{2.5}$$

Since C_a and C_b are equal, eq. (2.5) finally becomes

$$\frac{\partial Q}{\partial t} = \frac{A}{\rho L}\left(p_a - p_b\right). \tag{2.6}$$

The pressure and the discharge variables can be represented as the sum of their mean and fluctuating parts, $p = \bar{p} + \tilde{p}$ and $Q = \bar{Q} + \tilde{Q}$. The mean discharge vanishes in the derivative of eq. (2.6) and, assuming $p_a = p_b$ in absence of losses, the fluctuating part of the discharge Q is

obtained by calculating the integral

$$\tilde{Q}(t) = \frac{A}{\rho L} \int \left(\tilde{p}_a - \tilde{p}_b \right) \mathrm{d}t. \tag{2.7}$$

The accuracy of the method is discussed in [32]. It is stressed that the mean discharge value may not be obtained by this method and the corresponding value from the electromagnetic flow meter is used for the following development.

2.3.3 Estimation of the vortex rope volume

As presented in Section 1.2.2, the vortex rope volume V_c is necessary for the calculation of the hydroacoustic draft tube parameters. In this section, a method to estimate V_c in the horizontal draft tube cone shown in Figure 2.2 is introduced, based on comparing consecutive images from a high-speed visualization, such as the one shown in Figure 2.7 .

A video consists of N_f grayscale images and the following process is applied to each individual frame. A given image is first converted to a black and white (binary) form with an ideal threshold value according to [48]. The result is then inverted, so that the area of the vortex rope appears in white (pixel value = 1). A region of interest (ROI) is defined by the vertices of a polygon around the area corresponding to the turbine outlet and the draft tube cone, hence the inner surface of the section shown in Figure 2.2. The ROI is displayed in Figure 2.3a for a single frame of the visualization at OP#A. It is used to define a binary mask in the form of an image of the same size as the processed image, where all the pixels inside the ROI are set to 1 and the rest to 0. This mask is then applied to the inverted binary images from the high speed camera. The end result are 256 × 512 matrices I_{bin}, their dimension being equal to the resolution of the original image, where all the pixels which are either outside the ROI or of black color are represented by a zero. Consequently, the ones (pixel value = 1) in the matrices stand for white pixels inside the ROI. This is illustrated in Figure 2.3b.

(a) ROI   (b) Binary mask
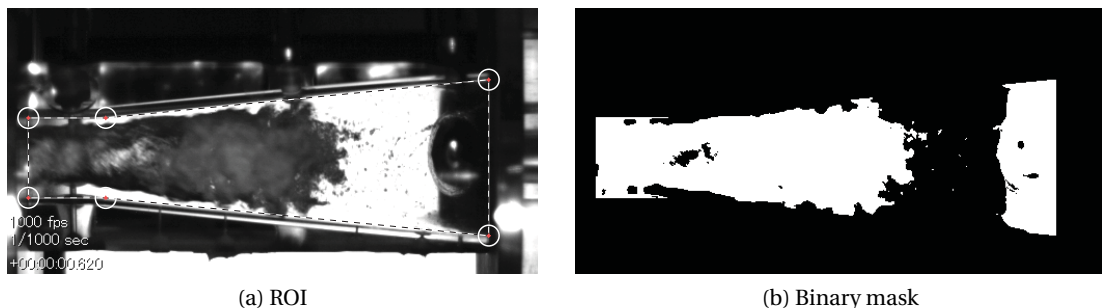
Figure 2.3: Left: Region of interest (dashed line) with vertices (white circles). Right: Result of the inversion of the binary image and application of the mask.

In order to the calculate the growth or the diminution of the cavity, the matrices representing two consecutive frames at t_n and t_{n+1}, respectively, are subtracted. The sum of the non-zero elements of the resulting differential matrix brings forth a change ΔA_c in the area of the projected vortex rope, calculated according to

$$\Delta I_{bin,n} = I_{bin,n+1} - I_{bin,n} \tag{2.8}$$

$$\Delta A_{c,n} = \sum_{j=1}^{N_c} \left(\sum_{i=1}^{N_r} \Delta I_{bin,n}(i,j) \right), \tag{2.9}$$

where N_c and N_r designate respectively the number of columns and rows of an image matrix. The total area occupied by the cavity at a time $t = t_n$ is finally calculated by summing up the surface changes ΔA_c between a reference time t_{ref}, for which the area $A_{c_{ref}}$ is calculated, and the time t_n. Hence,

$$A_{c,n} = A_{c_{ref}} + \sum_{i=n_{ref}}^{n} \Delta A_{c,i}, \tag{2.10}$$

where n_{ref} is the frame number at $t = t_{ref}$, $n = \left((t_n - t_{ref}) \times f_s - 1 \right)$ and f_s is the frame rate at which the video is taken. The reference surface $A_{c_{ref}}$ is evaluated by a pixel count in a manually defined ROI around the cavity in the relevant video frame. Hence, the reference time t_{ref} is arbitrary, but often chosen to correspond to a situation where the rope is easily distinguished from its environment, in other words where there is no overlapping with the pressure sensors in the background. The total cone surface A_{cone} is obtained by summing up the non-zero elements in the binary masked based on the ROI in Figure 2.3a. If the vortex rope is centered and axisymmetric, the ratio of the projected surface occupied by the cavity (A_c) and the total surface occupied by the cone $\left(A_{cone} \right)$ is equal to the ratio of the vortex rope volume (V_c) and the volume of the draft tube cone $\left(V_{cone} \right)$. The latter is known from the test rig geometry and the vortex rope volume hence becomes

$$V_{c,n} = \left(\frac{A_{c,n}}{A_{cone}} \right)^2 \cdot V_{cone}. \tag{2.11}$$

2.4 Periodic oscillations in the hydraulic system

2.4.1 Pressure and flow rate

For the operating conditions at OP#A, an auto-oscillation of the hydraulic system is observed. This unstable behavior is revealed by the characteristic repetitive collapse and growth of the vortex rope, accompanied by periodic draft tube pressure fluctuations of significant amplitude. Figure 2.4 shows the raw and low pass filtered wall pressure factor for p_2 (see Figure 2.4a), together with the power spectral density of the filtered signal (see Figure 2.4b). For the analysis in the frequency domain and the calculation of the discharge using eq. (2.7), the filtered wall pressure factor is used, due to the high noise content of the raw signal. The pressure fluctuations reach up to 10% of the specific energy at OP#A and the dominant surge frequency peak is situated at 10% of the runner frequency.

(a) Wall pressure c_p (b) Power spectral density P_{xx}
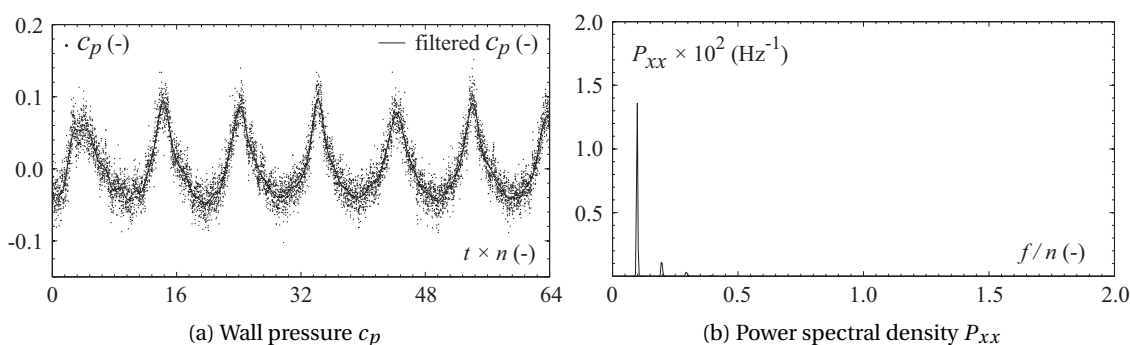
Figure 2.4: Wall pressure signal as a function of the number of runner revolutions together with corresponding power spectral density of the filtered signal for OP#A.

A systematic variation of the draft tube pressure level is performed at OP#A. Figure 2.5 shows the behavior of the dominant surge frequency and amplitude for ten different σ-values. Similar to the observations made during the reduced scale model testing, documented in Section 1.1.3, the frequency changes linearly with the cavitation number. The amplitude appears again to oscillate around the first order fit (dashed line). The vortex rope oscillates however at a lower fraction of the runner frequency compared to the reduced scale model.

The upstream and downstream flow rate fluctuations are calculated by using the pressure differentials p_{A-B} and p_{C-D} for Q_1 and Q_2, respectively, with the method introduced in Section 2.3.2 (see Figure 2.1 for the measurement locations of p_A, p_B, p_C and p_D). Figure 2.6 shows the results for six different values of the cavitation number σ around OP#A, together with the wall pressure factor for p_2. As mentioned earlier, the mean value of the discharge cannot be obtained with this method. Hence, the fluctuating parts of Q_1 and Q_2 are plotted around an arbitrary reference value, which is chosen to be the mean discharge in the test rig measured by the electromagnetic flow meter. The integration of eq. (2.7) is performed numerically by applying the Simpson's rule [57]. For all presented cases, the downstream flow rate fluctuation Q_2 is significantly higher than the upstream equivalent Q_1. The peak-to-peak amplitude of Q_2

27

(a) Waterfall diagram

(b) Fundamental frequency evolution

(c) Fundamental amplitude evolution
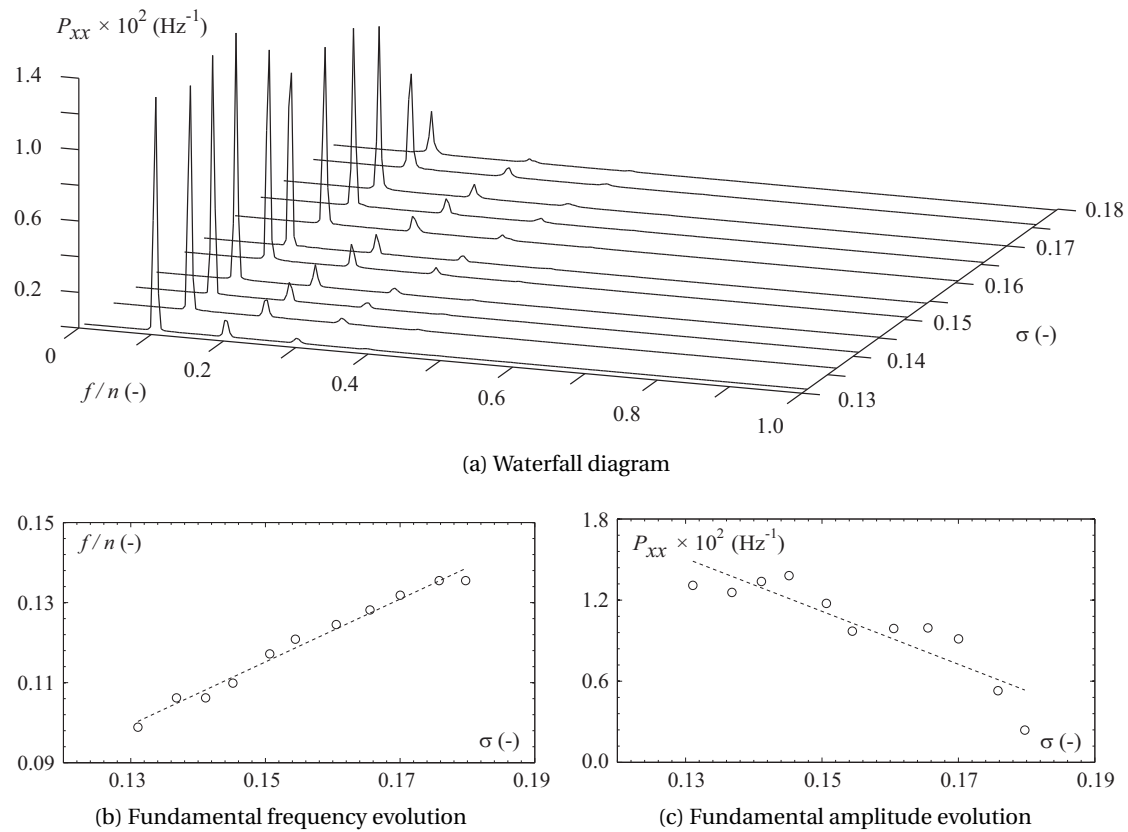
Figure 2.5: Power spectral densities of c_p at p_2 and evolution of the dominant surge frequency and amplitude for different σ-values.

is furthermore decreasing with an increasing σ, that is to say for a growing draft tube pressure level and hence a declining volume of the vortex rope.

2.4.2 Vortex rope volume

Figure 2.7 shows snapshots of the flow visualization at OP#A with a high speed camera in the draft tube cone. It is observed that the vortex rope almost completely disappears and reappears during each cycle, as observed on the reduced scale physical model in Chapter 1. Also, the collapse of the cavity is rather sudden and short compared to its longer lasting growing phase. The illustrated cycle is situated between the second and third peak of the wall pressure signal in Figure 2.4a.
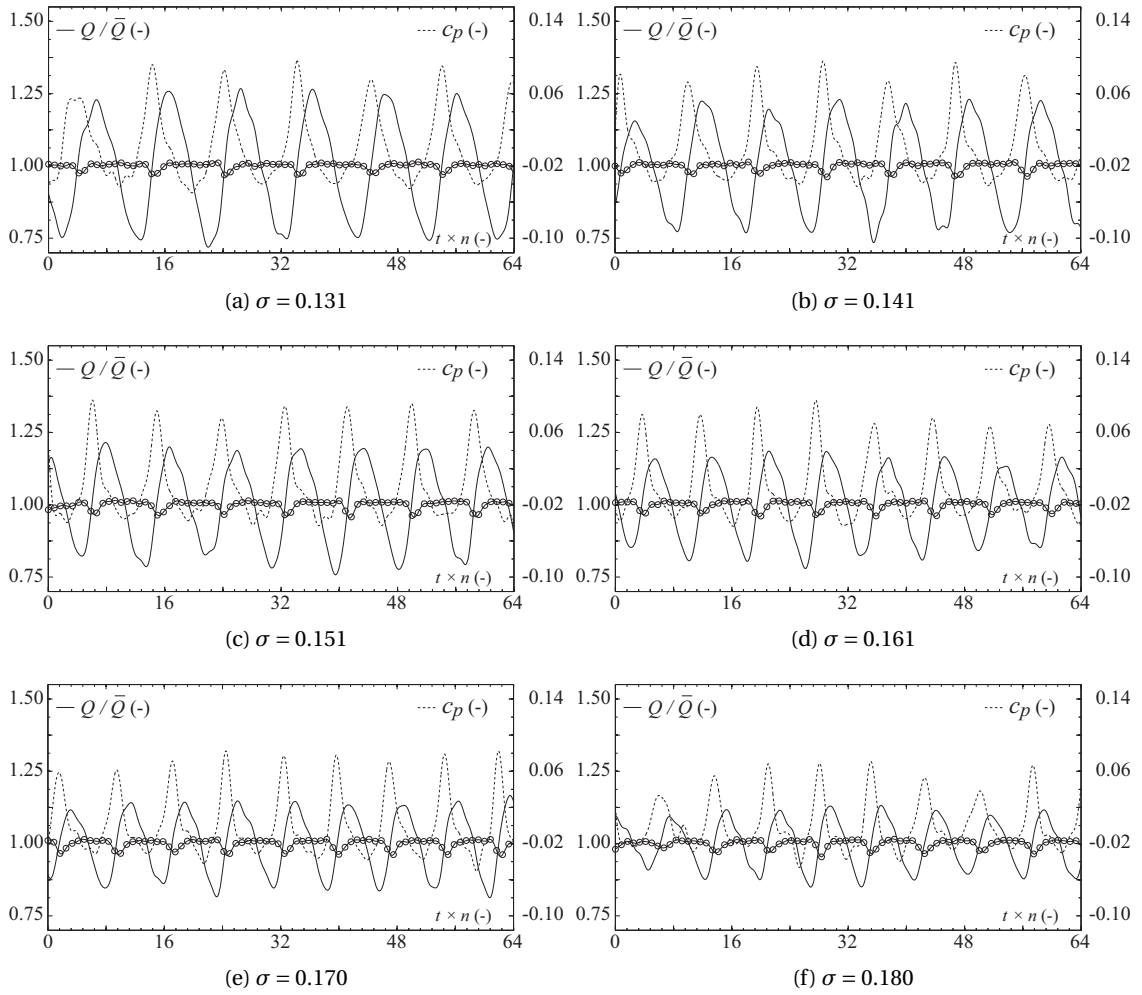
Figure 2.6: Fluctuation of Q_1 (∘-markers) and Q_2 (solid lines) together with c_p at p_2 (dashed lines) as a function of the number of runner revolutions.

(a) $t = 0$

(b) $t = 0.11 \cdot T$

(c) $t = 0.22 \cdot T$

(d) $t = 0.33 \cdot T$

(e) $t = 0.44 \cdot T$

(f) $t = 0.55 \cdot T$

(g) $t = 0.66 \cdot T$

(h) $t = 0.77 \cdot T$

(i) $t = 0.88 \cdot T$

(j) $t = T$
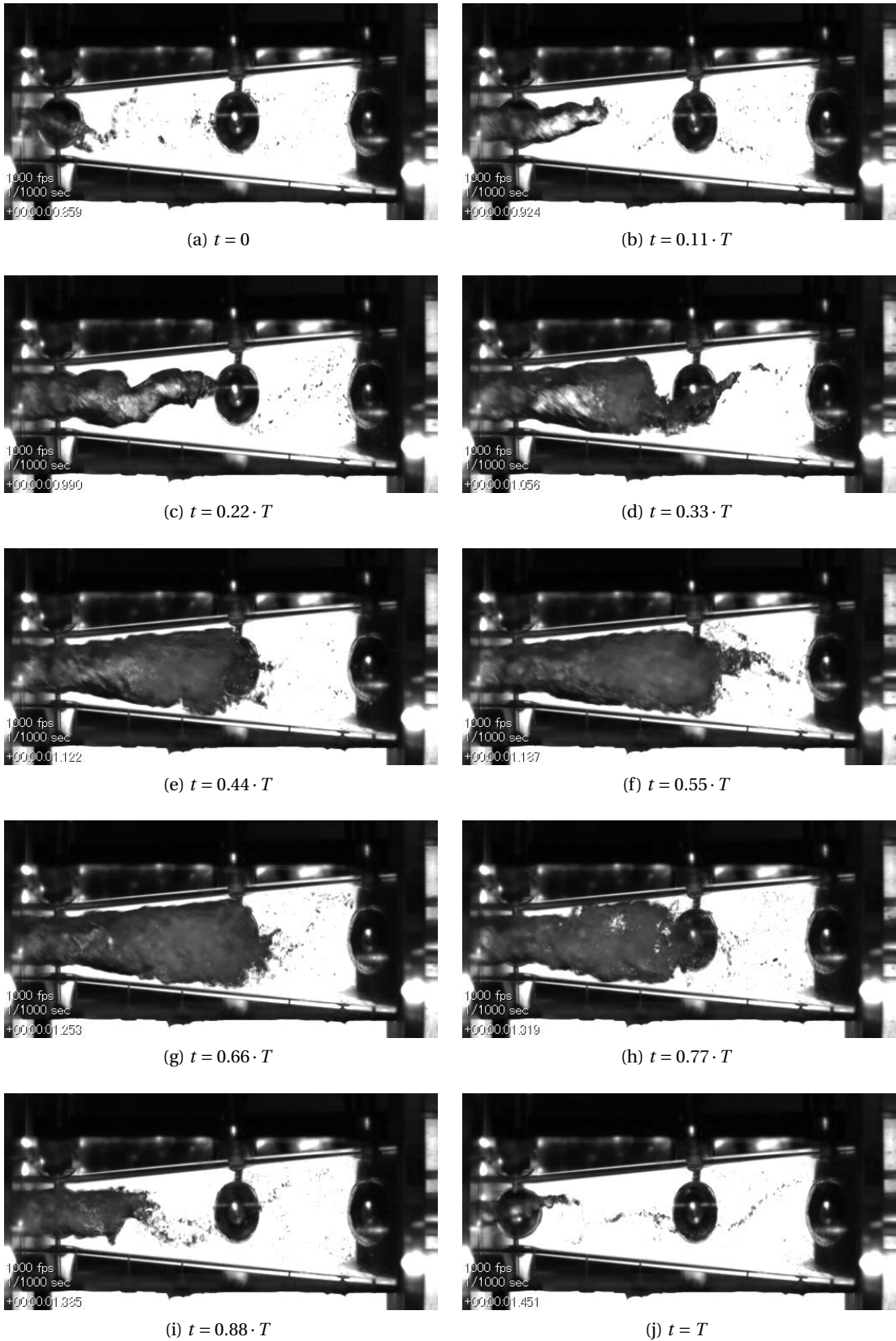
Figure 2.7: Draft tube flow visualization at OP#A.

With the method presented in Section 2.3.3, the change in the area occupied by the vortex rope ΔA_c is calculated for the visualization at OP#A shown in Figure 2.7. Figure 2.8 shows the raw data and a low pass filtered version. The instant, raw ΔA_c in Figure 2.8a is highly fluctuating and the maximum amplitudes of the low pass filtered data in Figure 2.8b are more than four times lower. However, the qualitative behavior seems to be well reproduced and the periodicity is respected. This is confirmed by an inspection of the video material, showing that the zeros of the low pass filtered curve on a rising and falling edge accurately define the stages where the vortex rope volume reaches its minimum and maximum, respectively.

(a) Raw and filtered ΔAc (b) Filtered ΔAc
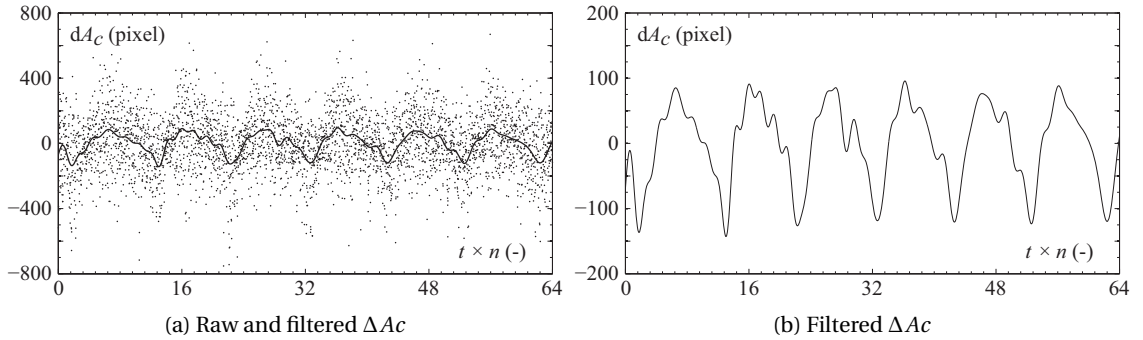
Figure 2.8: Left: Raw ($\cdot$ markers) and low passed filtered (solid line) ΔA_c for OP#A. Right: Rescaled low pass filtered ΔA_c.

Based on eq. (2.11), the instantaneous vortex rope volume may now be estimated. Figure 2.9 shows the evolution of the vortex rope volume V_c together with the wall pressure factor at p_2 for six values of the cavitation number σ. The volume is made non dimensional by the total volume of the draft tube cone V_{cone}. A first inspection reveals a very regular phase relationship with the pressure signal. The volume of the cavity reaches its maximum when the pressure is at its minimum, whereas the vortex rope collapse is matched by the position of the pressure peaks. The volume V_c in Figure 2.9a fluctuates between 20% and 50% of the total volume of the cone, which appears realistic in view of the corresponding flow visualization presented in Figure 2.7. However, the minimum volume seems to be slightly overestimated.

A few drawbacks and potential sources of error of the presented method for the estimation of the vortex rope volume have to be discussed. First of all, the volume is generally underestimated due to the fact that the first segment of the straight part of the diffuser in Figure 2.2 consists of a nontransparent metal flange, hiding a fraction of the vortex rope. Secondly, a periodic error is introduced when the cavity overlaps with the pressure sensors in the background of the picture frames. For the visualization performed at OP#A, this is the case, for instance, in Figure 2.10a and Figure 2.10b, where the vortex rope partly covers the pressure sensors p_4 and p_5, respectively. The corresponding masked binary images are shown in Figure 2.10. When calculating the difference with respect to the adjacent frames, the entire permanently white area corresponding to the pressure sensors in the background is subtracted. Consequently, the proportion of the vortex rope volume overlapping with the sensors is ignored in the calculation

(a) $\sigma = 0.131$

(b) $\sigma = 0.141$

(c) $\sigma = 0.151$

(d) $\sigma = 0.161$

(e) $\sigma = 0.170$

(f) $\sigma = 0.180$
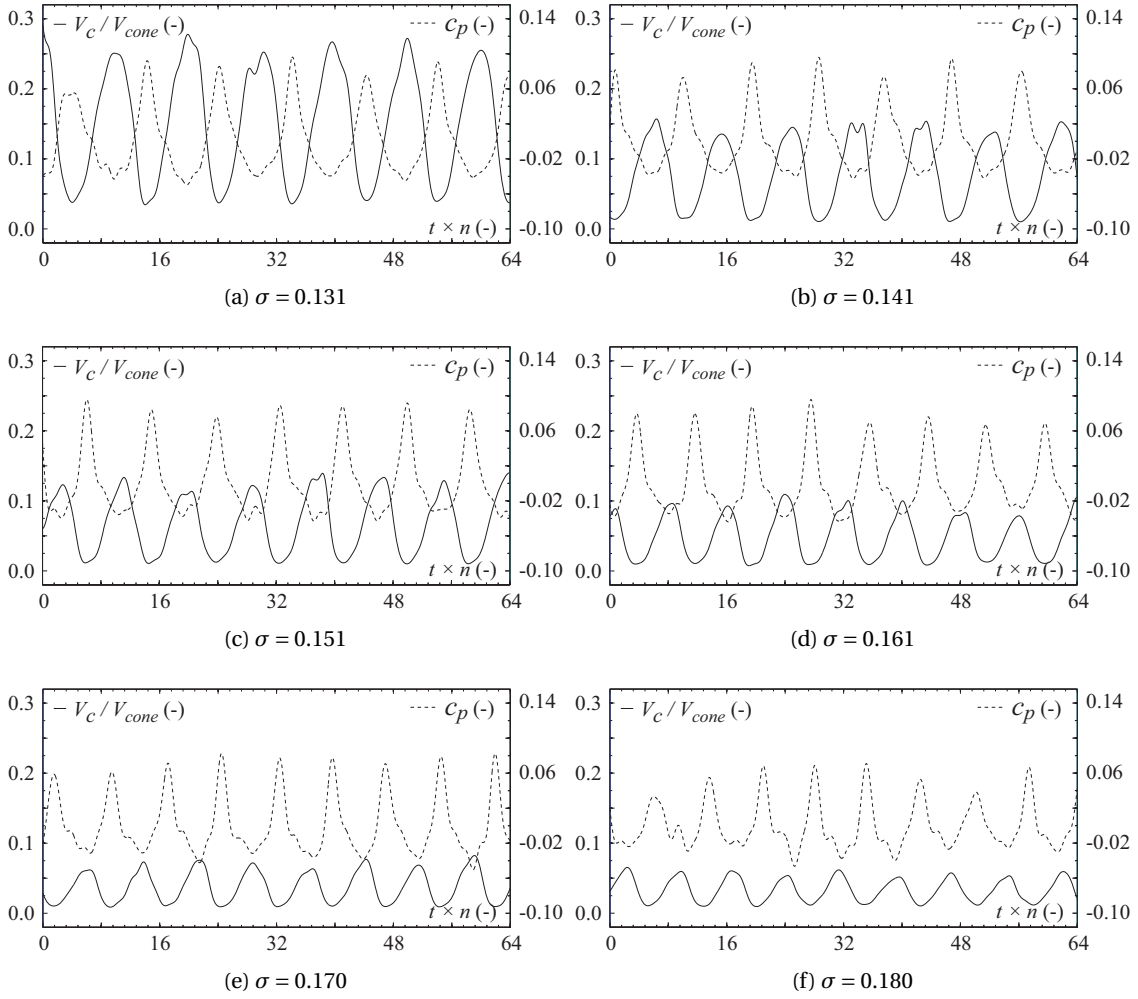
Figure 2.9: Fluctuation of V_c (solid lines) together with c_p at p_2 (dashed lines) as a function of the number of runner revolutions for different σ-values.

of the differential surface ΔA_c. Furthermore, as can be observed in Figure 2.3b, reflections of the ambient light on the surface of the cavity occasionally transform into black pixels and therefore falsify the count. Finally, the mean value of the volume V_c depends essentially on $A_{c_{ref}}$. This surface is estimated by counting the pixel inside a polygon around the edge of the cavity, for which the vertices are defined manually in the corresponding image at t_{ref}. This is potentially limiting the precision of the method.

(a) $t = 0$ (b) $t = 0.77 \cdot T$

Figure 2.10: Masked binary images of two instances where the vortex rope overlaps with the pressure sensors p_4 and p_5 from Figure 2.7.

2.5 Hydroacoustic characterization of the test rig

The possibility of instantaneously following the vortex rope volume, the upstream and downstream flow rates and the cavitation number, enables the estimation of the hydroacoustic draft tube flow parameters according to Section 1.2.2. It has to be mentioned that an exact calculation is not possible, since the partial derivatives in eq. (1.3) with respect to a given state variable are performed by keeping the remaining two variables constant. These conditions are evidently not met on the test rig.

In a first step, the flow rate and the cavitation number, as well as the calculated vortex rope volume, are averaged with respect to the dominant wall pressure phase. This offers an additional physical insight by revealing how the vortex rope volume V_c changes as a function of Q_1, Q_2 and σ during one period of the pressure oscillation. The HA parameters are finally deduced from the slope of these curves.

2.5.1 Mean phase averaged flow variables

The term *mean phase average* refers to a characteristic mean variation of a periodic signal by calculating the average over all its recorded cycles. This requires the definition of an instant phase, allowing to identify the individual cycles and to split up the raw signal accordingly in order to determine its average. The method is described in detail in Section 3.3.4 and has been used by several researchers in the past for similar applications [5, 8, 50]. For illustration purposes, the length of the signal in Figure 2.11a is limited to 64 runner revolutions. However, the total amount of cycles taken into account for the calculation of the mean phase average in Figure 2.11b is 97.

Figure 2.12 shows the mean phase averaged vortex rope volume V_c, the flow rates Q_1 and Q_2 as well as the cavitation number σ for OP#A. All the corresponding signals were divided into their individual cycles with respect to the same instant phase from the wall pressure, represented in Figure 2.11a by the dashed line. It is noted that the number of cycles taken into

33

(a) Filtered c_p with instant phase

(b) Mean phase averaged c_p
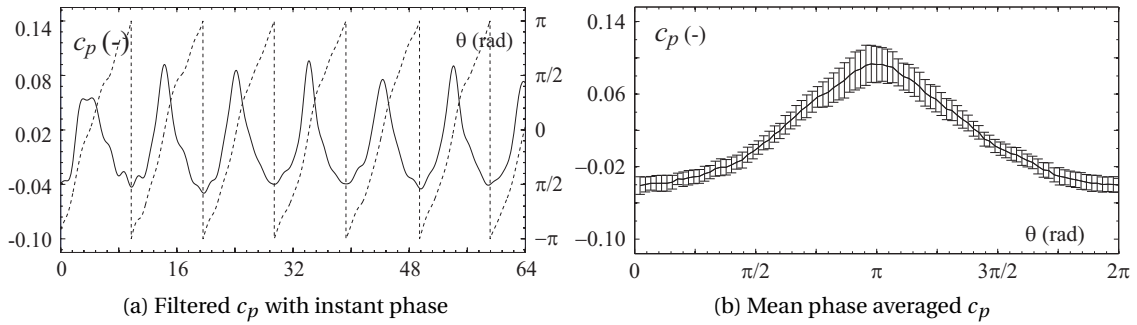
Figure 2.11: Mean phase average of the filtered c_p at p_2 for OP#A. The dashed line represents the instant phase of the wall pressure signal and the vertical error bars the standard deviation.

account varies significantly between the calculation of V_c based on the high speed visualization (total acquisition time 5 s) and the calculation of Q and σ based on the analogue data (total acquisition time of 60 s). Since all the signals are averaged with respect to the same pressure reference signal, the resulting phase relationships may directly be compared to each other. The volume is made non-dimensional with the volume of the draft tube cone and the flow rates are made non-dimensional with the mean discharge measured in the test rig.

(a) Vortex rope volume V_c

(b) Upstream flow rate $Q_1/\bar{Q}$

(c) Cavitation number σ

(d) Downstream flow rate $Q_2/\bar{Q}$
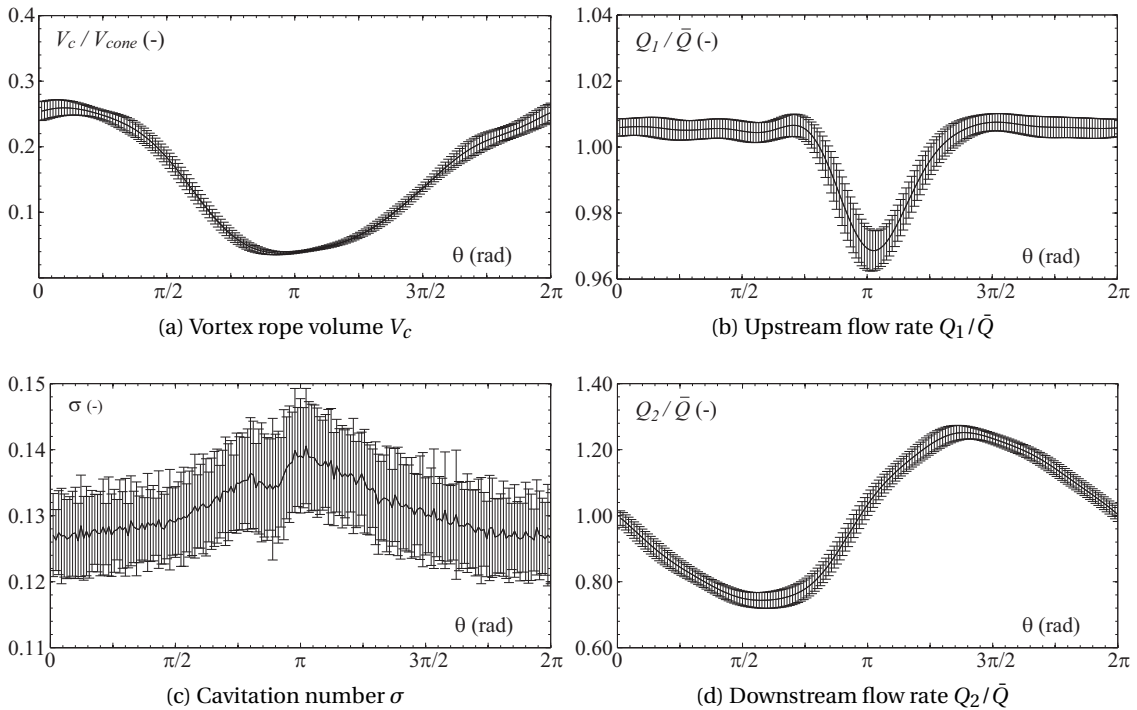
Figure 2.12: Pressure phase averaged V_c, Q_1, Q_2 and σ for OP#A.

2.5.2 Calculation of the HA parameters

Vortex rope evolution as a function of the flow rate and the cavitation number

In order to visualize the behavior of the hydroacoustic parameters χ_1, χ_2 and C_c, the vortex rope volume V_c is first plotted against the upstream and downstream flow rates Q_1 and Q_2 in Figure 2.13a, as well as against the cavitation number σ in Figure 2.13b. The graph $V_c(Q_2)$ approximately forms an ellipse, with its major and minor axis being defined by the peak-to-peak amplitudes of the downstream flow rate and the vortex rope volume oscillation, respectively. On the other hand, the $V_c(Q_1)$-curve is a vertical straight line during most of the V_c-variation, with only a small tear-shaped deflection when the vortex rope is at its minimum volume.

The mean phase averaged $V_c(\sigma)$-evolution seems to be well approximated by a straight line with a slightly negative slope. An elevated noise level in the signal of the cavitation number σ is observed, expressed by higher standard deviation values in Figure 2.12c and large σ fluctuations in Figure 2.13b. This is due to the fact that the calculation of σ is based on a raw pressure signal, where as the other quantities on display are based on filtered signals.

The same representation is shown for five other cavitation numbers in Figure 2.14 and Figure 2.15. The variation of the upstream flow rate Q_1 seems to increase with an increasing cavitation number σ, which is reflected by a more important size of the above described tear-shaped area attached to the vertical straight section. The contrary is observed for Q_2, where the main axes of the ellipse formed by $V_c(Q_2)$ are shortened by an increasing cavitation number σ. The slope of $V_c(\sigma)$, representing the cavitation compliance C_c, appears to decrease with a decreasing mean volume and an increasing σ.

(a) $V_c(Q_1)$ and $V_c(Q_2)$

(b) $V_c(\sigma)$
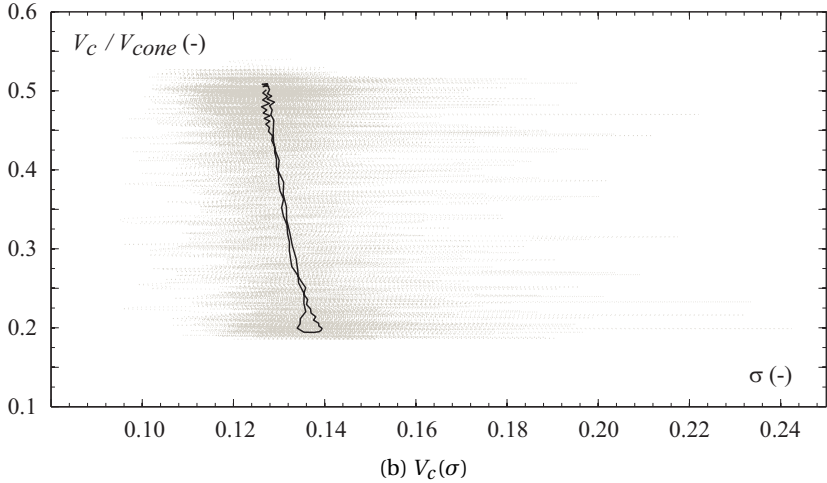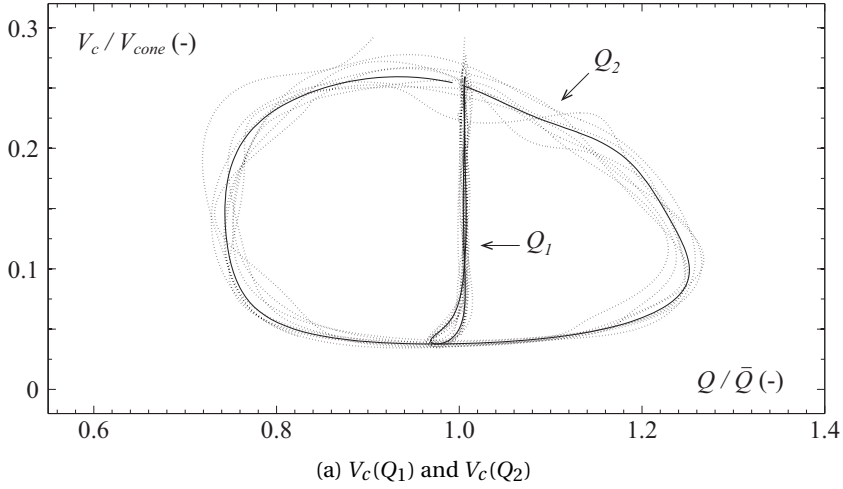
Figure 2.13: Vortex rope volume as a function of the raw (dotted lines) and pressure phase averaged (solid lines) upstream and downstream flow rates and cavitation number at OP#A.
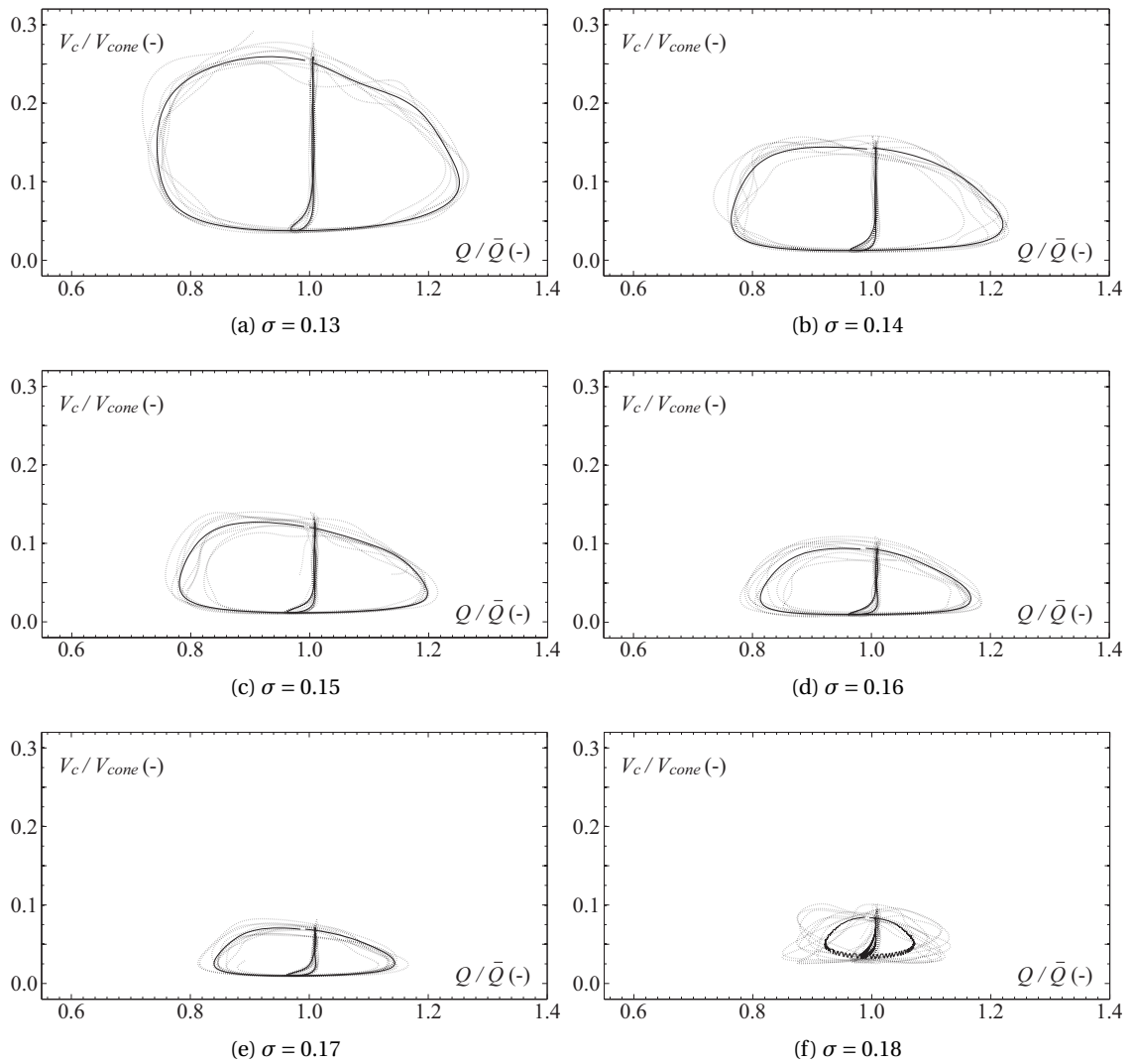
Figure 2.14: V_c as a fct. of the raw (dotted lines) and pressure phase averaged (solid lines) upstream and downstream flow rates for several cavitation numbers around OP#A.
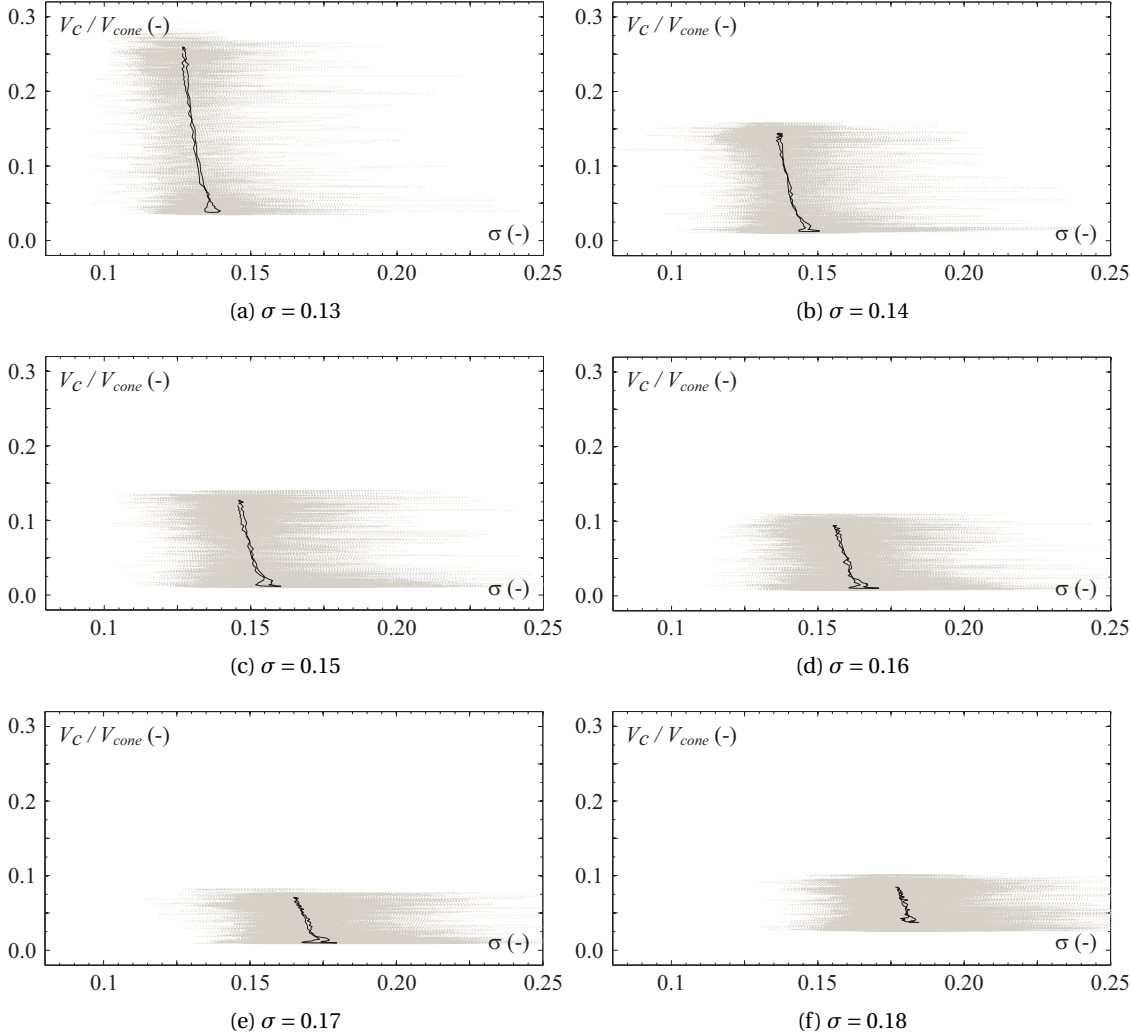
Figure 2.15: Vortex rope volume as a function of the raw (grey tone) and pressure phase averaged (solid lines) cavitation number for several cavitation numbers around OP#A.

Approximation of χ_1, χ_2 and C_c

The shape of the functions $V_c(Q_1)$ and $V_c(Q_2)$ in Figure 2.14 inevitably produces singularities in their derivatives. This is shown in Figure 2.16, plotting the pressure phase averaged up and downstream flow gain factors against a dimensionless time, normalized by the mean period over all the V_c-cycles. Quantitative statements about the value, the sign or the trend of χ_1 and χ_2 are therefore of limited worth. This is underlined by the corresponding mean values obtained by time-wise integration of the pressure averaged curves, reported in Table 2.1.
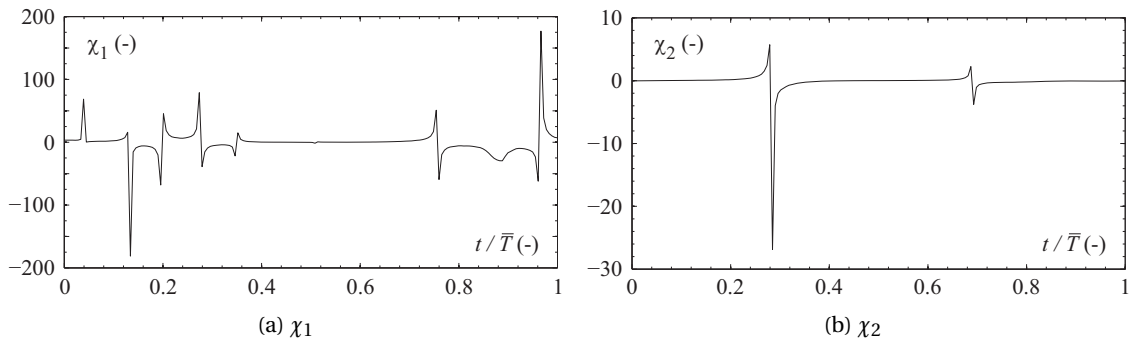
Figure 2.16: Pressure phase averaged mass flow gain factors at OP#A.

As mentioned earlier, the variation of the vortex rope volume with respect to the cavitation number in Figure 2.15 seems fairly linear, and so a first order fit of the pressure phase averaged $V_c(\sigma)$-curves in a least square sense is performed. According to eq. (1.9), the slope of the resulting straight line divided by the hydraulic head H is equal to the cavitation compliance C_c. Furthermore, C_c may be linked to the speed of sound in the draft tube through classical pipe flow theory [65, 44], stating that

$$C_c = \frac{g \cdot A \cdot l}{a^2} \, , \tag{2.12}$$

where A and l are the area and the length of a reference pipe section. The values for both the compliance and the sound velocity are included in Table 2.1. Similar to the quasi-static (QS) approach performed by the author [41], the cavitation compliance may be estimated over the tested σ-range with the mean vortex rope volumes, shown in Figure 2.17. The first and the last values being far off the general trend, they are not considered for the calculation of the linear approximation (dashed line). The results are documented in the last column of Table 2.1. The values obtained by the instantaneous and the quasi-static approach display a substantial difference.
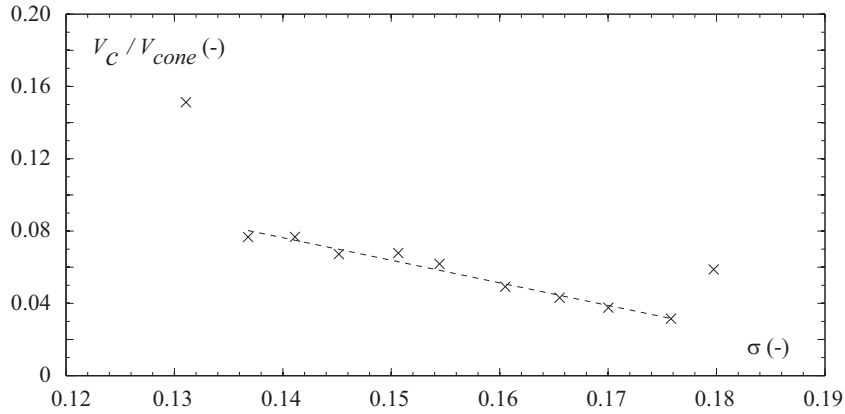
Figure 2.17: Mean vortex rope volumes for several σ-values (cross markers) with linear fit (dashed line) around OP#A.

Table 2.1: Hydroacoustic parameters of a simplified test rig with a micro-turbine for OP#A.

σ	0.131	0.141	0.151	0.161	0.170	0.180	QS approach
χ_1 (s)	-0.217	-12.09	0.319	-0.034	0.082	-0.145	-
χ_2 (s)	-0.132	-0.021	0.002	0.039	-0.001	-0.020	-
$|C_c| \times 10^3$ (m^2)	6.486	3.664	3.082	2.277	1.608	2.379	0.411
a (m·s^{-1})	4.587	6.103	6.650	7.741	9.212	7.574	18.21

2.5.3 Passage from stable to unstable configuration

As explained in Section 1.1.4, a minor variation of the operating conditions may have a considerable impact on the flow parameters at the limits of the stability domain. Given the critical role of the sound velocity on the onset of pressure surge, the switch from one state to the other can be provoked by changing the cavitation number σ and hence the fraction of vapor in the draft tube. This transition can be for instance be observed by increasing the cavitation number beyond the range displayed in Figure 2.5. A first indication is found during the study of the vortex rope volume as a function of the flow rate, where the behavior for the highest σ-value in Figure 2.14f diverges from the lower values. The inspection of the corresponding pressure fluctuations in Figure 2.18a reveals the reason. The oscillation loses its self-excited character twice, dropping to significantly lower peak-to-peak amplitudes. A further increase of the cavitation brings forth a completely stable configuration, as shown in Figure 2.18b. A graphic study of the hydroacoustic parameters similar to the one in Figure 2.14 and Figure 2.15 with a mean phase average becomes harder to implement, since the instant pressure phase used to isolate the single cycles does not produce clearly distinguishable periods anymore, due to the loss of regularity in the signal.
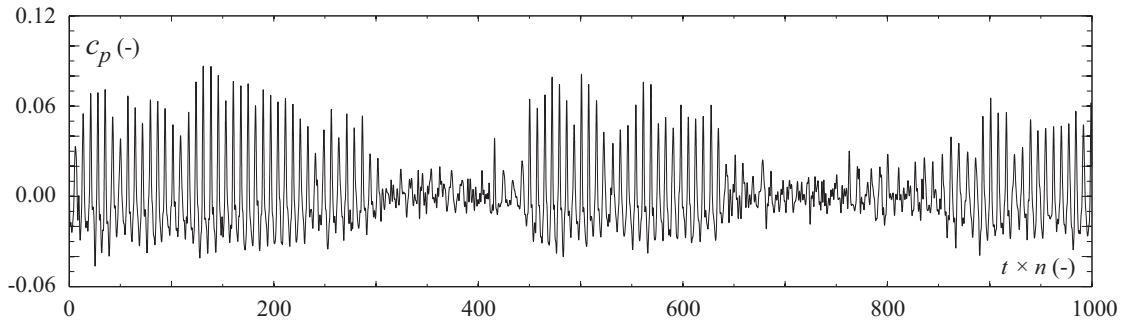
(a) c_p at OP#A-10, $\sigma = 0.18$
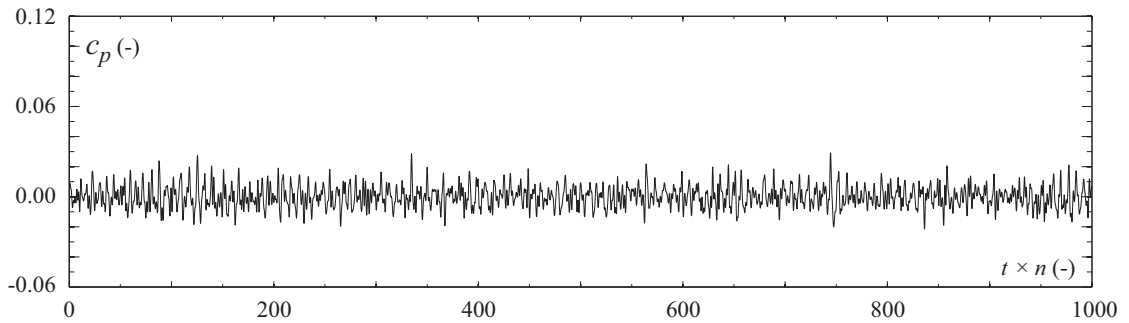
(b) c_p at OP#A-12, $\sigma = 0.19$

Figure 2.18: Wall pressure factor c_p from the sensor p_2, plotted against the number of runner revolutions.

The evolution of the vortex rope volume and the upstream and downstream flow rates at the stable configuration of $\sigma = 0.19$ is presented in Figure 2.19. Unsurprisingly, it is observed that both the volume and flow rate fluctuations are marginal compared to the ones in Figure 2.6 and Figure 2.9 for an unstable flow configuration.

(a) $V_c(n \times t)$ and $c_p(n \times t)$

(b) $Q_1(n \times t)$, $Q_2(n \times t)$ and $c_p(n \times t)$
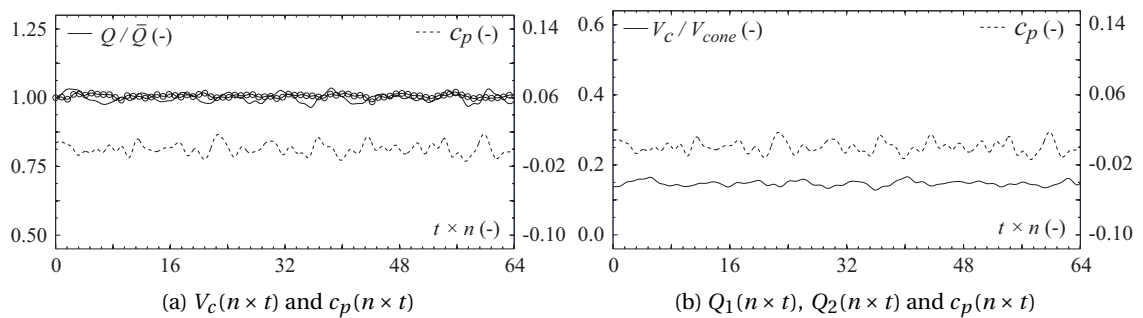
Figure 2.19: Vortex rope volume and upstream ($\circ$-markers) respectively downstream (solid line) flow rate as a function of the runner revolutions at OP#A-12 ($\sigma = 0.19$).

2.6   Summary and discussion

A self-sustained pressure oscillation similar to the one observed on a reduced scale physical model in Chapter 1 is reproduced on a simplified test configuration featuring a micro-turbine and a horizontal conical diffuser. The main characteristics in terms of the wall pressure and vortex rope fluctuation are comparable. As for the previous case, the dominant pressure fluctuation frequency and the corresponding amplitude is found to vary linearly with the cavitation number.

A method for estimating the instant vortex rope volume based on high speed flow visualization is introduced and successfully applied. Together with the upstream and downstream flow rates obtained from differential pressure measurements, the temporal variations of V_c, Q_1 and Q_2 are obtained. The upstream discharge varies significantly less than its downstream counterpart. The phase relationships between pressure, volume and discharge are constant throughout the total period of the data acquisition.

Together with an instantaneous record of the cavitation number, the functions $V_c(Q_1)$, $V_c(Q_2)$ and $V_c(\sigma)$ are drawn up. Their graphical representation clarifies how the mass flow gain factors and the cavitation compliance vary over one period of the pressure oscillation. While C_c is fairly well approximated by a constant value, χ_1 and χ_2 feature several singularities due to the partly circular shape of $V_c(Q_1)$ and $V_c(Q_2)$. This highlights the difficulty of representing the mass flow gain factors by a constant value in a one-dimensional model. Numerical values calculated for C_c at several cavitation numbers confirm the steady decrease of the sound velocity with an increasing mean vortex rope volume.

Studying the shape of $V_c(Q_1)$, it is observed that nearly the entire span of the vortex rope volume is crossed during a very small variation of the corresponding flow rate Q_1. This suggests that minor swirl variations at the runner outlet, being directly linked to the upstream discharge through the velocity triangles, may have a decisive destabilizing effect on the draft tube flow. It is however to be expected that the characteristic shape of the $V_c(Q)$ and $V_c(\sigma)$ curves as well as the discharge ratio Q_1/Q_2 depend on the design of the hydraulic circuit. Based on the collected data it cannot be determined if the results are similar for a different relative position of the turbine within the circuit, for instance, or for a different runner size. The results are therefore not directly transposable to another test case.

3 Draft tube flow investigation

3.1 Introduction

The flow in the draft tube of a hydraulic machine during self-sustained pressure oscillations at full load is characterized by its complex, unsteady and two-phase nature. This chapter aims at providing a detailed description of the flow field in terms of the axial (meridional) and tangential velocity components Cm and Cu. This is achieved by performing Laser Doppler Velocimetry (LDV) as well as 2-D fluorescent Particle Image Velocimetry (PIV) measurements in the draft tube cone. The LDV offers a local simultaneous measure of the axial and tangential velocity components, whereas the PIV provides the axial and radial velocity field over a predefined target area in a resolution depending on various parameters. Measurements are performed in cavitation-free conditions as well as in presence of an oscillating vortex rope. The resulting velocity profiles at several streamwise locations are used to establish the mass and angular momentum balance in the draft tube. Finally, the instantaneous volume of the vortex rope is estimated based on high speed visualizations. The test case is identical to the one in Chapter 1 and the setup of the reduced scale physical model of a Francis turbine on the EPFL test rig PF3 at the Laboratory of Hydraulic Machines is shown in Figure 1.1.

3.2 Experimental setup

3.2.1 Laser Doppler Velocimetry

The local variation of the tangential and axial velocity components is measured with a state of the art LDV system shown in Figure 3.1. The Laser probe is set up in two different configurations, respectively parallel and perpendicular to the inlet pipe, as shown in Figure 3.3. In order to ensure an ideal optical access and to facilitate the calculation of the position of the measurement volume in the draft tube cone, circular optical windows with an anti-reflection coating adapted to the wavelength of the Laser are installed. A remotely controlled traversing system is used for the vertical and radial displacement of the Laser.
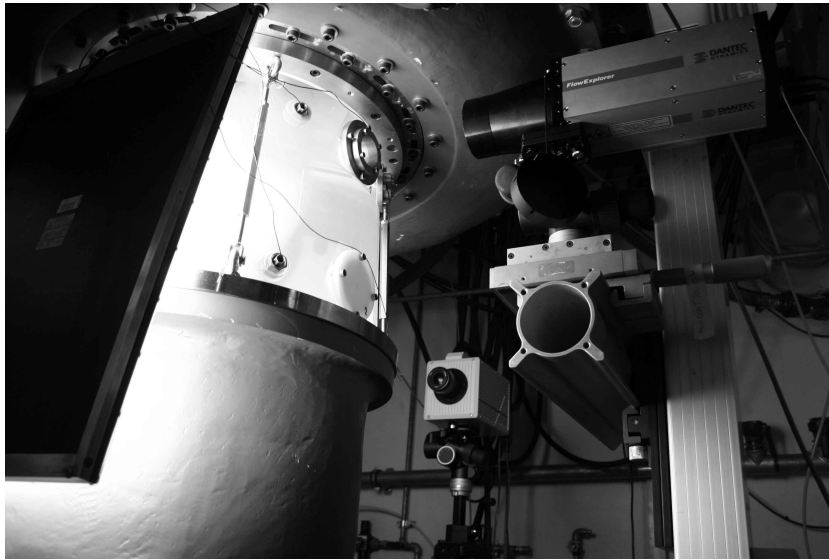
Figure 3.1: Photo of the measurement setup around the draft tube cone with LED backlight panel to the left, LDV probe to the right and high speed camera in the back.

Table 3.1: Technical specifications of the LDV equipment

Optical head	
Model	Dantec FlowExplorer
Type	2 component factory-aligned probe
Wavelength	660 nm (Ch. 1) & 785 nm (Ch. 2)
Energy	35 mW per channel
Beam diameter	2.5 mm
Focal length	500 mm
Control volume in air	$0.1684 \times 0.1681 \times 2.806$ mm (Ch. 1)
	$0.2003 \times 0.1999 \times 3.338$ mm (Ch. 2)
Signal processor	
Model	Dantec F60 FlowProcessor
Type	Burst Spectrum Analyzer

The measurements are performed at two streamwise positions, referred to as Section 1 and Section 2 in Figure 3.2. The corresponding horizontal cross-sections of the draft tube cone, both including four equally spaced wall pressure sensors mounted on the circumference, are shown in Figure 1.3a.

The measurement setup and the chain of acquisition is schematized in Figure 3.3. An external trigger from the BSA is used to set off the wall pressure measurements, assuring a perfect synchronization. The water is seeded with 10 μm hollow glass sphere particles at a fairly low density, since various impurities and bubbles present in the flow already produce a considerable number of valid bursts in the measurement volume at the intersection of the Laser beams.
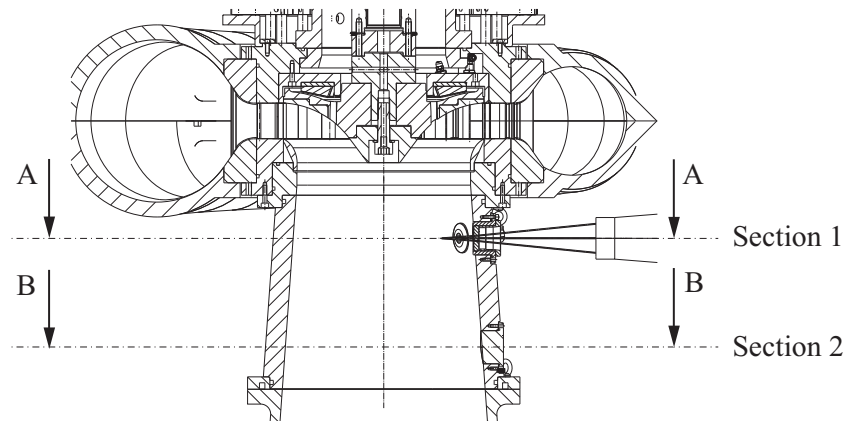
Figure 3.2: Side view of the draft tube cone with optical LDV probe.

3.2.2 Particle Image Velocimetry

Test arrangement

Figure 3.4 shows the setup for the PIV measurements with the upstream feeding pipe, the spiral case, the Plexiglas draft tube cone, the elbow and the diffuser. A water filled window is installed between the camera and the target area in the cone center, so as to minimize the optical distortion effects. The Laser is mounted parallel to the inlet pipe. The technical details of the PIV equipment are summarized in Table 3.2.

Table 3.2: Technical specifications of the PIV equipment

Laser	
Model	New Wave Minilase III-15
Type	Frequency doubled Q-switched Nd:YAG
Wavelength	532 nm
Energy	< 32.5 mJ
Beam diameter	3.5 mm
Camera	
Model	Dantec FlowSense EO 4M
Resolution	2048 x 2048 pixels
Pixel Size	7.4 μm
Lens	24 mm
Filter	long pass (>570 nm)
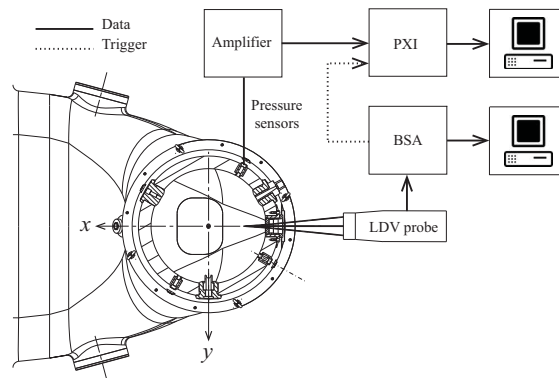
(a) Laser parallel on y-axis, parallel to the inlet pipe
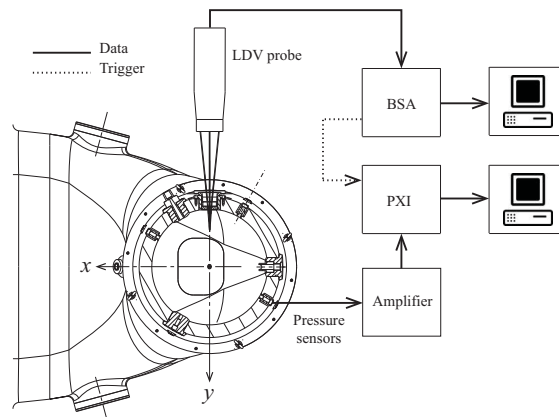
(b) Laser on x-axis perpendicular to the inlet pipe

Figure 3.3: Horizontal cut of the draft tube cone at $0.39 \times D_{\bar{1}}$ below the runner exit (Section 1) together with the data acquisition chain for x-axis and y-axis LDV surveys.
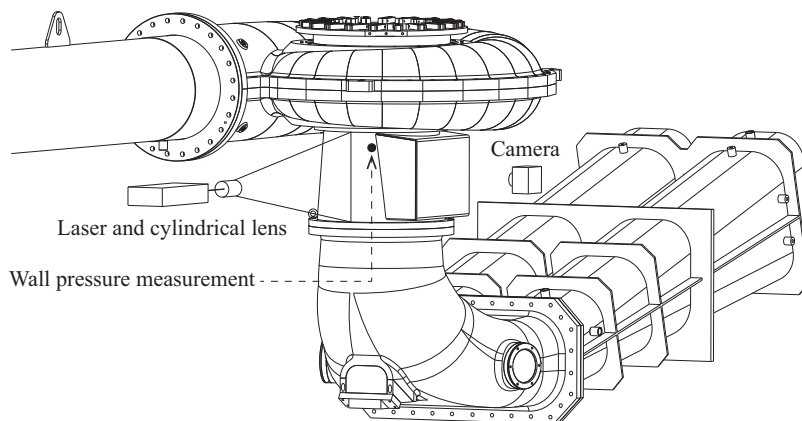
Figure 3.4: Experimental setup for the PIV measurements in the draft tube cone from [43].

Calibration

The target area measures roughly 20 cm x 20 cm and is located in a meridional plane of the draft tube cone, starting $0.464 \times D_{\bar{1}}$ below the runner exit. For the calibration, an Imaging Model Fit is performed with a 200×200 mm dotted disk, which is attached to the runner nose.

Seeding material

The use of a Laser device in a two-phase environment is challenging, since the light sheet is reflected on the surface of the gaseous phase. Possible consequences reach from significant measurement errors to a damage of the measurement equipment due to the overexposure of the camera's image sensors. Therefore, fluorescent seeding material is used together with a suitable long pass filter for the camera. Since commercially available products tend to be too expensive in view of the considerable water volume of about 30 m^3 in the test rig, an alternative procedure is introduced to obtain fluorescent particles from common polyamide particles and Rhodamine-B dye. The method is described in detail by the author in [43] and led to very satisfying results in terms of the optical properties and the life span of the particles.

Measurement procedure and pressure synchronization

The measurement procedure with the acquisition chain is schematized in Figure 3.5. With the ultimate goal of establishing the change in the velocity components and the discharge during a whole period of the vortex rope pulsation, several measurements are taken at different instants. In order to assign each of these measuring points a stage in the pressure cycle, one of the wall pressure signals is taken as a reference, since it provides an accurate notion of the oscillation's periodicity. The corresponding sensor is connected to an oscilloscope, which generates a square TTL signal, triggered at a predefined voltage level at each falling edge of the wall pressure. This is illustrated in Figure 3.6.

The TTL signal from the oscilloscope is then used as a trigger for the PIV system via its timing box. Since the user interface allows defining a trigger delay value, i.e. a delay between the trigger and the start of the measurement, an arbitrary amount of measurement points with different trigger delays can be defined. At each of these measurement points, forty consecutive image pairs are recorded in order to calculate a mean velocity field. Then, the trigger delay is set to another value and the procedure is repeated. The time between two acquisitions forming one pair of images is 100 μs. Based on the tangential velocity components measured by LDV, it can be assumed that the vast majority of particles remains in the measurement plane, characterized by a light sheet thickness of approx. $2 - 3$ mm, during this time.
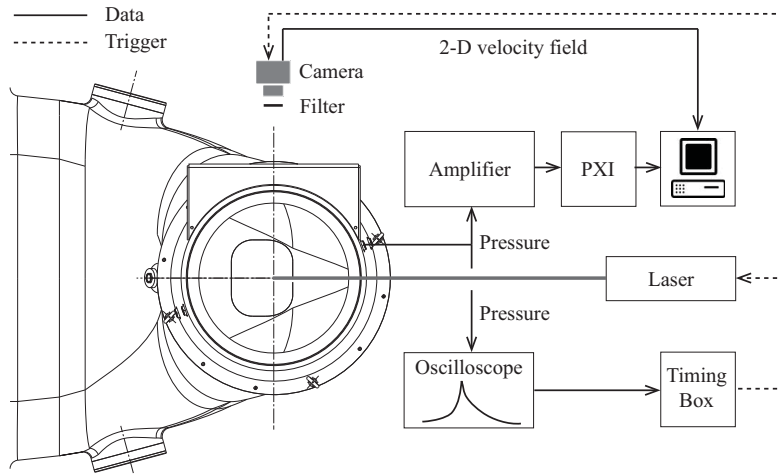
Figure 3.5: Section of the draft tube cone at $0.39 \times D_{\bar{1}}$ from the runner outlet, together with the data acquisition chain for the PIV measurements from [43].
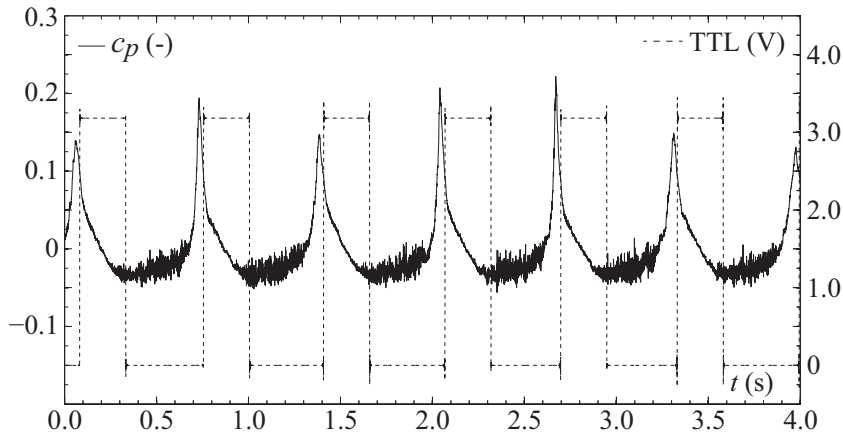
Figure 3.6: Wall pressure factor c_p (C1N) with TTL signal generated by the oscilloscope for externally triggered PIV measurements.

3.2.3 High speed flow visualization

The Plexiglas cone provides an optical access to the flow in the reduced scale model. This enables, one one hand, the study of the vortex rope behavior in the draft tube, and on the other hand the observation of the cavitation formed on the runner blades. For both cases, the two-phase flow is recorded with a high speed camera. For the visualization of the vortex, a highly uniform LED screen is installed as a back light. The LED source produces an excellent contrast between the gaseous and the liquid phase and therefore considerably facilitates the image processing in 3.3.1. For the blade cavitation, the cone runner outlet is illuminated with a stroboscope, which is synchronized with the high speed camera so that an image frame is recorded following each flash of the strobe. The technical specifications of the equipment are summarized in Table 3.3. The camera and the LED backlight are visible in Figure 3.1.

Table 3.3: Technical specifications of the flow visualization equipment

High speed camera	
Model	Fastcam SA1.1
Max. resolution	1024 x 1024 pixels (up to 5'400 fps)
Max. frame rate	675'000 fps
Triggering	Selectable positive or negative TTL
LED backlight	
Model	PHLOX LEDW-BL-550X400-MSLLUB-Q-1R-24V
Dimension	550 x 400 mm
Uniformity	90% (± 10%)
Luminance	7'000 CD/m^2

Given the conical shape of the draft tube cone, water filled compartments with a flat surface are installed perpendicularly to the camera axis. The presence of the same refractive index on both sides of the curved surface minimizes the optical distortion effects. The setup for the vortex rope visualization may be imagined from Figure 3.4, since the same rectangular window is used for the PIV measurements and the camera position is identical. The setup for the blade cavitation observation with a window along an inclined axis is shown in Figure 3.7.
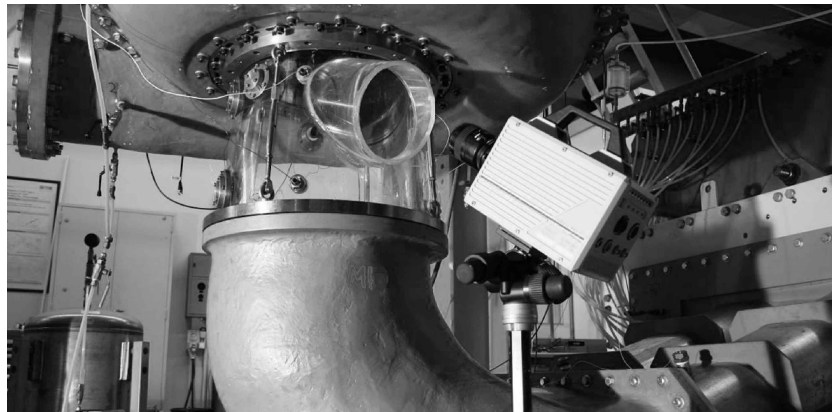
Figure 3.7: Setup for the visualization of the blade cavitation on the reduced scale model.

3.3 Signal processing methodology

3.3.1 Estimation of the vortex rope volume

Edge detection

If the estimation of the vortex rope volume is based on its local radius, it is necessary to detect the edges of the cavity. The same goes for the estimation of the local discharge surface around the vortex rope. The choice of the appropriate method depends on the measuring equipment and on the lighting conditions, which should produce a good contrast between the liquid and gaseous phase in the flow. When the draft tube cone is illuminated with conventional spotlights, the application of a Laplacian of Gaussian (LoG) type filter is found to yield the most satisfying results, as described in [41]. The corresponding procedure is illustrated in Figure 3.8. In the original photos from a high speed camera (top row) it is observed that the vortex rope is often hardly distinguishable from its surroundings, especially during the presence of a large amount of bubbles in the flow. Furthermore, the reflections of the light on the surface of the cavity as well as on the Plexiglas cone are conflicting. A mask is defined based on a ROI around the vortex rope. The filtered version of this ROI is shown in the bottom row of Figure 3.8 and the local radius of the vortex rope can hence be estimated by locating the first and the last black pixels on a given row.

A) B) C) D)
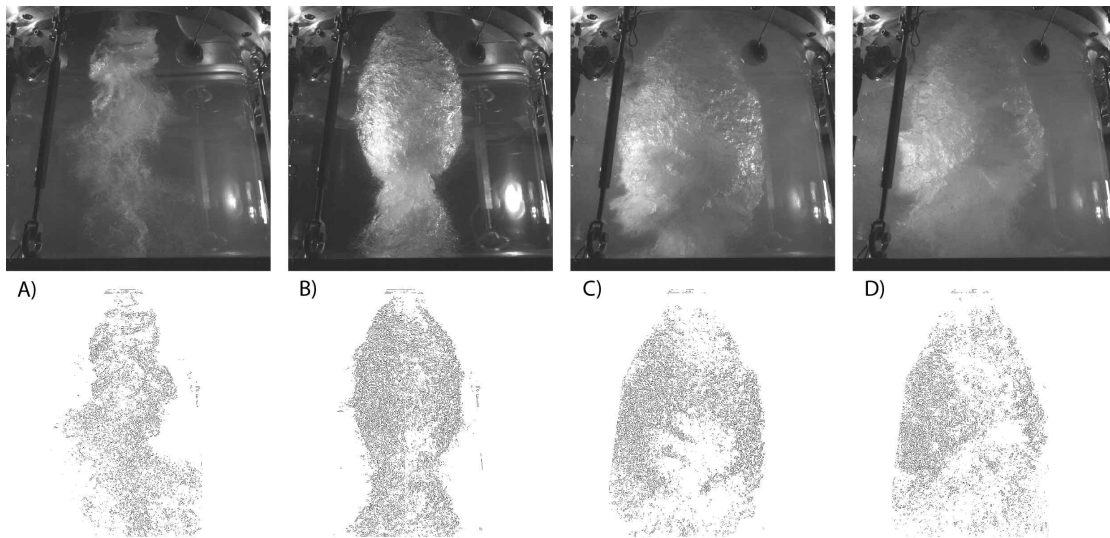
Figure 3.8: High-speed visualization of the vortex rope (top row) and result of LoG filtering with inverted black and white pixels (bottom row) from [41].

A much better outcome is obtained with the LED backlight panel described in Section 3.2.3. This uniform light source produces a sharp contrast between the gaseous and the liquid phase of the flow, as illustrated for instance in Figure 1.4. The vortex rope edge can therefore simply be found by identifying the black and white pixels in a binary picture matrix obtained with an ideal threshold value according to [48]. No filtering or additional image processing is usually

required. It is however observed that a manual adjustment of the threshold value may be beneficial in order to isolate the vortex rope from its surrounding flow in the presence of an increased amount of bubbles.

Finally, the vortex rope edge may also be determined based on PIV measurements, as described in Section 3.3.2 for the determination of the local discharge area around the cavity.

Calculation of the vortex rope volume

Similar to the method described in Section 2.3.3, a ROI covering the region of the draft tube cone is defined. With the coordinates of the corresponding polygon's vertices, a binary mask is then constructed and applied to the images that have been transformed into black and white beforehand. This is shown in Figure 3.9.

(a) Raw image with ROI   (b) Binary mask based on ROI
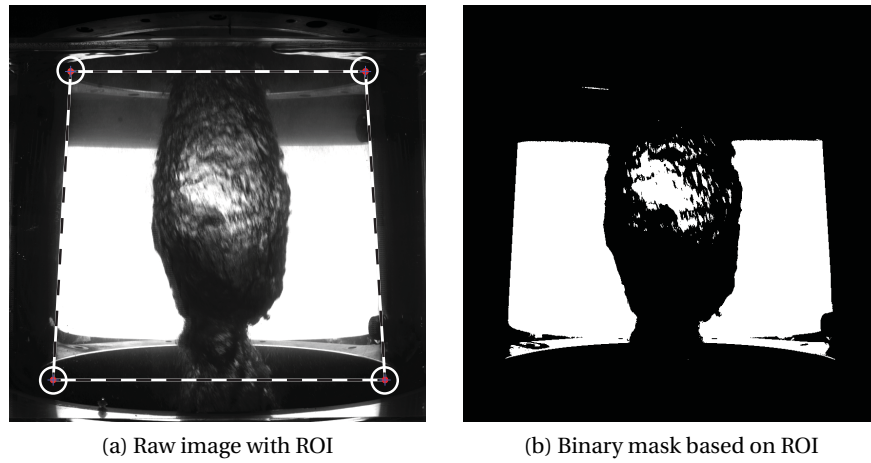
Figure 3.9: Image processing of high speed visualization material at OP#2.

The visible fraction of the vortex rope volume may then be estimated with two different methods. The first one shall be referred to as the differential method, consisting in the subtraction of two consecutive image frames and using the difference in pixels to estimate the volume change in between. This method is already described in detail in Section 2.3.3, where it is applied to a simplified test case with a micro-turbine.

Another possibility to estimate the volume of the vortex rope is to determine its local radius and to sum up its presumably circular cross-sections. The volume delimited by a surface of revolution around a central symmetry axis is defined as

$$V = \int_0^{2\pi} \int_0^{R_{\bar{x}}} \int_{z_1}^{z_2} r \, \mathrm{d}\theta \mathrm{d}r \mathrm{d}z \ = 2\pi \int_{z_1}^{z_2} \frac{1}{2} R_{\bar{x}}(z)^2 \, \mathrm{d}z \approx \pi \sum_{i=1}^{N} \left(R_{\bar{x},i}^2 \cdot \Delta z_i \right), \tag{3.1}$$

where $R_{\bar{x}}$ is the local vortex rope radius at an arbitrary streamwise position $\bar{x}$. The altitudes z_1 and z_2 represent the limits of the visible portion of the vortex rope in the draft tube cone and N is the number of pixel rows in a given picture frame between z_1 and z_2, each row covering a vertical distance of Δz_i.

The estimation of the vortex rope volume based on the above described visualization techniques has a few weaknesses. Among them are the general underestimation of the cavity's volume. Figure 3.9 reveals that only a fraction of the vortex rope can be taken into account for the calculation of its volume. Indeed, the regions which are not contrasted by the LED backlight source, below the Plexiglas cone and from the runner hub to the lower spiral case end, are hardly visible in Figure 3.9a and fall on the dark side of the threshold in the binary version displayed in Figure 3.9b. A significant, not quantifiable error is therefore introduced, since a non-negligible portion of the cavity is periodically ignored. As is can be seen in Figure 3.10, the vortex rope continues well beyond the draft tube cone and even the elbow. Figure 3.10a shows a view from above into the draft tube, through the Plexiglas cone. The upper edge of the photo roughly corresponds to the downstream end of the cone. Its lower half displays the pier nose where the diffuser separates into two branches. Figure 3.10b shows the tip of the vortex rope through one of the two circular side windows in the elbow (visible for example in Figure 3.3).
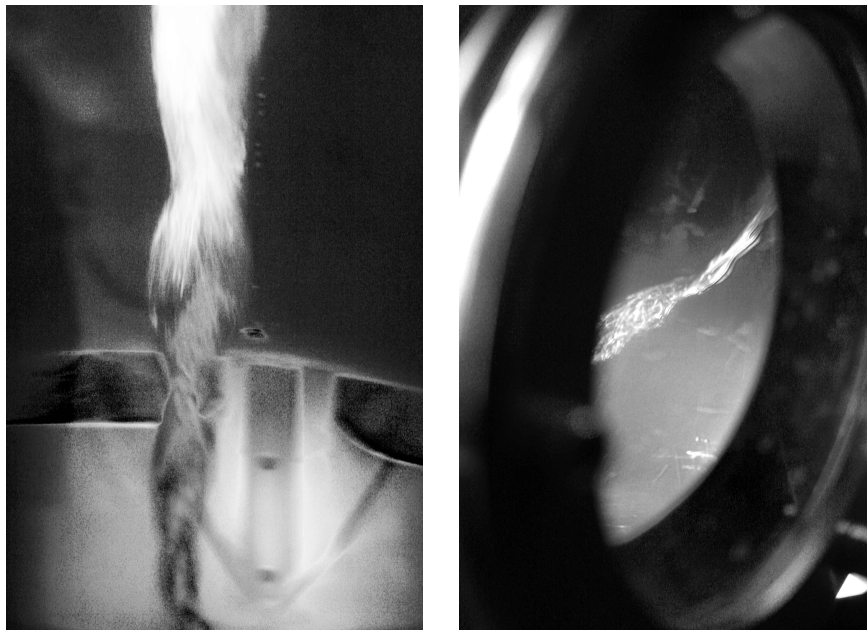
(a) View from above into the draft tube   (b) Rope tip through side window

Figure 3.10: Vortex rope extending into the draft tube elbow.

Finally, both methods regularly fail during the cloudy phases with a significant amount of bubbles present in the surrounding flow. In concrete terms, said bubbles are regularly but arbitrarily detected to be part of the gaseous phase in the conversion from the raw to the

binary form of a picture frame. This depends mainly on the threshold value, which is static and not adapted to the different phases of the flow oscillation. The integral method is particularly susceptible to this, since the local vortex rope radius is calculated by detecting the first and the last white pixel in a given picture row. Two detected one-pixel bubbles might therefore yield a too large radius or even suggest the presence of a rope where there is none.

3.3.2 Post-processing of the PIV data

The raw images from the PIV equipment are used to obtain two-dimensional velocity fields in the draft tube by applying an appropriate mathematical correlation method and one or several flow-specific validation techniques. In addition to that, the camera output may also be processed in order to find the vortex rope edges and hence the local discharge surfaces. Six examples of the raw images from the PIV camera are shown in Figure 3.11, where the white dots represent the fluorescent particles illuminated by the light sheet from the pulsed Laser. The dash-dotted line marks the cone center and the positions A, B and C correspond to the streamwise locations where the discharge is calculated later on, at $0.55 \times D_{\bar{1}}$, $0.70 \times D_{\bar{1}}$ and $0.84 \times D_{\bar{1}}$ below the runner exit, respectively.
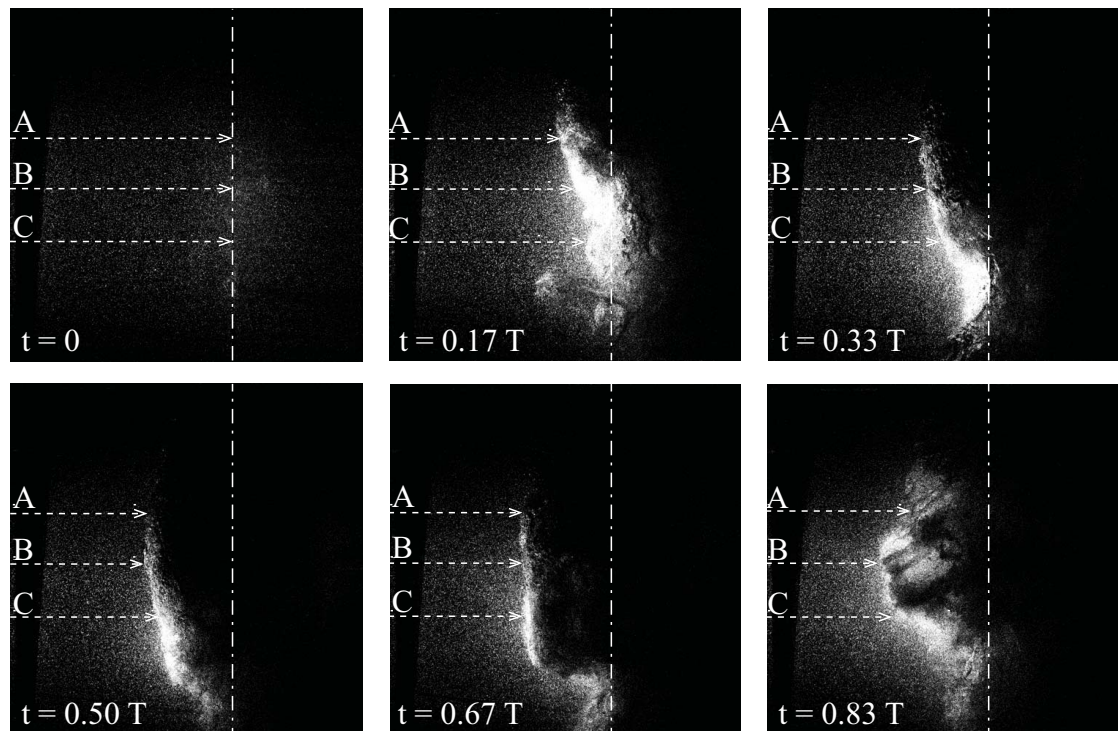
Figure 3.11: Raw images from the PIV camera during six instants uniformly distributed over one period of the vortex rope oscillation at OP#2.

Calculation of the velocity fields

Cross-correlations in interrogation windows of 32 pixels with a 50% overlap are calculated from the raw image pairs. At a resolution of 2048×2048 pixels, this produces 127×127 velocity vectors. The obtained cross-correlation maps need however further validation. As shown in earlier sections, the concentration of bubbles in the draft tube flow varies significantly over one period of the vortex rope oscillation. When reconstructing the evolution of the velocity field with pressure synchronized measurement points, it is observed that the number of erroneous vectors is significant for an increased presence of bubbles prior to the collapse of the vortex rope. These inaccurate vectors can be eliminated and replaced by post-processing in two steps. First, a simple range validation is performed, where all the vectors with an amplitude exceeding 10 m s^{-1} are discarded. This is followed by a moving average validation, in which each vector of the cross-correlation map is compared to the average of a surrounding 3×3 window and substituted by interpolation if the deviation is larger than 10%. The validation criteria are based on experience and observation. Once these methods are applied to all the cross-correlation maps at a given measurement point, the mean vector field can be calculated, which is finally used to obtain the velocity profiles.

The entire validation process is illustrated in Figure 3.12. The corresponding measurement point is taken during the decreasing phase of the vortex rope at $t = 0.63\ T$, characterized by the presence of a significant amount of bubbles in the surrounding flow. The top figure shows the raw velocity field resulting from one out of the forty measurements at the given instant of the instability, where all the vectors with a modulus larger then 10 m s^{-1} detected in the range validation are drawn with dashed lines. The middle graph shows the result of the moving range validation on that same raw velocity field. The bottom figure finally shows the mean velocity field obtained by calculating the average over all the forty validated cross-correlation maps at this measurement point. Even if the contour of a vortex rope seems still visible in the averaged velocity field, measurements in the vicinity of the water-vapor interface feature a larger uncertainty due to the reflection of the light sheet on the surface of the vortex rope, as shown by [40] for a large collapsing bubble.

Vortex rope edge detection

None of the techniques described in 3.3.1 could be employed in case of the approximation of the discharge surface in [43], since there was no space for an additional camera or the LED panel in the experimental setup. Therefore, the picture material obtained with the PIV camera was used. An algorithm is developed detecting the edge of the vortex rope, based on the identification of the overexposed area at the surface of the well developed vortex rope. First, the images are transformed into a binary (black and white) form using an ideal threshold value according to [48]. Then, on a given row of the picture matrix, the white pixels are counted in horizontal windows, starting form the left and moving to the right side with a 50% overlap. The window size, typically between 1×4 pixel and 1×32 pixel, is chosen based on the intensity of the reflection of the light sheet at the vortex rope surface, which critically depends on the
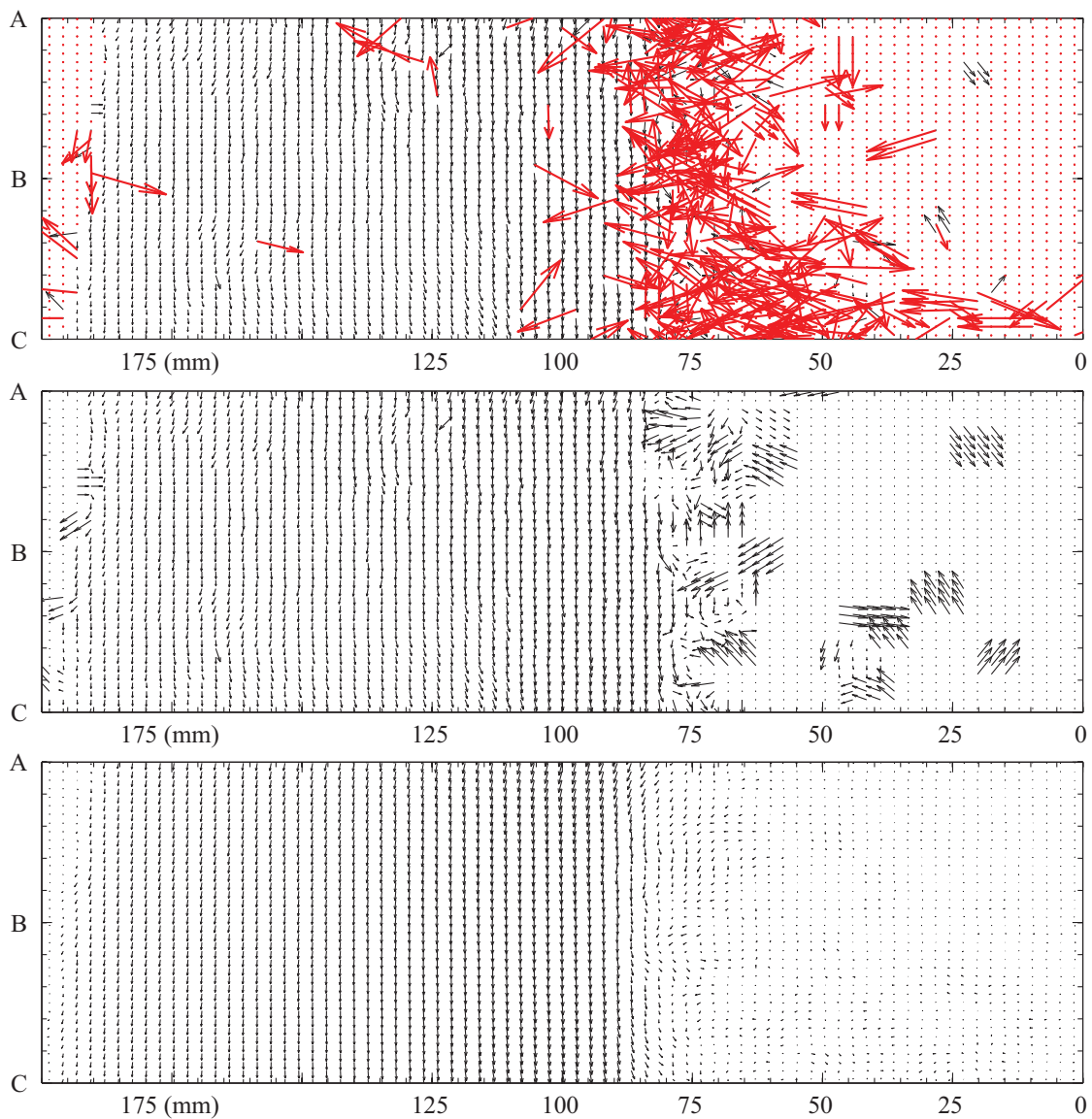
Figure 3.12: Top: Raw velocity field with invalid vectors after the range validation (dashed thick lines). Middle: Velocity field after moving average validation. Bottom: Mean velocity field based on 40 validated velocity fields. The origin of the X-axis is located on the cone centerline.

power of the pulsed Laser. These parameters are determined empirically on a trial and error basis. The described steps are repeated until the first window containing exclusively white pixels is found, where the location of the vortex rope edge is set at the given window's left end. The results of this algorithm are shown in Section 3.7.1. It is clear that the reliability of this algorithm depends on the vortex rope shape, producing the best results when the cavity is fully developed and overestimating its local radius in the phase of the collapse and the following reformation.

55

3.3.3 Flow rate calculation

The calculation of the instantaneous flow rate requires the knowledge of the axial velocity profile at a given streamwise location and the relevant discharge surface. The former is directly obtained by the PIV measurements, whereas the latter is estimated using the algorithm described in Section 3.3.1 or Section 3.3.2. Finally, the discharge Q is written as

$$Q = \int\limits_{R_{edge}}^{R_{wall}} \int\limits_{0}^{2\pi} Cm \cdot r \,\mathrm{d}r\mathrm{d}\theta = 2\pi \int\limits_{R_{edge}}^{R_{wall}} Cm \cdot r \,\mathrm{d}r, \tag{3.2}$$

where R_{edge} and R_{wall} refer to the local radius of the vortex rope and the inner draft tube cone wall radius, respectively. The integral in eq. (3.2) is calculated using the Simpson's rule [57], assuming an axisymmetric rope shape.

3.3.4 Mean phase averaging

A strong periodicity is observed in the signals of the measured quantities, most notably in the wall pressure fluctuations. However, small variations from one cycle to another are natural and the definition of a mean value with respect to one period of the oscillation seems meaningful. A notion of the instant phase is gained by constructing an analytic signal $z(t)$, with the ultimate purpose of isolating the individual periods of a given signal. The analytic signal is expressed as

$$z(t) = x(t) + i \cdot \mathscr{H}[x(t)], \tag{3.3}$$

where the real part consists of the actual measurement data $x(t)$ and the complex part is represented by its Hilbert transform [6]. The variable i denotes the imaginary unit defined as $\sqrt{i} = -1$. The argument $\arg(z(t))$ is interpreted as the phase of $x(t)$. In current commercial softwares, the Hilbert transform is often calculated using an FFT algorithm [39]. Other reference signals may of course be used to split a signal into its different cycles. At partial load conditions ($Q < Q_{\mathrm{BEP}}$) for instance, the vortex rope precession is well adapted, as demonstrated by [5]. Still in the context of hydraulic machines, the runner revolutions are often another suitable choice.

In order to illustrate the method, the mean phase average of the signal shown in Figure 1.5c is calculated. In a first step, the analytic signal and its argument are established. The latter is shown together with the raw wall pressure factor signal in Figure 3.13a for a time window of 4 s. This allows assigning a phase angle value to each pressure data point. One period $[0, 2\pi]$ is then divided into a suitable number of windows and the mean value of all the pressure data

points in a given window is calculated. This is illustrated in Figure 3.13b for an angular window size of 3 deg., where the vertical error bars represent the standard deviation. The use of a low pass filter is often necessary in order to reject phase changes due to small scale fluctuations.

(a) Pressure factor c_p (solid line) and phase angle θ (dashed line)

(b) Mean phase averaged pressure factor c_p with standard deviation
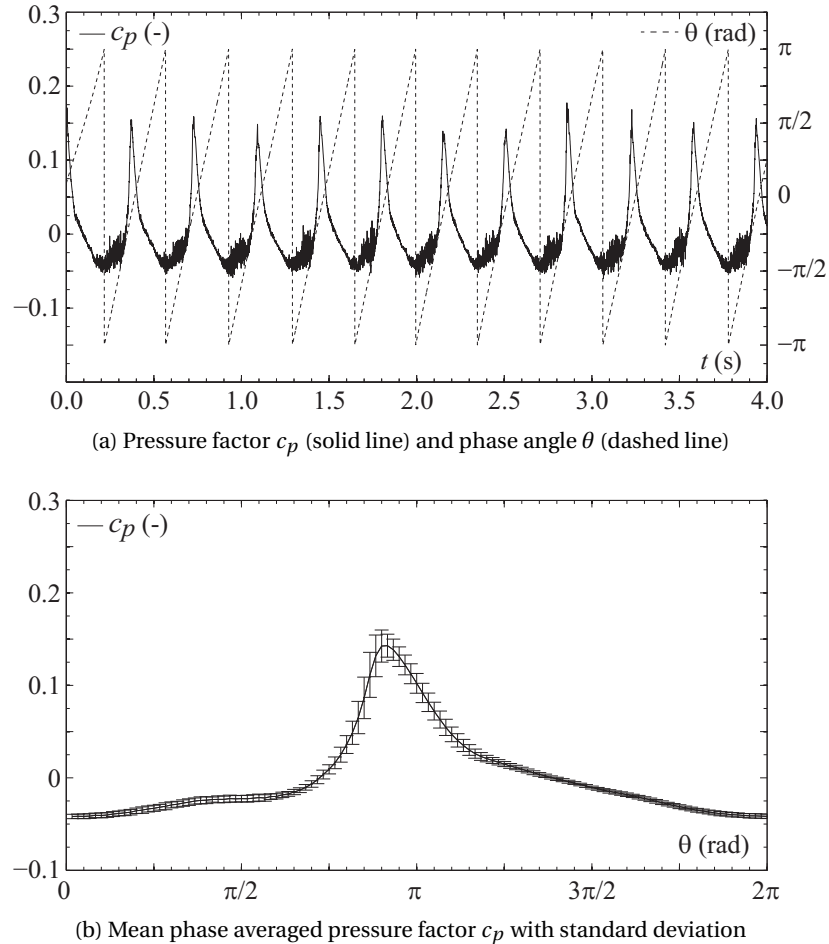
Figure 3.13: Mean phase averaging of a wall pressure signal in the draft tube cone measured $0.39 \times D_{\bar{I}}$ downstream the runner exit. A total number of 137 pressure oscillation cycles were taken into account for the calculation.

3.3.5 Spectral analysis of randomly sampled data

The statistical analysis of randomly sampled data, for instance from LDV measurements, is to be performed with care so as to avoid the loss of relevant information and to control the resulting errors in the frequency domain [24]. Several options exist to calculate the Hilbert transform of the measured velocity components. For instance, the data can be transformed into a continuous signal, enabling the use of efficient standard tools such as the Fast Fourier Transform (FFT). The available reconstruction methods include the *sample and hold* technique and a piecewise interpolation of the data. The sample and hold process consists of holding a sampled velocity value until the arrival of the next particle in the control volume. It

acts as a low pass filter due to the loss of information during the hold periods and implicates the presence of a white "step noise" created by the random steps [1]. These effects may be mitigated by a polygonal interpolation, for instance, as shown in [49]. Alternatively, the LDV data may be processed directly, taking into account a variable time step. The statistical properties of the spectral estimates of randomly sampled data using direct transform methods are described in [25].

For the direct approach, the algorithm proposed by [39] is implemented for a variable time step. The Discrete-Time Fourier Transform (DTFT) of the velocity data $c(t)$ is calculated according to [6] for each frequency component f_k. This is done by using

$$C(k) = \sum_{i=1}^{N-1} (c(t_i) \cdot D(t_i)) \cdot \Delta t_i \cdot e^{-i \cdot 2\pi f_k \cdot t_i} \, , \tag{3.4}$$

where N represents the total number of samples, Δt_i are the individual time lags between the samples, f_k the frequency components, t_i the arrival times of the particles and $D(t)$ a suitable data window. Once the DTFT calculated, the negative half of the spectrum is discarded by defining the one-sided signal transform

$$Z(k) = \begin{cases} C(0), & \text{for k=0} \\ 2 \cdot C(k), & \text{for } 1 \le k \le \frac{N}{2} - 1 \\ 0, & \text{for } \frac{N}{2} + 1 \le k \le N - 1 \end{cases} \tag{3.5}$$

Finally, the analytic signal is obtained by calculating the inverse DTFT of $Z(k)$, hence

$$\tilde{c}(n) = \sum_{k=1}^{N-1} Z(k) \cdot \Delta f_k \cdot e^{i \cdot 2\pi f_k \cdot t_n} \, . \tag{3.6}$$

The velocity data acquired during a period T at a given measuring location may be split into a suitable number M of windows in order to minimize the variability of the spectral estimation as shown in [25]. Accordingly, each value obtained by eq. (3.4) represents a mean value over the total number of windows, which is

$$C(k) = \frac{1}{M} \sum_{j=1}^{M} C_j(k) \, . \tag{3.7}$$

Alternatively, the raw LDV data can be interpolated with methods available in commercial software, such as piecewise cubic hermite polynomial functions [23]. The result is a continuous reconstruction of the velocity signal and the corresponding analytic signal is then easily obtained by using standard calculation tools, such as for the pressure signal described in Section 3.3.4. Without providing prove, the obtained spectra for the direct DTFT approach and the interpolated data are very similar. The computational time is however significantly lower for the interpolated data.

3.4 Variation of the vortex rope volume

Figure 3.14 shows the approximated dimensionless vortex rope volumes for two different speed factors at OP#2 and OP#5, obtained by using the differential and integral methods presented in Section 3.3.1. It is first noticed that the results from the differential analysis and the integral calculation show a good overall agreement. Furthermore, the values of the void fractions are realistic by comparing with the visualizations in Appendix A (Figure A.3 and Figure A.4). The vortex rope at the nominal speed factor of $n_{ED} = 0.288$ is fairly slim compared two the one at a lower value of $n_{ED} = 0.273$.

(a) $n_{ED} = 0.273$, OP#2 (b) $n_{ED} = 0.288$, OP#5
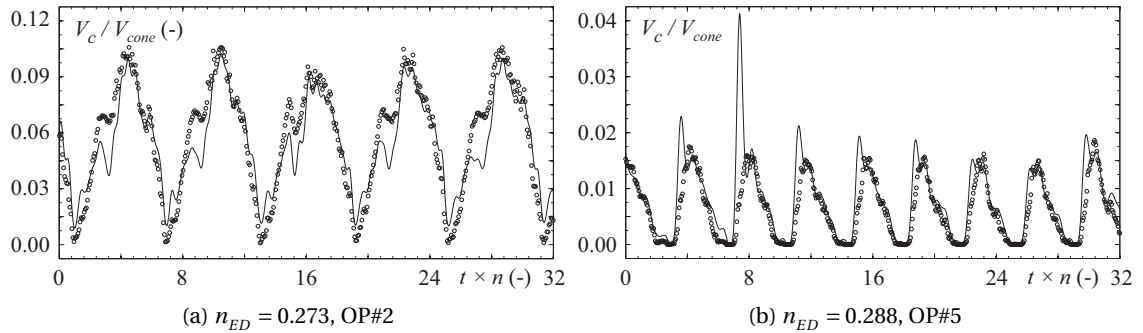
Figure 3.14: Dimensionless V_c as a fct. of the number of runner revolutions at OP#2 and OP#5, obtained from the differential (solid lines) and integral (∘-markers) method.

The problem of the missing portion of the vortex rope is common to both of the presented methods. While the differential method seems to capture irregular rope shapes around its collapse and certain local fluctuations more accurately, it suffers from the error introduced by the reflection of the light on its surface. Especially around the maximum volume. As shown in Figure 3.9b, a considerable part of the cavity's surface is overexposed and transformed into white pixels during the thresholding. The integral method, based on the estimation of the local vortex rope radius, on the other hand, has the advantage of being unbiased by said light reflections. It is however considerably less reliable for the cloudy phases around the cavity's collapse, where no clear edges exist. During these instants, single bubbles in the surrounding flow are often detected and mistaken for the rope edge, introducing an error in the volume calculation. At OP#2 this is more pronounced, since the bubbles in the surrounding flow are larger and appear darker in the pictures than at OP#5.

Figure 3.15 shows the dimensionless vortex rope volume from the differential method together with the wall pressure factor at Section 1 (C1N). It is reminded that V_c only represents the visible, contrasted portion of the vortex rope. The results are therefore mainly of qualitative value. A few interesting insights may however be gained from the presented data. The evolution of the vortex rope volume at the two operating points displays a different behavior with respect to the pressure oscillation cycle. For OP#2, the maximum volume roughly corresponds to the minimum wall pressure and vice-versa. This is not true for OP#5, where the volume is almost synchronized with the pressure, featuring a significantly steeper growth. A common thing between the two different operating conditions is that the growth of the vortex rope is initiated at the end of the highly fluctuating part between two peaks of the pressure signal. A simultaneous viewing of the high speed videos reveals that this instant corresponds to the moments where the bubbles in the surrounding flow disappear and the pictures "clear up" again. Furthermore, both volume curves also display a local "ripple" when said bubbles appear in the flow, at the beginning of the fluctuating pressure phase. If these bubbles have their origin in a periodically appearing and subsequent imploding cavitation on the runner blades, the dynamics of the vortex rope oscillation might be governed by how this blade cavitation modifies the swirl at the runner exit. This shall be further discussed in Chapter 4.

3.5 Velocity field in cavitation free conditions

The results presented hereafter are obtained by LDV in 2-D, non-coincidence mode and include the axial and tangential velocity profiles at the BEP and several operating points at high load. The pressure in the downstream reservoir is set to atmosphere in order to minimize the formation of cavitation in the draft tube flow. The corresponding σ values in Appendix B.1 are therefore replaced by the acronym *atm*. Different flow patterns are discussed resulting from a variation of the flow rate and the swirl in the draft tube.

The wall pressure signals for the BEP and two typical overload operating points at the nominal speed factor of $n_{ED} = 0.288$ and a lower value of $n_{ED} = 0.273$ are shown in Figure 3.16 in the time and frequency domain. For the BEP and OP#3, the runner frequency n is the dominant peak in the frequency domain. At the BEP, a second distinct peak at $0.74 \times n$ is present, whereas a low frequency contribution is observed at $0.1 \times n$ at OP#3. For the lower n_{ED} value at OP#4, the runner frequency is still present, but matched in amplitude by various unidentifiable contributions to the spectrum.

Figure 3.17 and Figure 3.18 show the mean axial and tangential velocity profiles on the two LDV measurement sections along the x-axis for the BEP. Figure 3.19 and Figure 3.20 displays the same thing for the overload operating conditions at OP#3. The definition of the axes corresponds to the coordinate system in Figure 3.3a. The z-axis points in the streamwise direction and the runner rotates in a clockwise direction. The *Cm* and *Cu* components are made non-dimensional with the mean discharge speed in the given measurement section and the circumferential runner speed at $R_{\bar{1}}$, respectively.

(a) $n_{ED} = 0.273$, OP#2

(b) $n_{ED} = 0.288$, OP#5
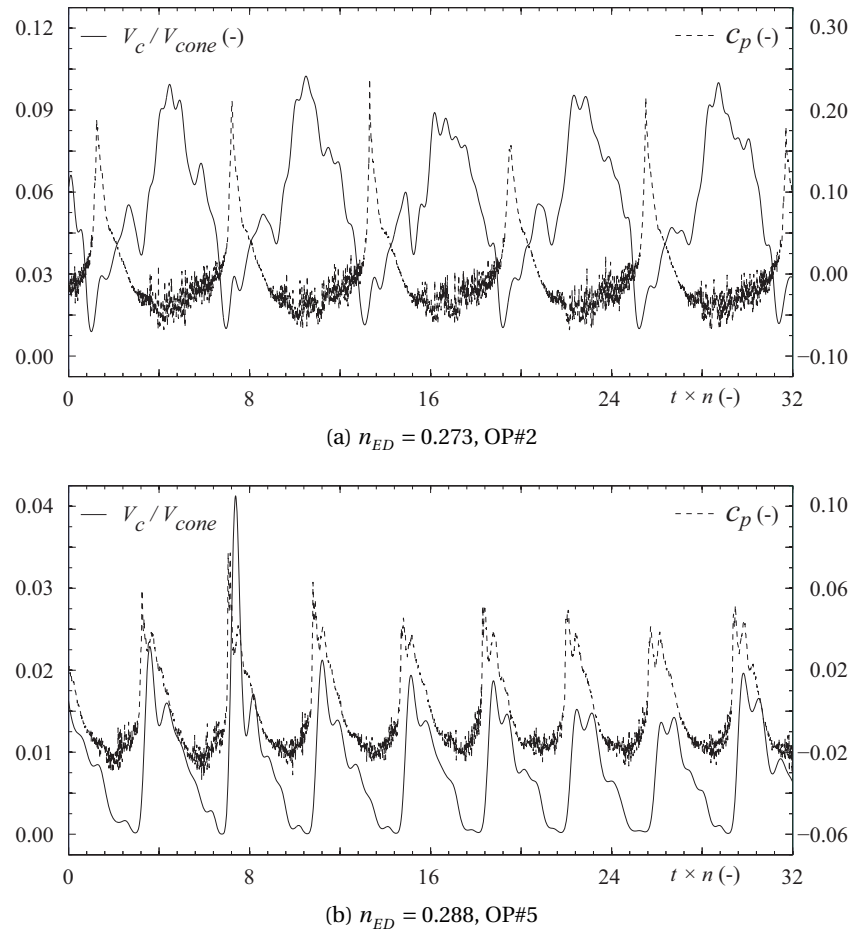
Figure 3.15: Temporal evolution of the vortex rope volume and the pressure coefficient at C1N for different speed factors as a function of the number of runner revolutions.

At the BEP, a significant decrease of the axial velocity component *Cm* is observed in the center of the draft tube cone, the flow direction even being inverted at the upper section in Figure 3.17a. This profile shape is known from similar studies on reduced scale models at partial load around the best efficiency point [58]. The same behavior is described in the theory of swirling jets, when the forces induced by the adverse pressure gradient created by the swirl breakdown further downstream overweigh the forward kinetic forces [26]. The opposite is the case for the *Cm* profiles in the central region at OP#3, which continue to grow and reach their maximum on the cone centerline, as shown in Figure 3.19a and Figure 3.19b.

The tangential velocity profiles in Figure 3.18 and Figure 3.20 are typical of a Lamb-Oseen vortex [37, 47]. The dashed circles around the graphs illustrate the inner cone wall at the corresponding LDV measurement section as seen from above. The fact that the draft tube flow at the BEP has a significant swirling component, and that its direction is reversed between the BEP and OP#3, indicates that the BEP of this particular reduced scale model is situated in the partial load range. This is unusual, since in theory, the flow at the runner outlet is purely axial

(a) BEP

(b) BEP

(c) OP#3, $n_{ED} = 0.288$

(d) OP#3, $n_{ED} = 0.288$

(e) OP#4, $n_{ED} = 0.273$

(f) OP#4, $n_{ED} = 0.273$
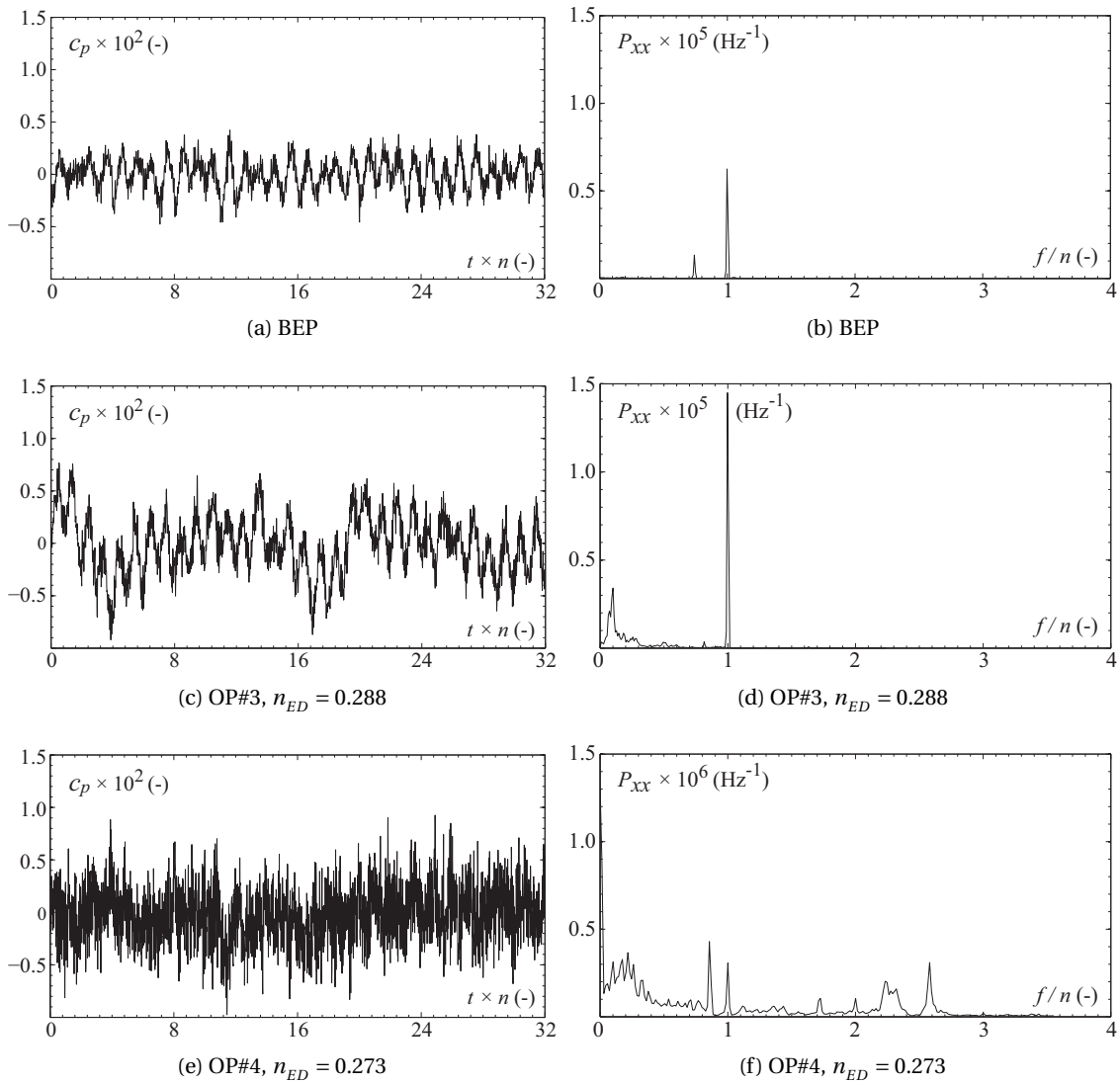
Figure 3.16: Wall pressure factor c_P at C1N (left) plotted against the number of runner revolutions and power spectral density P_{xx} (right) for the BEP, OP#3 and OP#4.

at the BEP. For both cases, the change in the *Cu*-sign past the cone center is well captured. In general, the measurements in proximity of the cone walls at either side are less reliable for both velocity components. A possible reason are optical effects such as parasite reflections of the Laser beams at the Plexiglas interface.
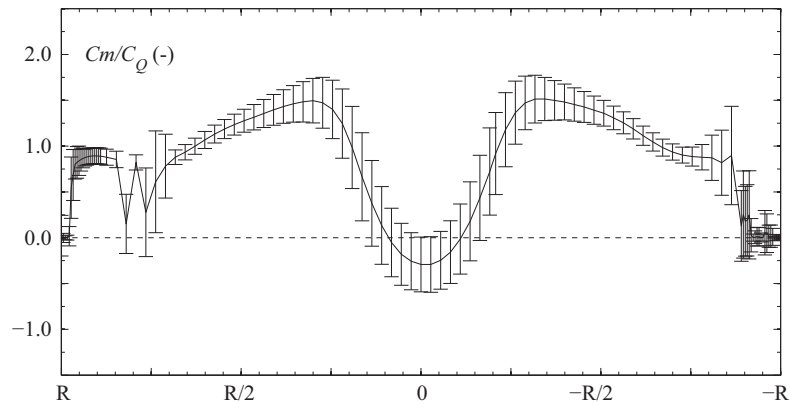
(a) Section 1, $0.39 \times D_{\bar{1}}$ below the runner exit
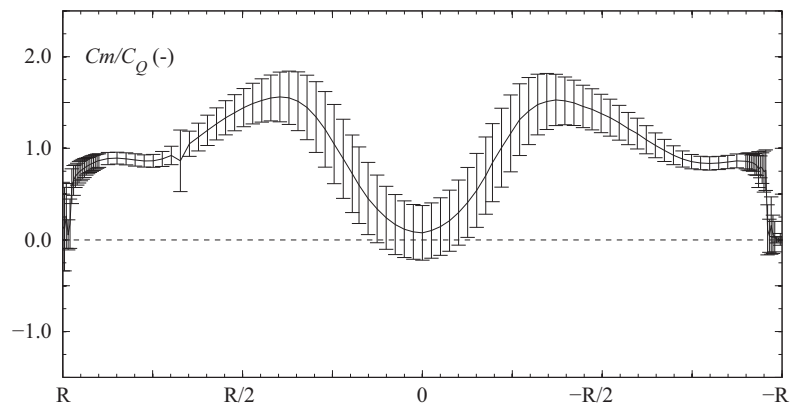
(b) Section 2, $1.0 \times D_{\bar{1}}$ below the runner exit

Figure 3.17: x-axis survey of the mean axial velocity component Cm (solid lines) with standard deviation values (vertical error bars) at the BEP.
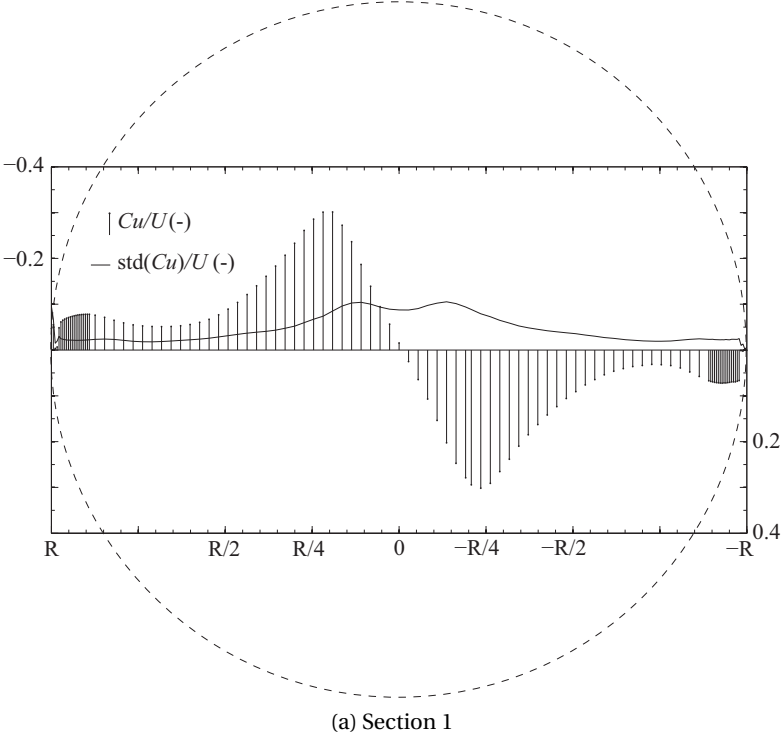
(a) Section 1
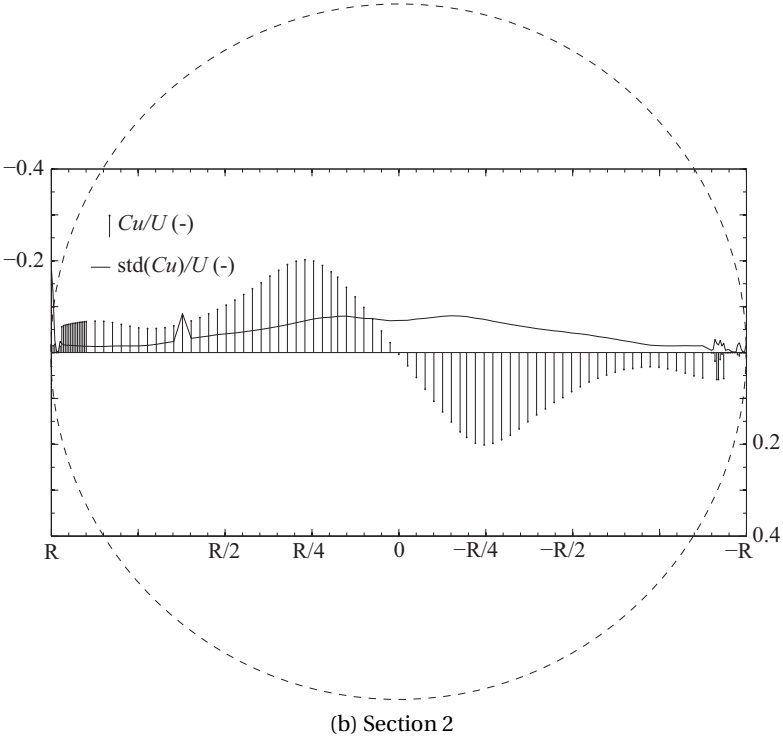
(b) Section 2

Figure 3.18: x-axis survey of the mean tangential velocity component Cu (vertical bars) with standard deviation values (solid lines) at the BEP.

64

(a) Section 1
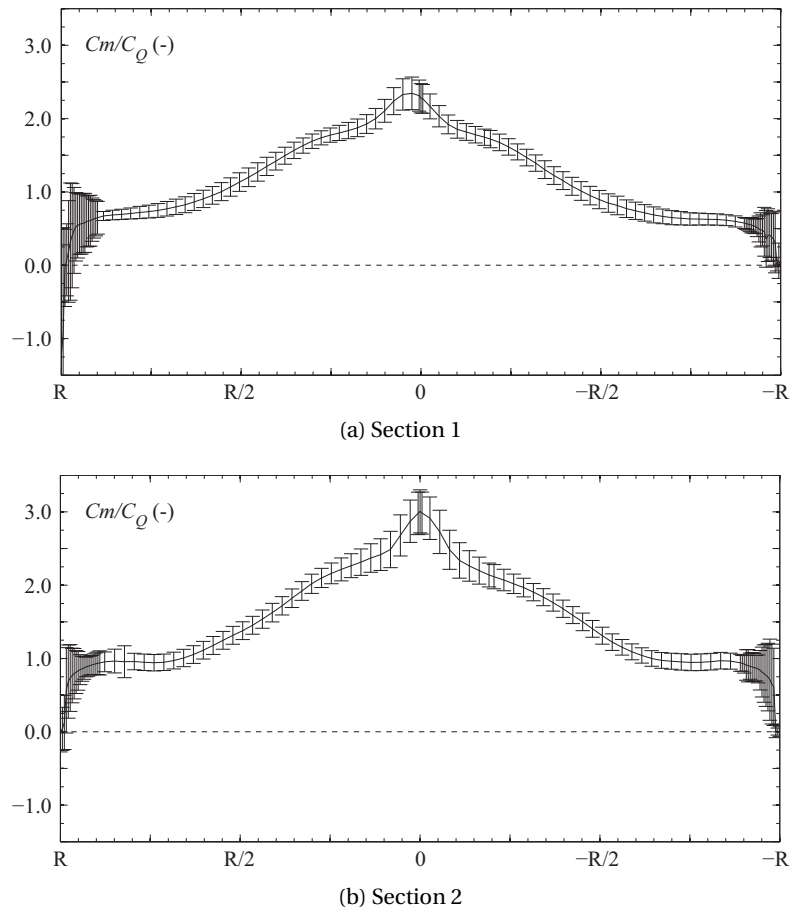
(b) Section 2

Figure 3.19: x-axis survey of the mean axial velocity component Cm (solid lines) with standard deviation values (vertical error bars) at OP#3 ($n_{ED} = 0.288$).
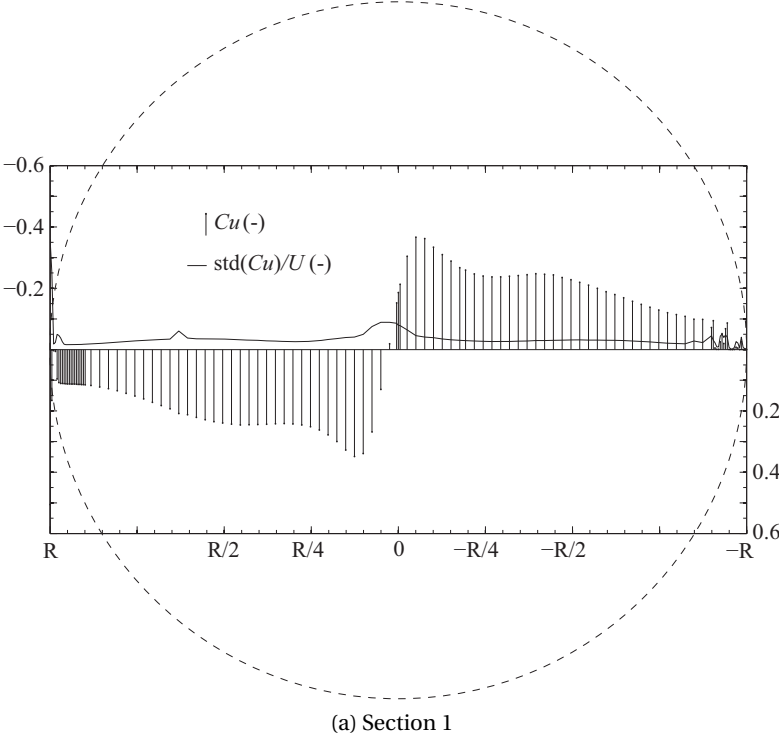
(a) Section 1
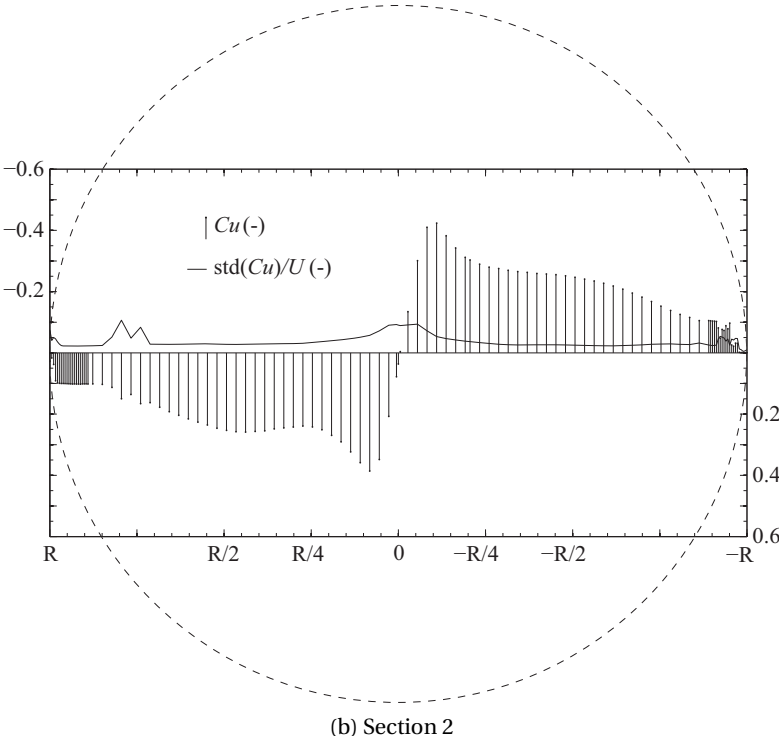
(b) Section 2

Figure 3.20: x-axis survey of the mean tangential velocity component Cu (vertical bars) with standard deviation values (solid lines) at OP#3 ($n_{ED} = 0.288$).

In order to asses the influence of the main operational parameters on the shape of the velocity profiles, additional measurements for several combinations of the speed and discharge factor are performed. One of the outcomes is, for instance, that both behaviors of the axial velocity profiles shown in Figure 3.17 and Figure 3.19, respectively, are observed at similar load conditions. This might suggest the vicinity to a critical swirl number. In order to illustrate this, a systematic variation of Q_{ED} and n_{ED} is performed around OP#4, keeping one of the two parameters as well as the specific energy and the Froude number constant. The speed and discharge factors are modified by changing the runner speed and the guide vane opening, respectively. The evolution of the operating conditions can be followed in Table 3.4 together with the swirl numbers.

Table 3.4: Operating conditions for the LDV measurements without cavitation.

Meas. section	n_{ED} (-)	Q_{ED} (-)	Q (m³ s⁻¹)	N (min⁻¹)	E (J kg⁻¹)	Fr (-)	Q_{ED}/Q_{ED}^* (-)	S (-)
1 (upper)	0.273	0.250	0.3288	505.1	116.46	5.8	1.243	0.351
		0.252	0.3311		116.48		1.252	0.359
		0.254	0.3337		116.55		1.262	0.385
		0.256	0.3365		116.54		1.272	0.410
		0.258	0.3390		116.41		1.283	0.418
		0.260	0.3417		116.31		1.293	0.431
2 (lower)	0.273	0.250	0.3282	505.1	116.20	5.8	1.243	0.387
		0.252	0.3312		116.40		1.253	0.406
		0.255	0.3337		116.52		1.262	0.425
1 (upper)	0.273	0.250	0.3290	505.1	116.46	5.8	1.243	0.351
	0.278			514.7	116.51			0.326
	0.283			524.1	116.50			0.299
	0.288			533.5	116.63			0.268
	0.293			542.5	116.55			0.237
	0.298			551.9	116.75			0.202
	0.303			560.8	116.47			0.171
2 (lower)	0.273	0.250	0.3290	505.2	116.20	5.8	1.243	0.387
	0.288			533.5	116.66			0.310
	0.303			560.8	116.48			0.198

Figure 3.21 shows the mean axial velocity profiles at the upper and lower LDV measurement section for a systematic variation of the speed and discharge factors. The corresponding tangential velocity profiles are included in Figure 3.22. Increasing the discharge factor Q_{ED} and hence the swirl in the flow leaving the runner, the shape of the axial velocity profile in Figure 3.21a and Figure 3.21c switches abruptly from featuring an absolute maximum on the cone centerline to a local minimum in the central region. This agrees with the above mentioned theory of swirling jets. Simultaneously, the radial spread of the central vortex region increases, which is also well displayed in the tangential velocity profiles in Figure 3.22a and Figure 3.22c.

The reaction to an increase of the speed factor n_{ED} is slightly different. Drawing the velocity triangles at the runner outlet reveals that an increase of the circumferential runner speed U at a constant discharge Q implicates a reduction of the tangential velocity component Cu and therefore the swirl. This is evidenced by the Cu-profiles in Figure 3.22b and Figure 3.22d. The axial velocity component has its peak in the central flow region, which is however continuously "flattened" and finally slightly inverted for increasing runner frequencies.

It is mentioned that the approach of the critical swirl number during the Q_{ED}-variation coincides with the appearance of a thin vortex (ø ≈ 10 mm) along the flow center. For $Q_{ED} = 0.254$, this vortex features a breakdown oscillating axially around the measurement section 1, characterized by very large values of standard deviation around the plotted mean value. For larger values than $Q_{ED} = 0.254$, the vortex extends beyond the Plexiglas cone and the LDV samples vary moderately even across the gaseous phase. Furthermore, due to the flow asymmetry introduced by the elbow, the vortex is slightly deflected from the geometrical cone centerline in positive x-direction at the lower measurement section 2. As a consequence, the velocity profile does not pass though the center of the flow with the setup in Figure 3.3b.
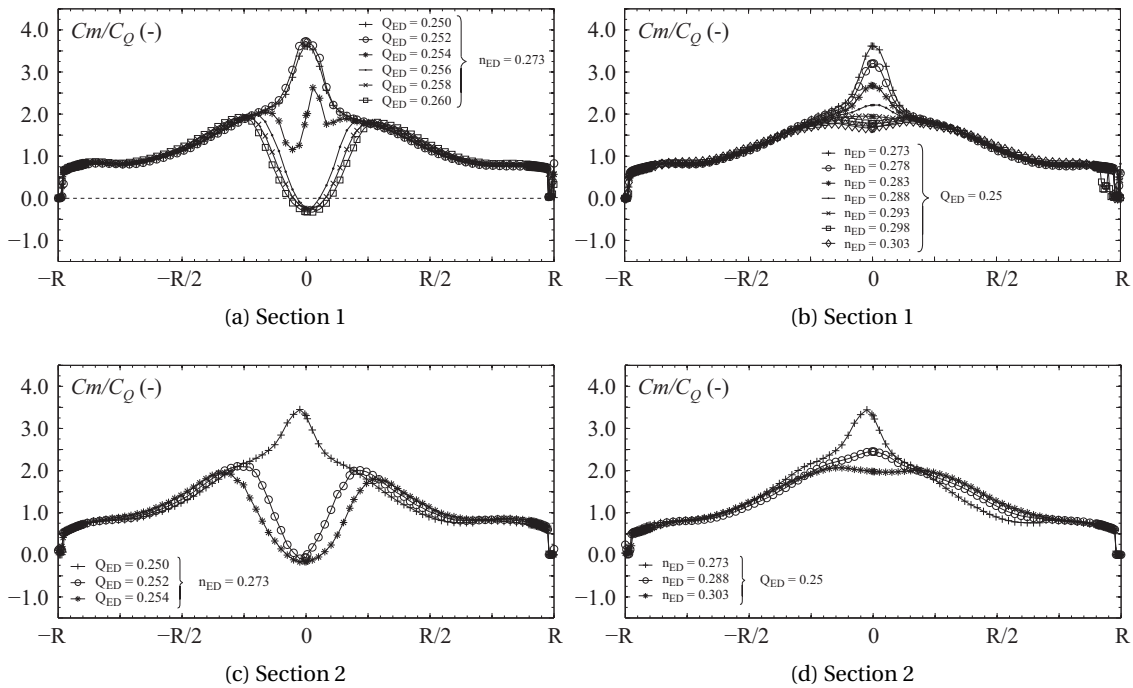
Figure 3.21: Mean axial velocity profiles Cm along the y-axis for a variation of Q_{ED} and n_{ED} at the upper and lower LDV measurement sections.
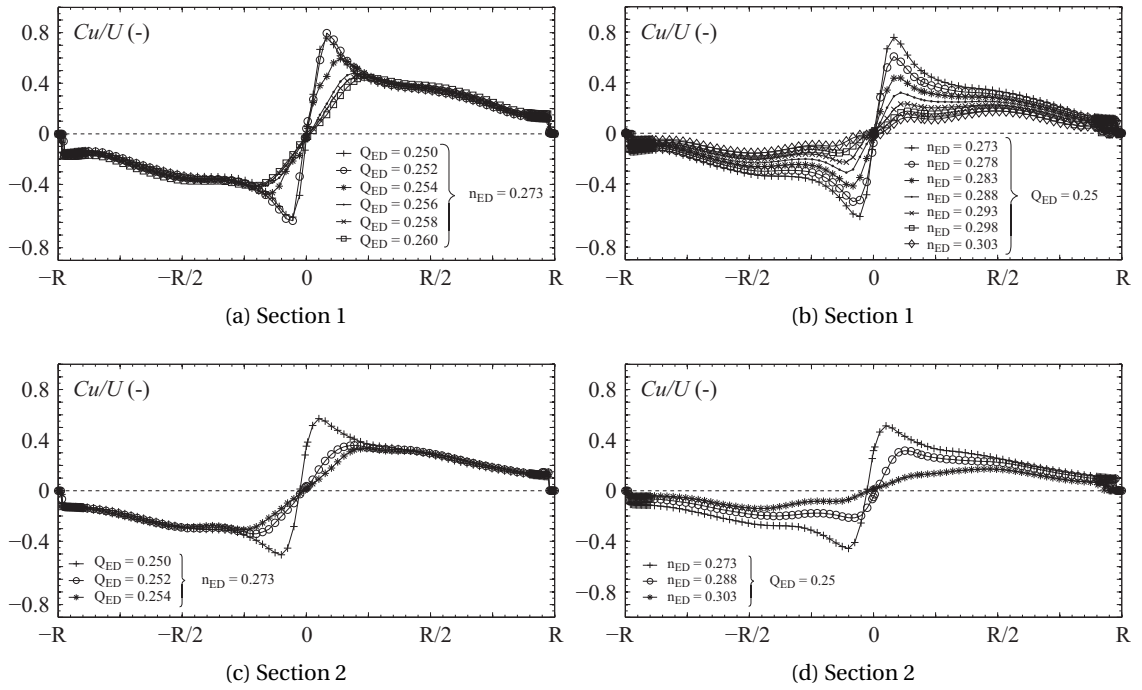
Figure 3.22: Mean tangential velocity profiles Cu along the y-axis for a variation of Q_{ED} and n_{ED} at the upper and lower LDV measurement sections.

3.6 Velocity field in presence of an oscillating vortex rope

3.6.1 Local pressure synchronized velocity variations from LDV

The fluctuating velocity components in presence of an oscillating vortex rope measured by LDV can be averaged with respect to the wall pressure signal. This was shown in [42] by the author for a single radial measurement position. The following development is an extension of this analysis to the entire measurement cross-section at several operating points. To this end, the mean phase averaged pressure signal is calculated with the method presented in Section 3.3.4. The velocity data is then split accordingly into sub-cycles and averaged, making it thusly possible to follow the behavior of the axial and tangential velocity components over a single period of the vortex rope oscillation at a given radial position. This is illustrated presently for three radial locations on the upper and lower horizontal LDV measurement sections. Figure 3.23 shows six equally spaced instants of the vortex rope oscillation at OP#5, where the crosses mark the radial measurement positions at a distance of $0.87 \times R_{\bar{1}}$, $0.47 \times R_{\bar{1}}$ and $0.086 \times R_{\bar{1}}$ from the cone centerline for a) & d), b) & e) and c) & f), respectively.
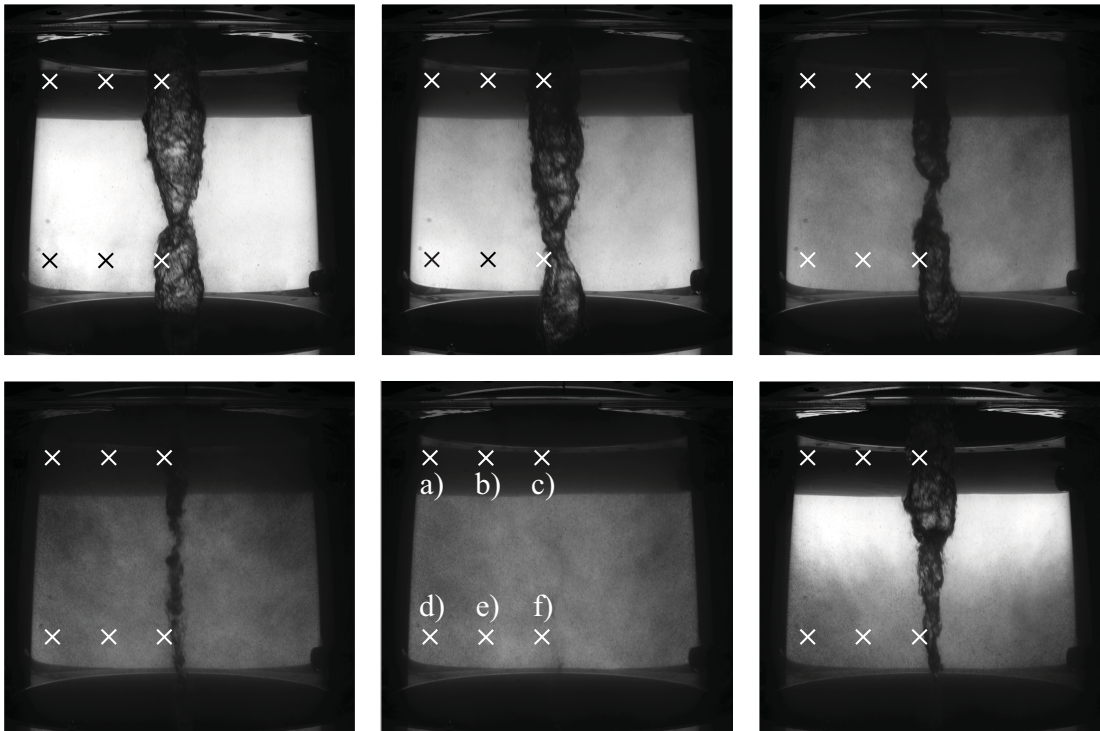
Figure 3.23: High speed visualization of the vortex rope at OP#5 at six equally spaced instants over one period of the pressure oscillation with radial LDV measurement positions (×).

An example for the raw velocity and pressure signals is given in Figure 3.24. The corresponding local evolutions of Cm and Cu for OP#5 are shown in Figure 3.25 and Figure 3.26 for sections 1 and 2, respectively. The operating conditions correspond to the model's nominal speed factor of $n_{ED} = 0.288$ and the nominal Thoma number of $\sigma = 0.11$, at 30% overload.

(a) Pressure factor c_p

(b) Axial velocity Cm

(c) Tangential velocity Cu
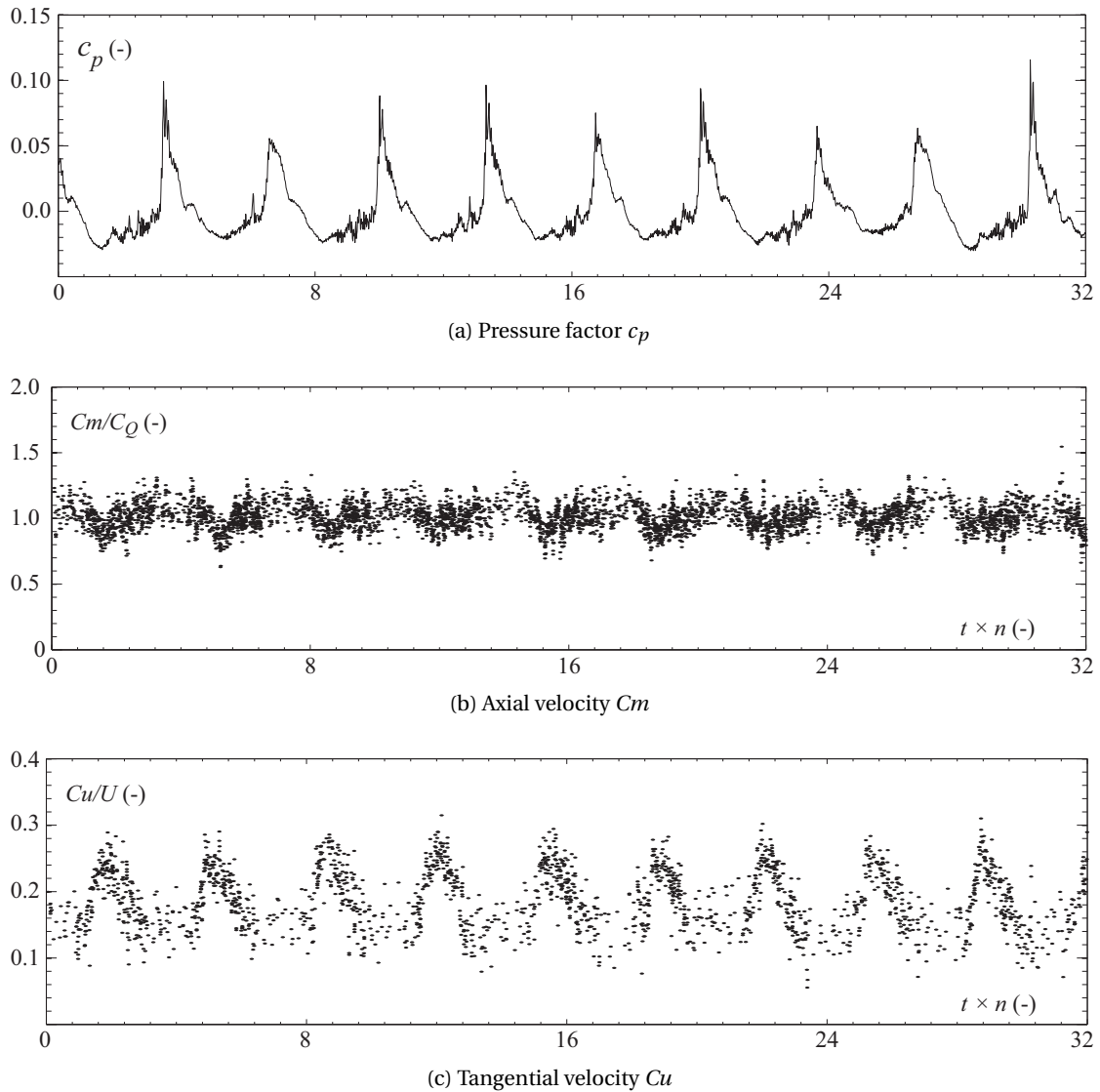
Figure 3.24: Raw, synchronized pressure and velocity data as a function of time at OP#5 ($n_{ED} = 0.288$) for position b) on the LDV measurement section 1.

At the upper LDV measurement section 1, three distinctive forms of the axial velocity profile are observed. While Cm remains practically constant at the radial position a) close to the inner cone wall, its profile displays a moderate local decrease at the pressure fluctuation peak for position b) and a local maximum at position c), which is slightly delayed with respect to the pressure peak. More significant are the variations in the tangential velocity profiles, which reach their maxima shortly after the pressure peaks. At the lower LDV measurement section, a periodic change in the Cm values is hardly noticeable and the corresponding profiles are nearly flat. The behavior of the tangential velocity component Cu is similar to the one on the upper LDV measurement section, where the maximum values occur however a little later in the pressure oscillation cycle. This likely corresponds to the propagation time of the swirl

(a) Axial and tangential velocity, position a) on the upper measurement section

(b) Axial and tangential velocity, position b) on the upper measurement section

(c) Axial and tangential velocity, position c) on the upper measurement section
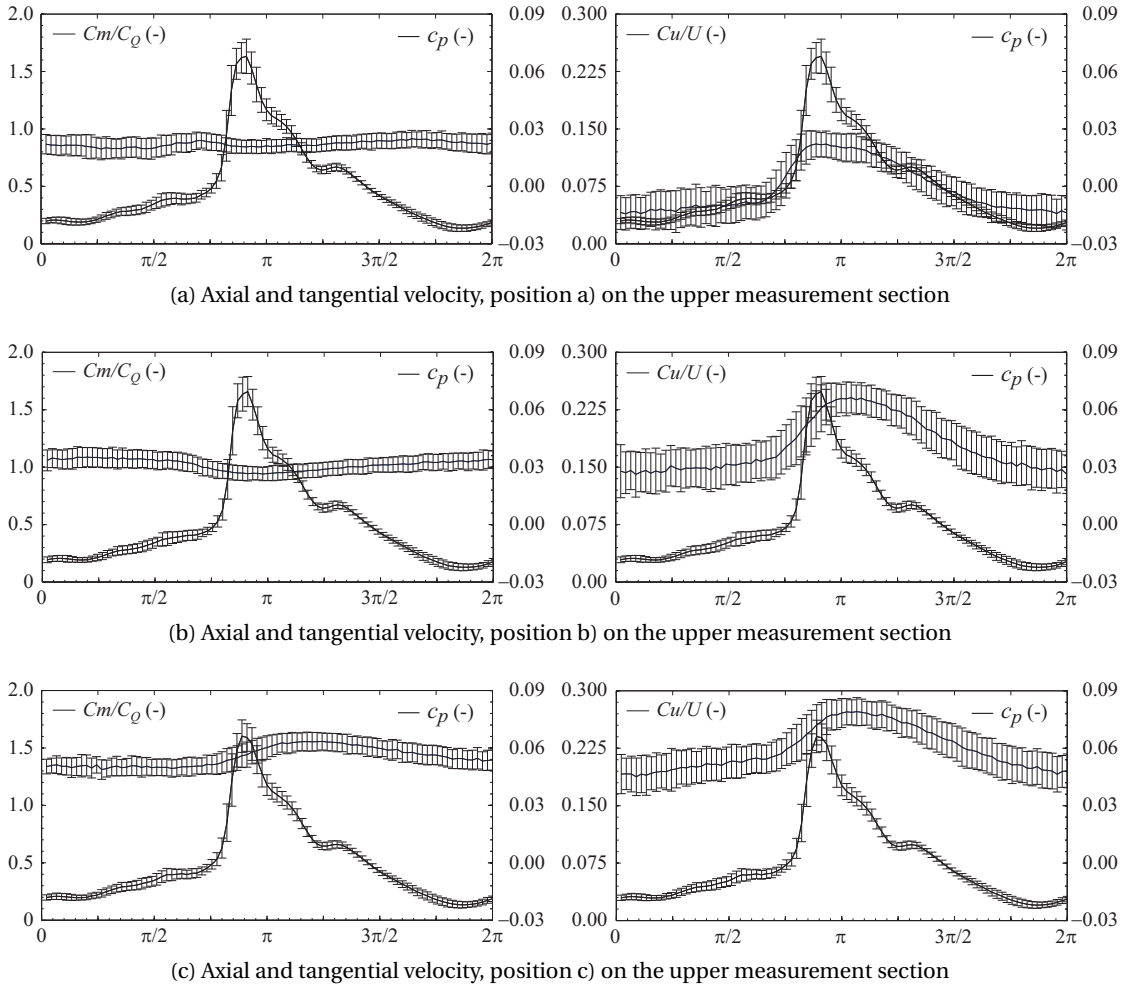
Figure 3.25: Mean phase averaged Cm (left) and Cu (right) at OP#5 ($n_{ED} = 0.288$) together with c_p at C2N (thick line). The x-axis span $[0, 2\pi]$ represents one period of the pressure oscillation.

change from the runner exit, which shall be discussed in a later section. In order to get a more complete picture of how the velocity field changes during one pressure oscillation cycle, all of the measured profiles between the cone wall and the cone centerline are displayed in Figure 3.27 for OP#5.

Figure 3.27a can be divided in two areas of roughly the same radial span. The first one, towards the cone wall, is characterized by a sink, which is formed by the local decrease of the axial velocity component Cm in the corresponding profiles. This was already observed in the left sub-plot of Figure 3.25b. The other half, on the contrary, forms a hill shape, characterized by a local increase in the Cm-profiles. This corresponds to the behavior displayed in the left sub-plot in Figure 3.25c. The tangential velocity profiles in Figure 3.27b all feature a similar shape with a maximum shortly after the mid-period of the pressure oscillation. The same graphs for the lower LDV measurement section are included in Figure 3.28. As mentioned beforehand, the variations in the axial velocity component Cm are less pronounced and the

(a) Axial and tangential velocity, position d) on the lower measurement section

(b) Axial and tangential velocity, position e) on the lower measurement section

(c) Axial and tangential velocity, position f) on the lower measurement section
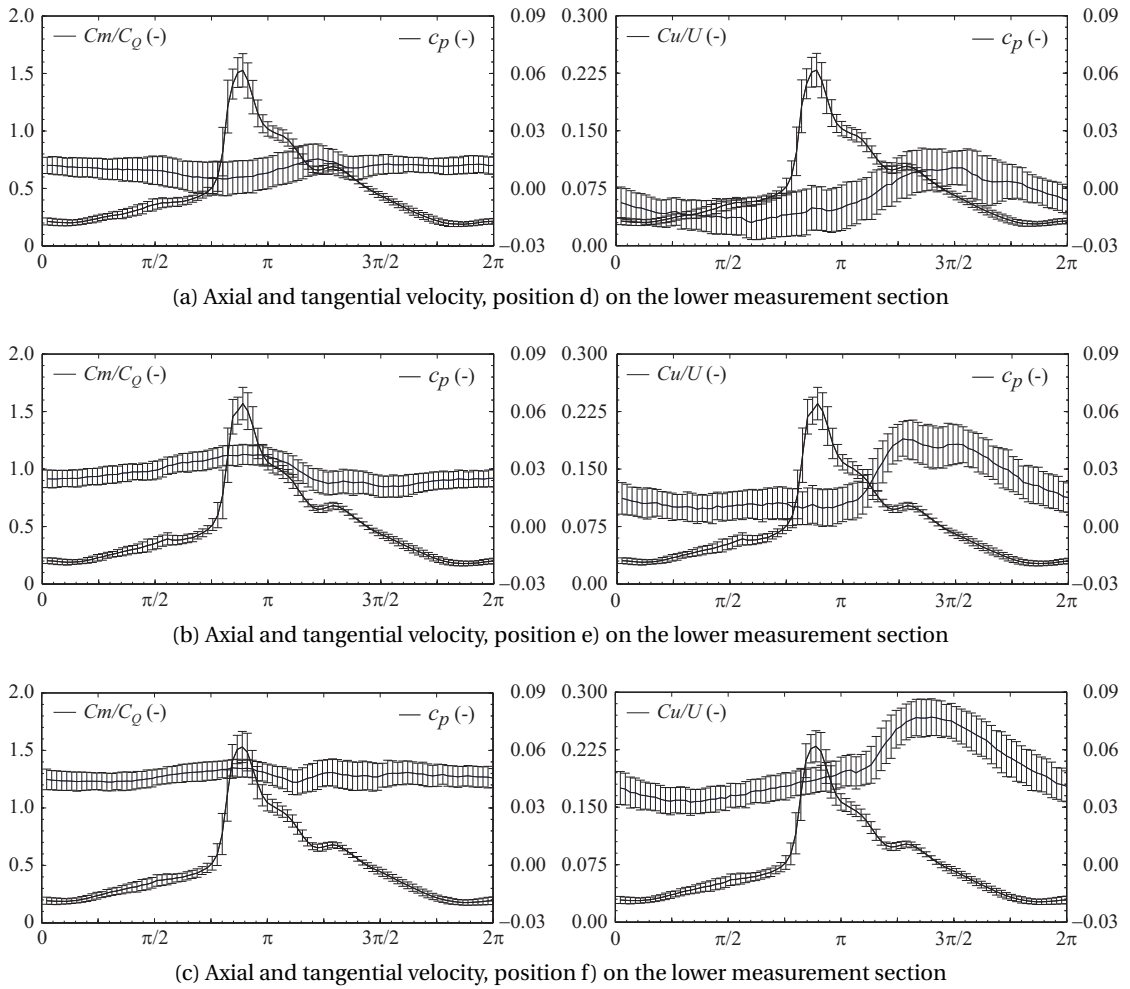
Figure 3.26: Mean phase averaged Cm (left) and Cu (right) at OP#5 ($n_{ED} = 0.288$) together with c_p at C2N (thick line). The x-axis span $[0, 2\pi]$ represents one period of the pressure oscillation.

local Cu-maxima occur with a delay. Finally, it is remarkable that presumably valid LDV data points are obtained even at radial positions towards the centerline, which are partially covered by the vortex rope. The quality of the measurements is often compromised in the vicinity of water-vapor interfaces due to optical issues, such as reflections of the Laser beams on the cavity, or due to a low local density of seeding material.

The same type of analysis is repeated for a lower speed factor of $n_{ED} = 0.273$ at OP#7 in Figure 3.29 and Figure 3.30 for the upper measurement section 1. In case of the axial velocity component Cm, the behavior is comparable to the one observed for the nominal n_{ED} at OP#5, with two zones of local decrease and increase towards the draft tube cone wall and its center, respectively. The corresponding minima and maxima seem to appear at the same location with respect to the pressure peaks. The tangential velocity components Cu are again characterized by a significant maximum around the pressure peak. Its location seems however to be more dependent on the radial position than at OP#5. Moreover, the increase in Cu generally occurs

(a) Axial velocity component

(b) Tangential velocity component
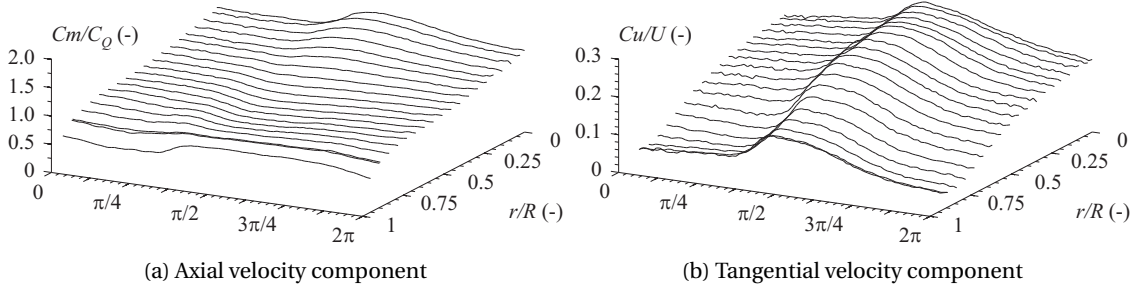
Figure 3.27: Non-dimensional, pressure phase averaged *Cm* and *Cu* profiles for several radial positions at the LDV measurement section 1 for OP#5 (n_{ED} = 0.288).

(a) Axial velocity component

(b) Tangential velocity component
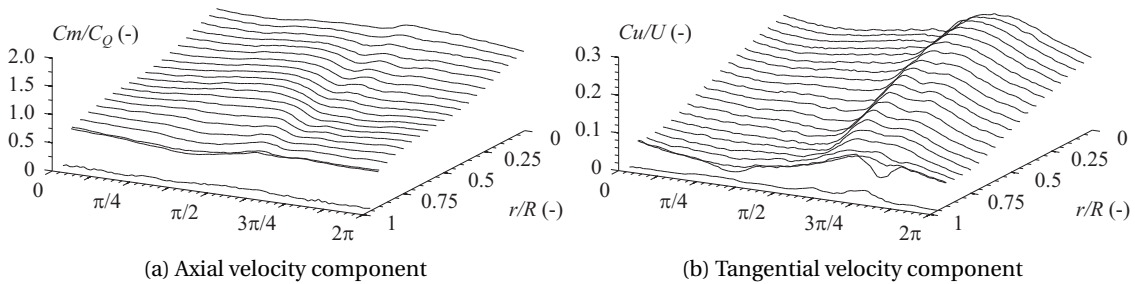
Figure 3.28: Non-dimensional, pressure phase averaged *Cm* and *Cu* profiles for several radial positions at the LDV measurement section 2 for OP#5 (n_{ED} = 0.288).

earlier with respect to the pressure cycle. Close to the center at position c), for instance, the *Cu*-maximum is reached shortly before the pressure peak, in contrast to the same measurement location at OP#5, where this happens shortly after the pressure peak.

Due to reasons mentioned beforehand, the quality of the measurements may decrease towards the center of the draft tube cone in presence of cavitation. This can be seen in Figure 3.30, where the two profiles close to the center display a higher level of fluctuations at their ends. It is also mentioned that the flow is not entirely symmetric with respect to the cone centerline. The center of the vortex is gradually shifted in a positive *x*-direction with a growing distance form the runner outlet, towards the abrupt redirection of the flow in the draft tube elbow.

Axial and tangential velocity, position a) on the upper measurement section

Axial and tangential velocity, position b) on the upper measurement section

Axial and tangential velocity, position c) on the upper measurement section
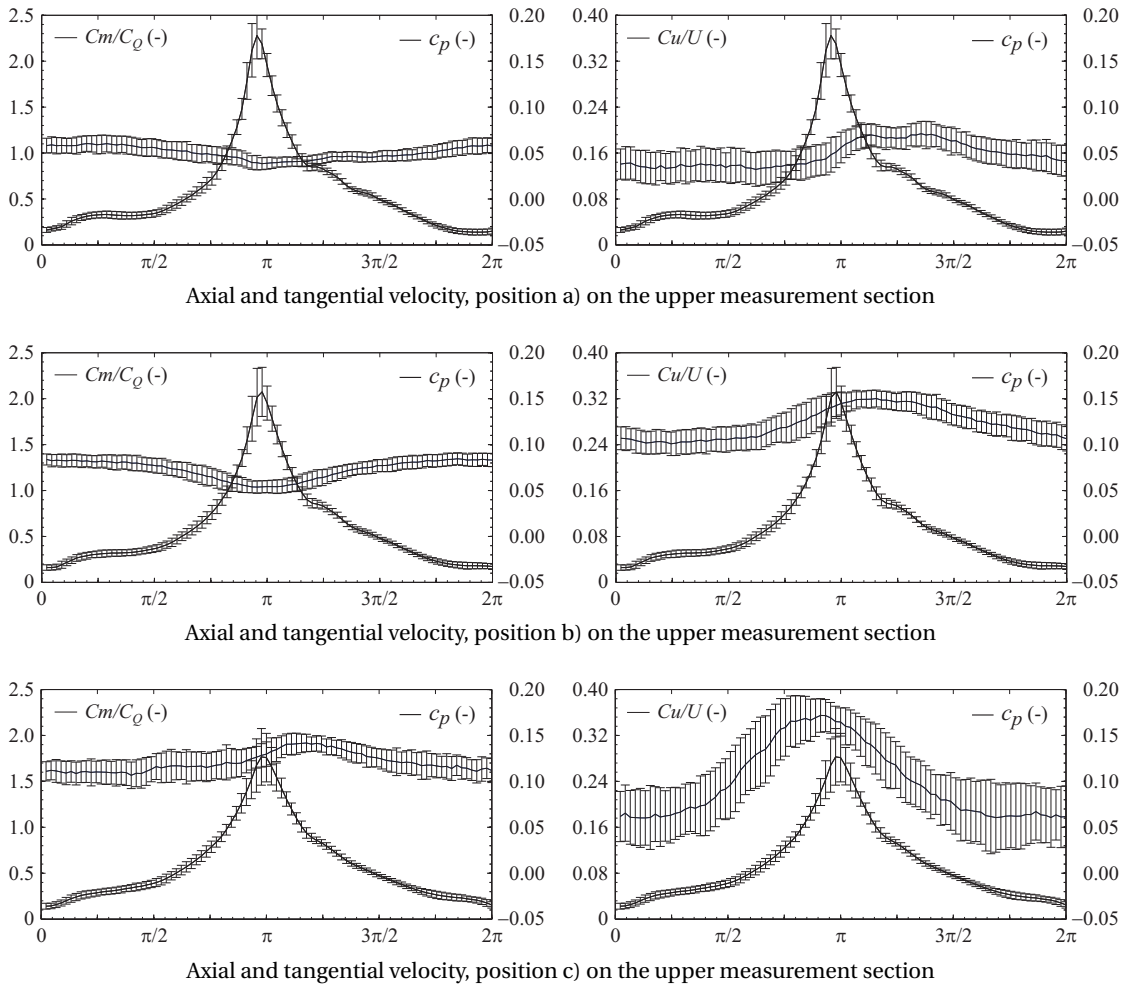
Figure 3.29: Mean phase averaged Cm (left) and Cu (right) at OP#7 together with c_p at C2N (thick line). The x-axis $[0, 2\pi]$ represents one period of the pressure oscillation.

(a) Axial velocity component

(b) Tangential velocity component
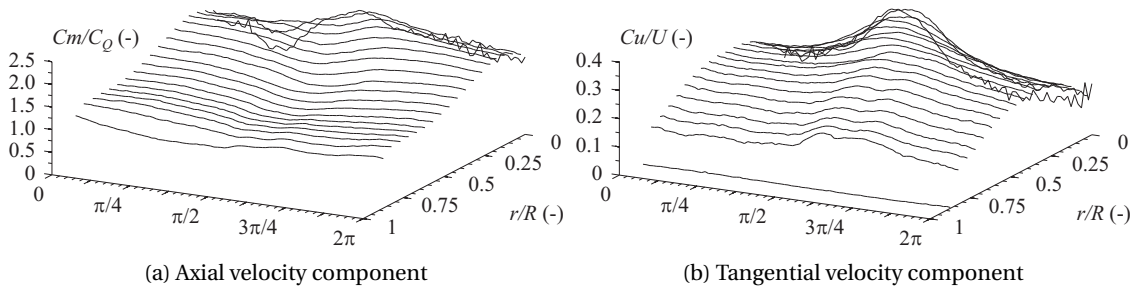
Figure 3.30: Non-dimensional, pressure phase averaged Cm and Cu profiles for several radial positions at the LDV measurement section 1 for OP#7 ($n_{ED} = 0.273$).

3.6.2 Axial velocity profiles from fluorescent PIV

The results presented in this section as well as in Section 3.7 are part of the research paper [43] published by the author. The same operating point is chosen for the following analysis, but with a slightly lower σ in order to assess the influence of a changing draft tube pressure level.

Figure 3.31 contains the axial velocity profiles obtained with PIV at the streamwise Position B, $0.70 \times D_{\bar{1}}$ below the runner exit, at the same six instants shown in Figure 3.11 for OP#2. Each subplot includes the mean velocity data and the standard deviation values resulting from the averaging over 40 vector fields at each measurement point. Both the results based on the raw cross-correlation maps and the validated velocity fields according to Section 3.3.2 are displayed. Furthermore, the vortex rope edge location is estimated with the algorithm introduced in Section 3.3.1 and marked with a vertical dashed line in each subplot. The origin of the x-axis corresponds to the cone centerline and its maximum to the location of the inner cone wall.

It is observed that the calculated edge limits the somewhat chaotic region characterized by large values of the standard deviation fairly well. The growing phase of the vortex rope diameter at this particular position extends to $t = 0.83 \times T$, implying that the collapse of the cavity is very quick, as shown in Figure 3.33. Figure 3.32 shows the profiles of the axial velocity component at the same six instants in one plot for each of the three streamwise Positions A, B, and C.
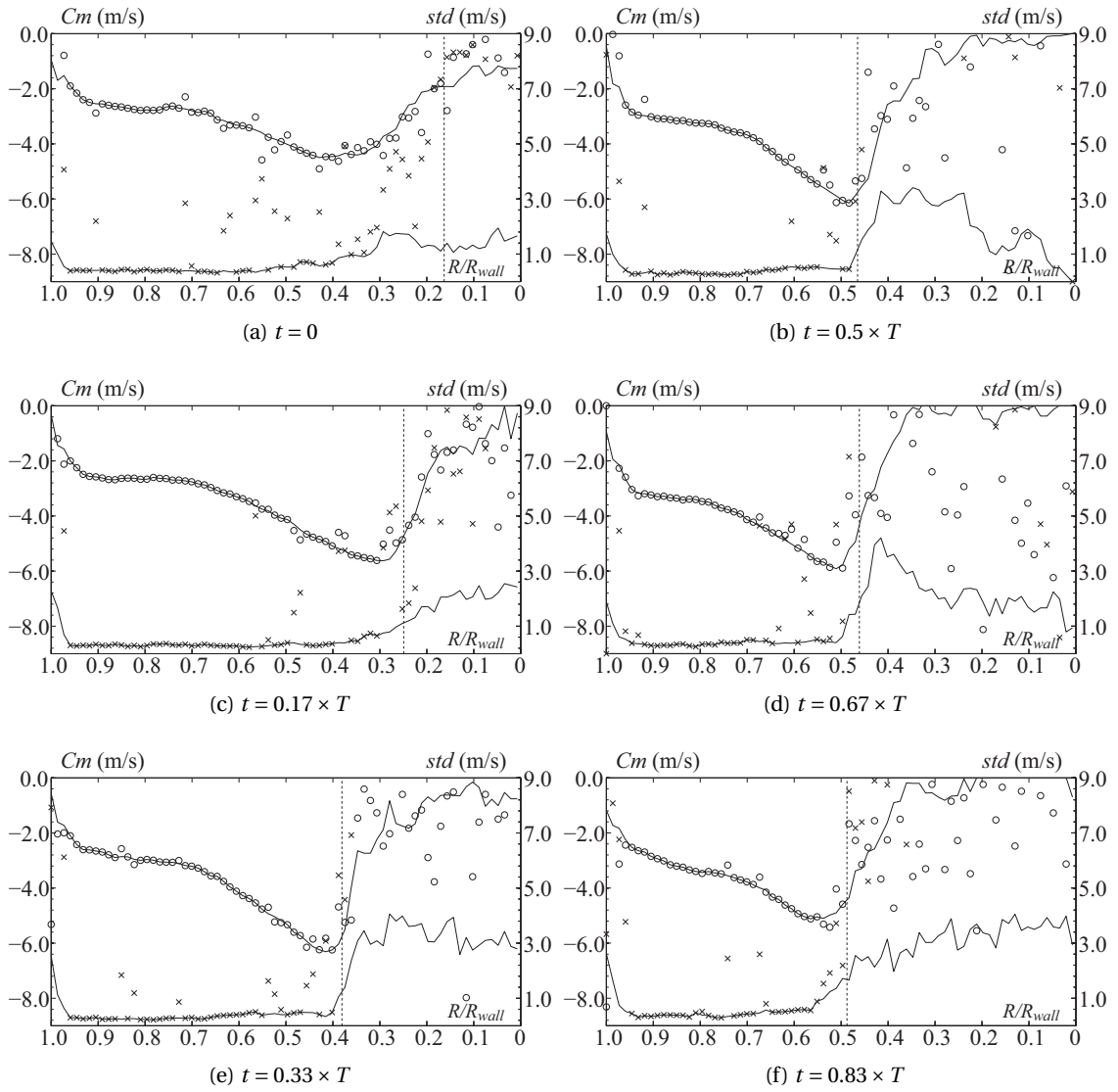
Figure 3.31: Raw and validated radial *Cm* profiles at Position B for OP#2. (◦): raw *Cm*, (×): raw *std*, solid lines: validated *Cm* (top) and *std* (bottom).
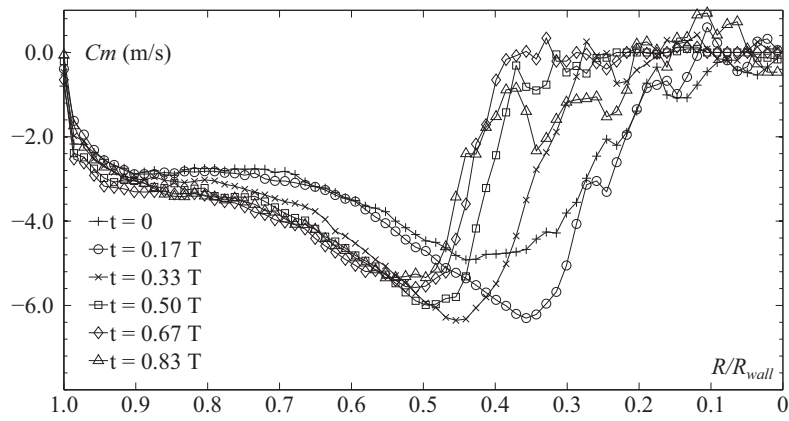
(a) Position A, $0.55 \times D_{\bar{1}}$ below the runner exit
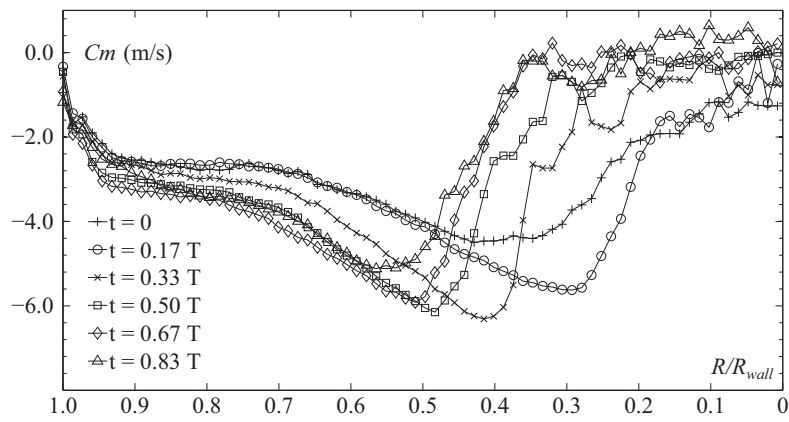
(b) Position B, $0.70 \times D_{\bar{1}}$ below the runner exit
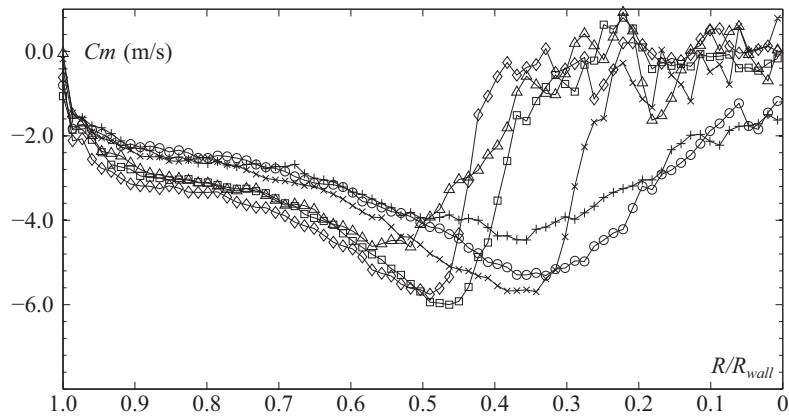
(c) Position C, $0.84 \times D_{\bar{1}}$ below the runner exit

Figure 3.32: Radial profile plots of the validated axial velocity component Cm at OP#2 for the Positions A, B, and C.

3.7 Local discharge variation around the vortex rope

3.7.1 Calculation of the discharge area

With the method described in Section 3.3.1, the instantaneous vortex rope radius can be estimated at the three measurement positions A, B and C. This radius is then used in the discharge calculation using eq. (3.2). Figure 3.33 shows the corresponding variation over one period of the pressure oscillation. In the rare cases no valid vortex rope radius is detected, a linear interpolation is performed based on the adjacent measurement points. The window size for the spatial filter described in Section 3.3.1 is set to 1×4 pixel for the Position A, since the reflection of the light sheet is not very distinct at the corresponding streamwise position, as can be observed in Figure 3.11. The detection of the vortex rope edge is consequently less accurate, as evidenced by the unsteadiness of the corresponding curve. For the Positions B and C, the window size is 1×8 pixel. It is noticed that the vortex rope radius does not reach zero at the collapse, which does not necessarily correspond to the reality. The resulting underestimation of the discharge during these moments is discussed in a later Section.
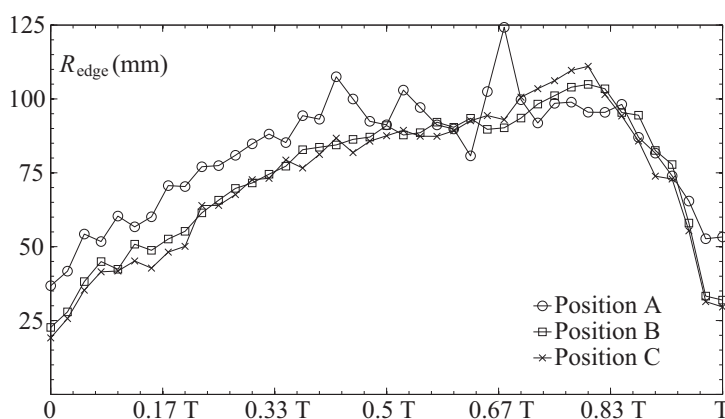
Figure 3.33: Variation of the instant vortex rope radius over one period of the pressure oscillation at three streamwise positions in the draft tube cone for OP#2.

In order to compensate for the lack of reliability of the edge detection in certain regions and to get more continuous estimates of the discharge evolution, the radius curves in Figure 3.33 are smoothed. It is found that a 8th degree polynomial interpolation is a good fit in capturing the different phases of the vortex rope radius variation, as demonstrated in Figure 3.34.

3.7.2 Flow rate variation around an oscillating vortex rope

From the axial velocity profiles and the local vortex rope radius in Section 3.6.2 and Section 3.7.1 at a particular streamwise position, the corresponding volumetric flow rate around the cavity is estimated. Several measurements taken at different instants over one pressure oscillation cycle are put together in order to reconstruct the evolution over an entire pressure oscillation period. For the operating point labeled OP#2, the results are presented in Figure

(a) Position A, $0.55 \times D_{\bar{1}}$ below the runner exit

(b) Position B, $0.70 \times D_{\bar{1}}$ below the runner exit

(c) Position C, $0.84 \times D_{\bar{1}}$ below the runner exit
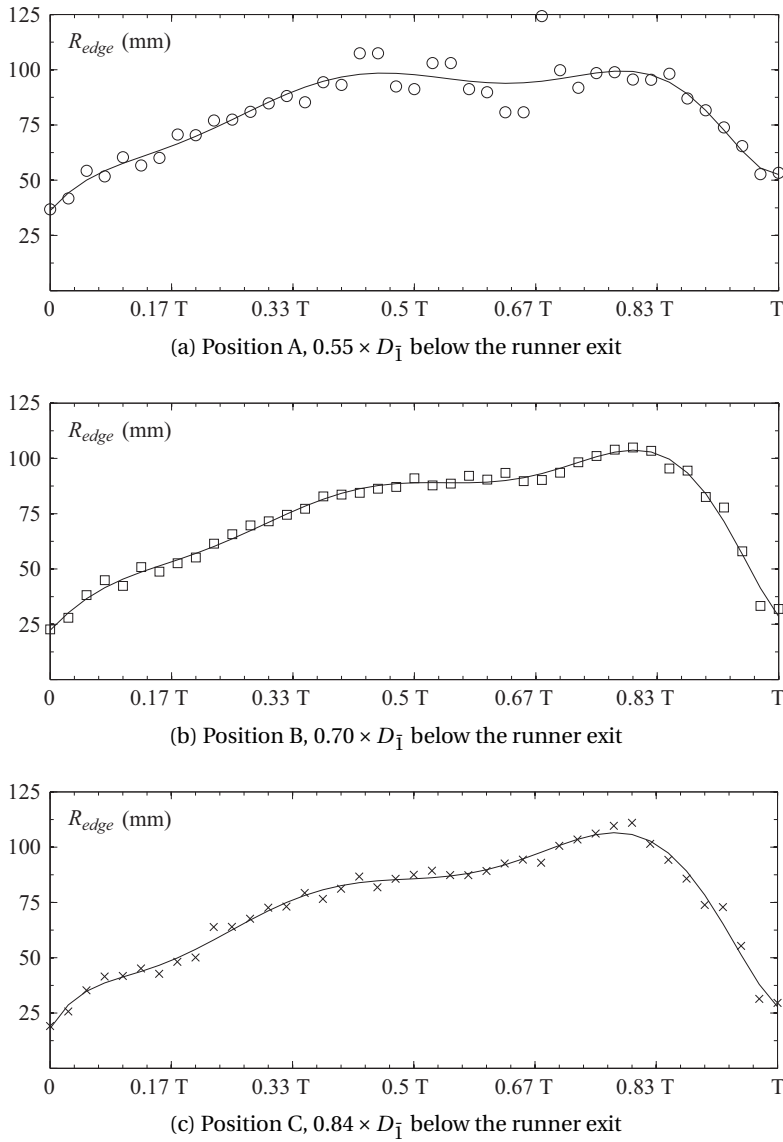
Figure 3.34: Vortex rope radius over one period of the pressure oscillation at three streamwise positions in the draft tube cone for OP#2, together with a 8th degree polynomial fit.

3.35a. The flow rate is made non-dimensional by the mean discharge measured in an upstream pipe with an electromagnetic flowmeter and is based on the fitted vortex rope radii presented in Figure 3.34.

A comment about the definition of the phase angle on the x-axis needs to be made before comparing the estimated flow rate to other quantities, such as the pressure, instantaneous velocity components from LDV or the vortex rope volume. The displayed period is simply a discretization of the interval $[0, 2\pi]$ by the number of PIV measuring points. As explained in Section 3.2.2, each of these measuring points stands for a different trigger delay value. Since the trigger itself is released at a constant but arbitrary voltage level of the wall pressure signal

(see TTL trigger output in Figure 3.6), no direct link to the instant phase defined in Section 3.3.4 may be established. However, the internal signal which triggers the actual Laser pulse from the timing box can be recorded and its time shift with respect to the adjacent pressure peaks is then determined in post-processing. This time shift is consequently averaged over all measurements at a given measuring point and compared to a mean phase averaged reference wall pressure signal obtained from the totality of recorded pressure cycles at C1N. Finally, a mean wall pressure value can be determined for each trigger delay in order to reconstruct the mean pressure fitting the PIV period. The corresponding signal is shown in Figure 3.35b.

(a) Flow rate fluctuation

(b) Mean wall pressure factor
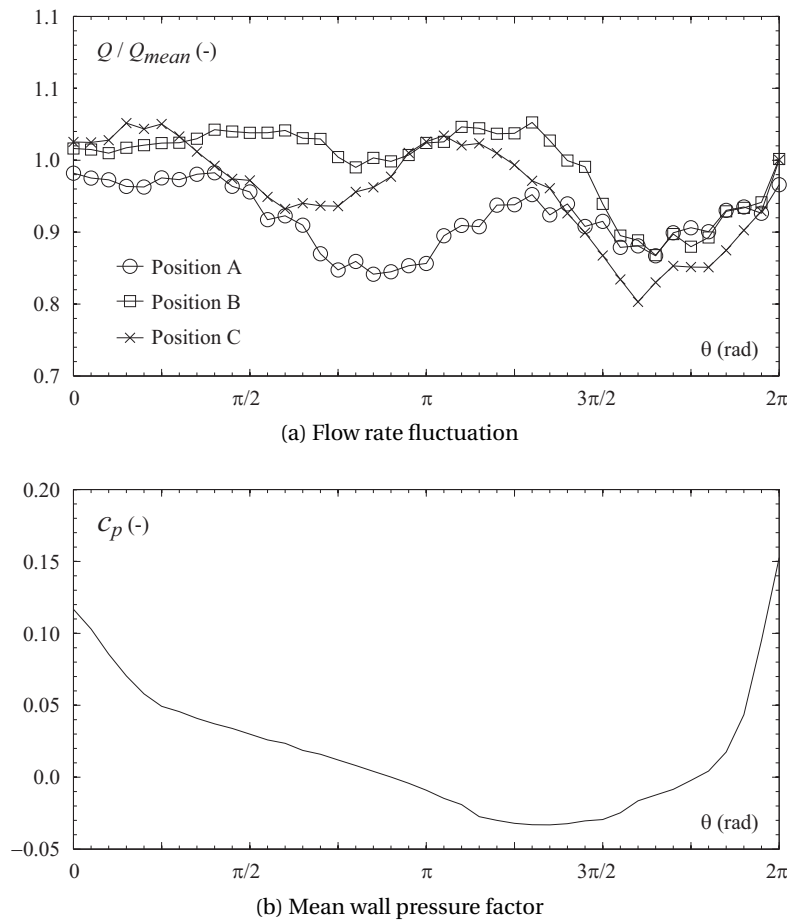
Figure 3.35: Dimensionless flow rate evolution at the positions A, B and C and corresponding mean wall pressure factor c_p at C1N.

The variation towards the end of the period observed at all three measurement positions A, B and C seems to coincide with the rising phase of the wall pressure signal. Other correlations with the pressure signal are not apparent. As for the individual behavior, all curves experience a local minimum between $\pi/4$ and $5\pi/4$ at varying amplitudes and locations. The flow rate at position B displays the most continuous behavior close to the nominal discharge, where as the corresponding curve at position A runs significantly below. With mean values of 92.0%, 99.5% and 95.8% over the whole period,respectively, the mean discharge in the test rig is only

matched at position B. However, in view of the significant discharge oscillations that may exist upstream and downstream of the vortex rope and the periodically chaotic nature of the flow, the significance of the quantitative aspects of these findings is limited.

As briefly mentioned before, the accuracy of the shown result may suffer lightly from an unde-sired change in the operating conditions during the time it takes to record all the measuring points constituting one period of the pressure oscillation. It is for instance challenging to maintain a constant pressure in the downstream reservoir with the vacuum pump over several hours. The reason are small leakages in the system, which ultimately lead to a modification of the cavitation number and therefore the properties of the vortex rope oscillation.

The use of a more powerful laser device for the PIV measurements in the future will expand the target area in the draft tube cone where the flow rate can be estimated. Furthermore, it will increase the reliability of the detection of the vortex rope edge with the algorithm described in Section 3.3.1 and hence the calculation of the discharge at the given streamwise location.

3.8   Summary and discussion

At the end of this chapter, a deep knowledge of the flow field properties throughout the draft tube cone is acquired for several operating conditions. After a description of the experimental setup for the LDV and PIV measurements as well as the flow visualization, an additional method for the estimation of the vortex rope volume based on the local radius of the vortex rope is introduced. This integral method as well as the differential approach described in Section 2.3.3 agree well with each other and deliver satisfying results for the volume of the visible portion of the vortex rope in the draft tube. The reliability of the integral method may be compromised around the collapse of the cavity and the bubbly flow phases, whereas the output from the differential method is biased when ambient light is reflected at the vortex rope interface.

The vortex ropes at a nominal speed factor of $n_{ED} = 0.288$ and at a lower value of $n_{ED} = 0.273$ display diverging properties in terms of their volume. The first one, having a rather slender shape as opposed to the large cavity at $n_{ED} = 0.273$, reaches its maximum volume together with the pressure and is characterized by a very rapid growth. The vortex rope at the lower n_{ED} however seems much more inert in the growing phase and is therefore shifted with respect to the pressure signal, in a way of reaching its maximum when the wall pressure is minimal and vice versa. The difference in the runner inlet flow incidence angle between the two operating points might play a role in this, as it directly impacts the volume of the previously mentioned cavitation on the runner blades. The amount of blade cavitation is expected to be higher for $n_{ED} = 0.273$, which is evidenced by the increased amount of bubbles in the surrounding flow. The common point is that for both n_{ED} values, the start of the growing phase of the vortex rope seems to coincide with the disappearance of the bubbles in the flow. This moment corresponds to the end of the highly fluctuating section covering the minima of the wall pressure signals at the upper measurement section.

The velocity profiles at cavitation-free conditions agree with classical vortex and swirling jet theories. The effect of the adverse pressure gradient on the shape of the velocity profiles is illustrated by a systematic variation of the discharge factor Q_{ED} and hence the draft tube inlet flow swirl. The results suggest the presence of a critical swirl number of about 0.385 around a discharge factor of $Q_{ED} = 0.254$ at a speed factor of $n_{ED} = 0.273$.

The velocity components from the LDV measurements are averaged with respect to the instant phase of the wall pressure signal. The resulting profiles display a significant increase of the tangential velocity component Cu following the pressure maximum, at all radial measurement positions. This is at the origin of a periodic variation of the flow swirl in the draft tube, which is going to be discussed in Chapter 4.

The axial velocity profiles from the PIV measurements together with the local vortex rope radius obtained from image processing are used to calculate the instant discharge around the vortex rope at a certain moment, at a certain streamwise position. Repeating this for several measurement points systematically distributed over the pressure oscillation period, the corresponding flow rate fluctuation is established. It features a local minimum at all the investigated streamwise positions when the pressure in the draft tube rises.

4 Angular momentum balance

4.1 Swirl variation in the draft tube

The axial and especially tangential velocity profiles presented in Section 3.6.1 indicate a significant variation of the draft tube flow swirl. The latter is represented by the swirl number S, which is defined as the ratio between the axial flux of the angular momentum (G_θ) and the axial flux of the axial momentum (G_z) [26]. It takes the expression

$$
S = \frac{\int\limits_0^R r^2 \cdot Cu \cdot Cm \, \mathrm{d}r}{R_{\bar{1}} \cdot \int\limits_0^R r \cdot Cm^2 \, \mathrm{d}r}
\tag{4.1}
$$

where $R_{\bar{1}}$ is the external runner outlet diameter. The axial and tangential velocity components Cm and Cu are available from the LDV measurements and the instantaneous swirl number can therefore be estimated on both LDV measurement sections shown in Figure 3.2. The procedure is based on the mean phase averaged velocity profiles displayed in Figures 3.27, 3.28 and 3.30, where eq. (4.1) is calculated at each step of the phase angle $\theta \in [0, 2\pi]$. Ultimately, this results in the evolution of the flow swirl over one period of the pressure oscillation.

The mean phase averaged vortex rope volume and the swirl number are both based on the instant phase of the pressure oscillation. The reference signal is however not the same, since the measurements were recorded at different moments. As mentioned earlier, the physical conditions may be subject to natural fluctuations between two tests at the same operating point. Moreover, in case of the swirl number, there are as many reference signals as there are radial LDV measurement positions. Hence, before any conclusions with regard to the relationship between the swirl and the vortex rope volume can be drawn, the corresponding mean phase averaged reference pressure signals need to be compared. This is illustrated in Figure 4.1 for the upper measurement positions at OP#5 and OP#7. In case of the swirl number,

the displayed c_p-curve is an average over all the radial measurement positions. In order to enhance the readability of the graphs, the statistical error is not included.

(a) Upper position, OP#7 ($n_{ED} = 0.273$)
(b) Upper position, OP#5 ($n_{ED} = 0.288$)
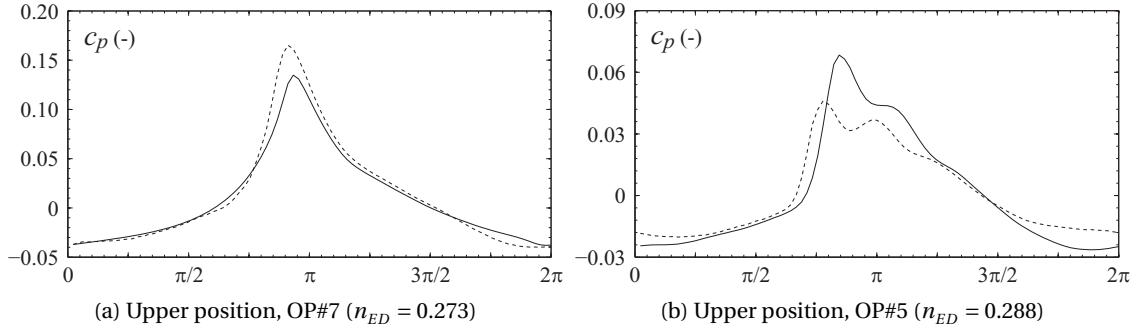
Figure 4.1: c_p mean phase averaged corresponding to the LDV measurements (solid lines) and the flow visualizations (dashed lines).

While the agreement is very good for OP#7, a more substantial difference between the two curves in the region of the pressure maximum is observed at OP#5. The location of the peak with respect to the overall period is however nearly identical and the following analysis remains therefore valid. Figure 4.2 shows the swirl number over one period of the pressure oscillation, together with the mean phase averaged wall pressure factors (C1N) and vortex rope volumes on both LDV measurement sections at OP#5. For the upper position in Figure 4.2a, close to the runner exit, the swirl number and the c_p display a very similar shape. The jump in the flow swirl at roughly $5\pi/8$ is very abrupt, swiftly followed by the pressure rise and then eventually by the vortex rope volume. As already foreshadowed by the local tangential velocity profiles in Section 3.6.1, the modification of the flow swirl arrives at the lower LDV measurement section with a significant delay (see Figure 4.2b).

For the upper position at OP#7, the evolution of the flow swirl, the vortex rope volume and the wall pressure factor are plotted in Figure 4.3. Other than the mean swirl being on a higher level, the relationship between the displayed quantities is slightly different with respect to the previously presented OP#5. This is to be expected in view of the results presented in Section 3.4, showing already a different evolution of the vortex rope volume compared to the wall pressure cycle. In the present case, the maximum of the flow swirl corresponds to the low point of the vortex rope volume. The wall pressure follows behind with a phase shift of roughly $\pi/4$. Around the pressure maximum, the decrease of the swirl and the raise of the vortex rope volume temporarily flatten.

4.2 Evidence of periodic blade cavitation appearance

As indicated earlier, CFD calculations based on the experimental data from the reduced scale model testing suggest a significant presence of cavitation on the low pressure side of the runner blades [9]. This is verified by high speed visualization with the setup shown in Figure 3.7. For

(a) S and c_p, upper section

(b) S and c_p, lower section

(c) S and V_c, upper section

(d) S and V_c, lower section

Figure 4.2: Swirl number together with the mean wall pressure factor and the vortex rope volume over one period of the pressure oscillation at OP#5 ($n_{ED} = 0.288$).

this purpose, the runner is illuminated from below with a stroboscope, which is synchronized with the camera. At a frequency of eight times the one of the runner, an image is recorded at each light pulse. The visualization is synchronized with the wall pressure measurements and Figure 4.4 shows one period of the raw c_p signal including the instants (a) to (p) at which the images in Figure 4.5 are recorded.

The chosen perspective shows the suction side of three out of a total of sixteen runner blades. The view is barely obstructed by the vortex rope, since the latter is comparatively slim at this particular operating point (see Figure A.2). The vortex rope is partly visible in the lower right corner of the individual images, allowing to follow simultaneously the evolution of V_c.
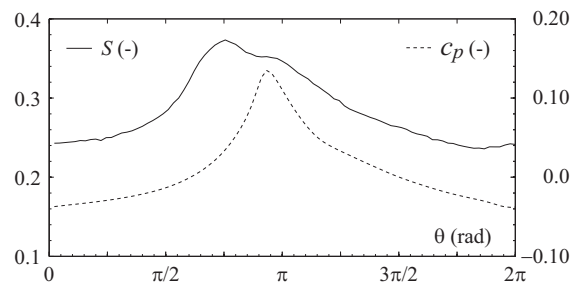
(a) S and c_p, upper section
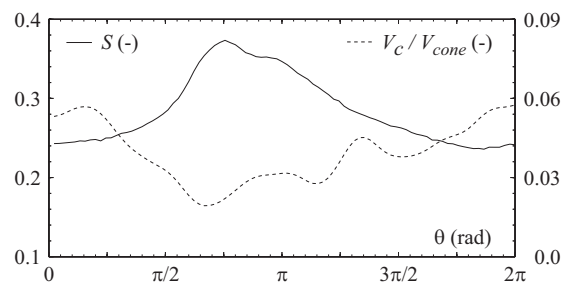
(b) S and V_c, upper section

Figure 4.3: Swirl number together with the mean wall pressure factor and the vortex rope volume over one period of the pressure oscillation at OP#7 ($n_{ED} = 0.273$).
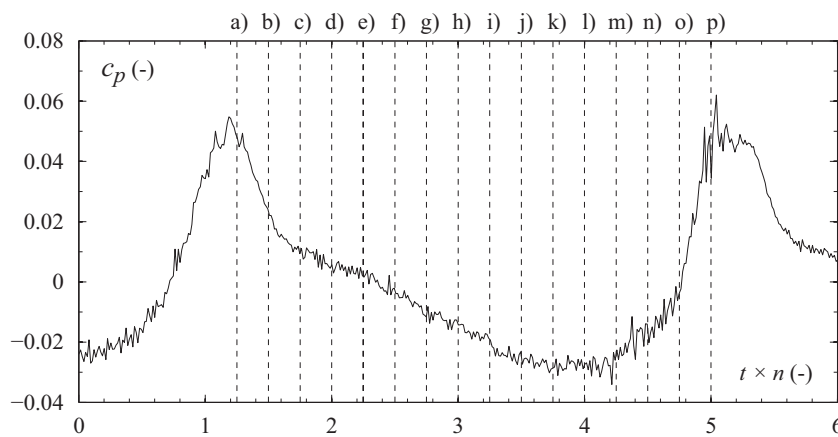
Figure 4.4: Wall pressure factor at C1N for OP#5 ($n_{ED} = 0.288$) plotted against the number of runner revolutions, together with the moments corresponding to the pictures in Figure 4.5 (vertical dashed lines).
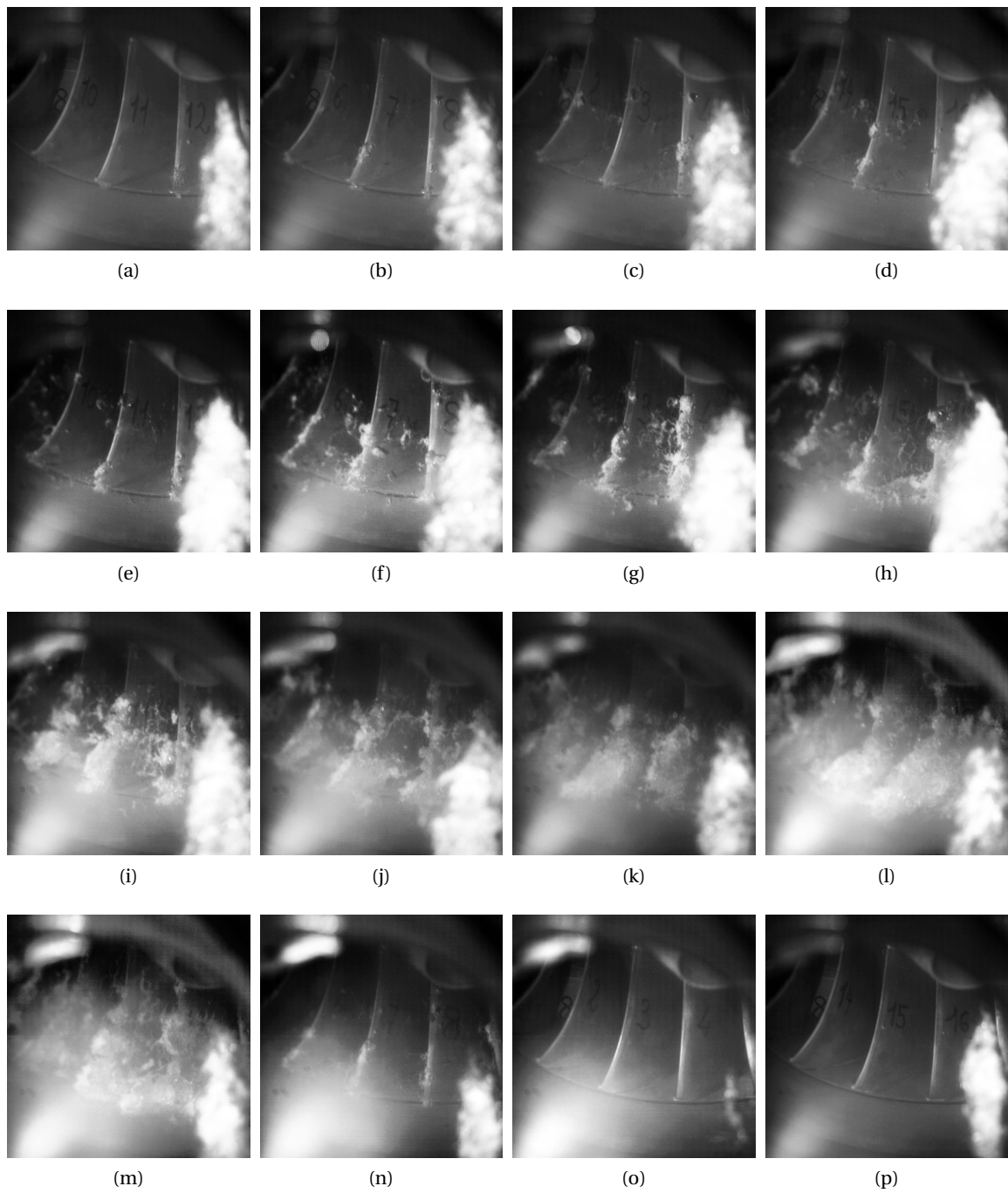
Figure 4.5: Formation of cavitation on the runner blades at OP#5 (n_{ED} = 0.288) during one period of the pressure oscillation (see Figure 4.4 for corresponding c_p values).

4.3   Calculation of the relative flow angle β

The cavitation on the runner blades causes a modification of the relative flow angle β at the runner outlet. According to the velocity triangles in Figure 2, it is defined as

$$\beta = \tan^{-1}\left(\frac{Cm}{U - Cu}\right).$$ (4.2)

The value of β should be constant on a given measurement section, since it is directly linked to the runner geometry. Except for the wake in the central region of the cone. Figure 4.6 shows the profiles of β on the upper LDV measurement section for six equally spaced instants over one period T of the pressure oscillation at OP#7 and OP#5. The three vertical dashed lines correspond to the radial locations (a), (b) and (c) from Figure 3.23, for which the time-wise evolution based on the pressure phase averaged velocity components are shown in Figure 4.7. The mean value of the peripheral velocity U is used in eq. (4.2), even though the instant runner speed experiences periodic fluctuations as shown in Figure of Section 4.4. The amplitude of the fluctuations is however too small to cause a noticeable difference in β.

(a) Relative flow angle at OP#7, $n_{ED} = 0.273$ (b) Relative flow angle at OP#5, $n_{ED} = 0.288$
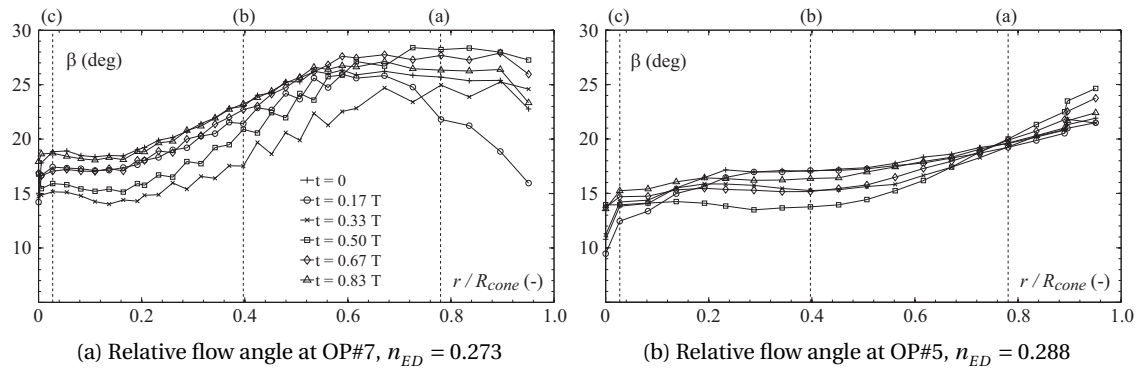
Figure 4.6: Relative flow angles as a function of the dimensionless cone radius at six instants of the pressure oscillation period at OP#7 and OP#5.

The variation of the relative flow angle is more significant for the lower speed factor at $n_{ED} = 0.273$. A distinctive minimum is especially observed at the radial position (b) in Figure 4.7. Said minimum occurs later for $n_{ED} = 0.288$ than for $n_{ED} = 0.273$ with respect to the mean period of the pressure oscillation and coincides with the swirl maximum in Figure 4.2a and Figure 4.3a.

4.4   Runner speed and torque fluctuations

The significant variation of the swirl number shown above suggests a measurable interaction of the flow in the draft tube with the mechanical system of the test rig. A high-resolution angular encoder used with a counter/timer module offers the possibility of studying the

(a) Relative flow angle at OP#7, $n_{ED} = 0.273$

(b) Relative flow angle at OP#5, $n_{ED} = 0.288$
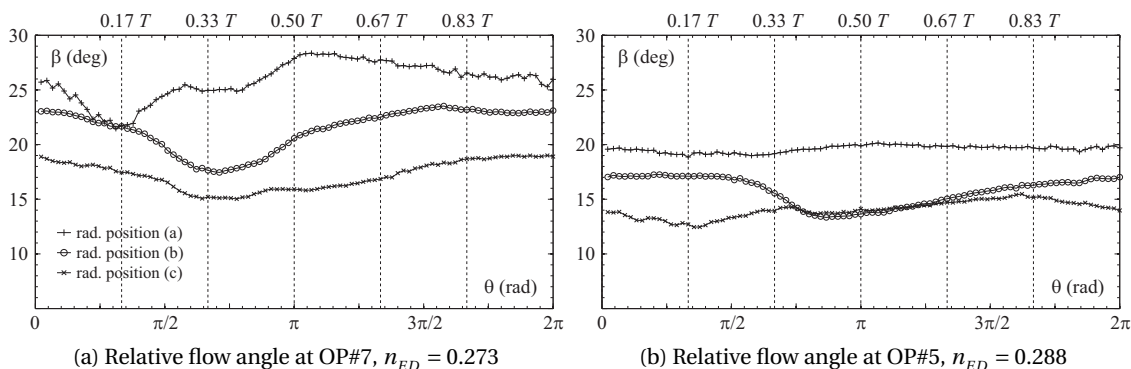
Figure 4.7: Relative flow angles as a function of the mean phase angle at six instants of the pressure oscillation period at OP#7 and OP#5.

instant runner frequency. The angular encoder has an output of 18'000 pulses per revolution and the counter/timer card, which is integrated in the PXI system, features a 80 MHz timebase or in other words a maximum resolution of 12.5 ns. A torquemeter on the runner shaft provides the instant torque values. Figure 4.8 shows the time history of these two quantities for the two operating points OP#5 and OP#7 at a speed factor of $n_{ED} = 0.288$ and $n_{ED} = 0.273$, respectively. The graphs for the runner speed contain the result based on a discretization of the circumference into 2'000 segments and a smoothed version based on a low pass filter.

Significant oscillations are observed in both the runner frequency and the torques at both operating points. The peak-to-peak amplitudes of the runner frequency fluctuation are between 0.5-1% of the specified value of 800 rpm and 505 rpm, respectively. The signal is more regular for OP#5, whereas higher frequency components are present in the oscillation of the runner speed at OP#7. The same can be said about the torque oscillation. In terms of the amplitudes, the torque reaches peak-to-peak values between 4-6% of the mean value at the given operating point. In view of the relationship $P = T_m \times \omega$, this has a non-negligible impact of the power output of the machine.

Figure 4.9 shows the pressure phase averaged signal of the runner speed and the torque, together with the mean phase averaged wall pressure reference signal at the sensor location C1N. This representation places the measurements displayed in Figure 4.8 in the general context of the instability by studying their evolution with respect to the same reference signal that was used in previous sections. Unsurprisingly, the rotating frequency and torque oscillations are nearly in phase. The torque peak is only slightly following behind the maximum of the runner frequency ($0.16 \cdot \pi$ for $n_{ED} = 0.288$ and $0.27 \cdot \pi$ for $n_{ED} = 0.273$). With regard to the reference signal, the maxima of the torque and the runner frequency occur during the falling edge of the wall pressure.

(a) Runner speed at OP#7 ($n_{ED} = 0.273$)

(b) Runner speed at OP#5 ($n_{ED} = 0.288$)

(c) Mechanical torque at OP#7 ($n_{ED} = 0.273$)

(d) Mechanical torque at OP#5 ($n_{ED} = 0.288$)
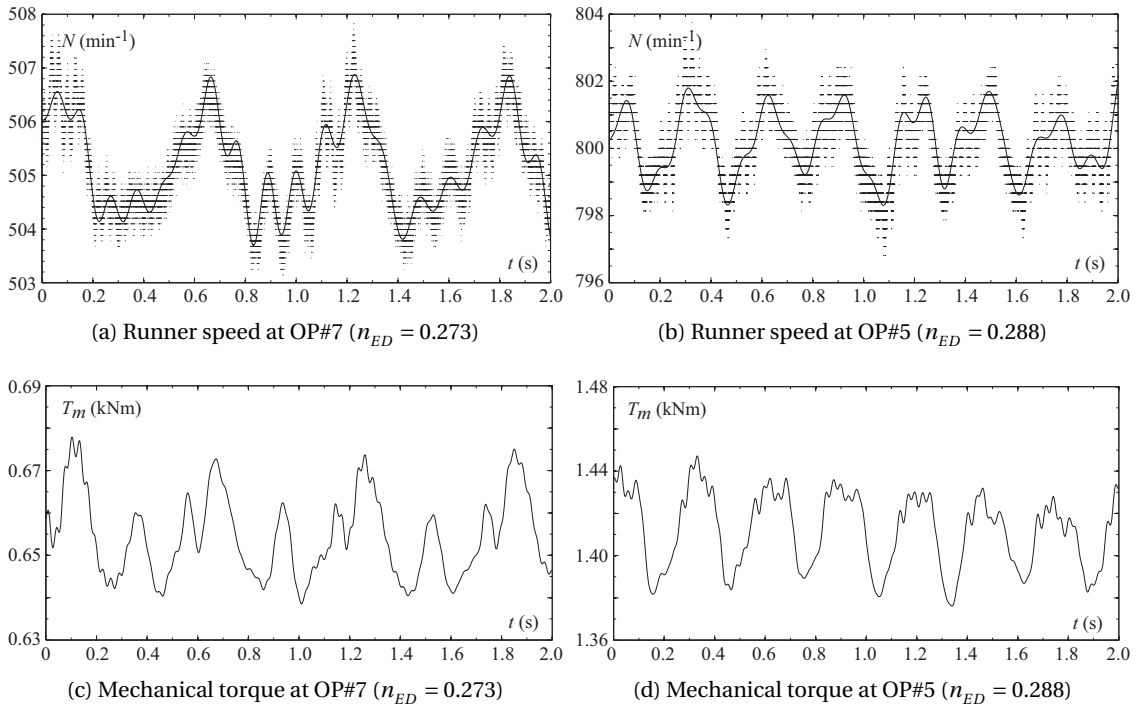
Figure 4.8: Variation of the runner frequency and of the mechanical torque at OP#7 ($n_{ED} = 0.273$) and OP#7 ($n_{ED} = 0.288$).

(a) Runner speed at OP#7 ($n_{ED} = 0.273$)

(b) Runner speed at OP#5 ($n_{ED} = 0.288$)

(c) Mechanical torque at OP#7 ($n_{ED} = 0.273$)

(d) Mechanical torque at OP#5 ($n_{ED} = 0.288$)
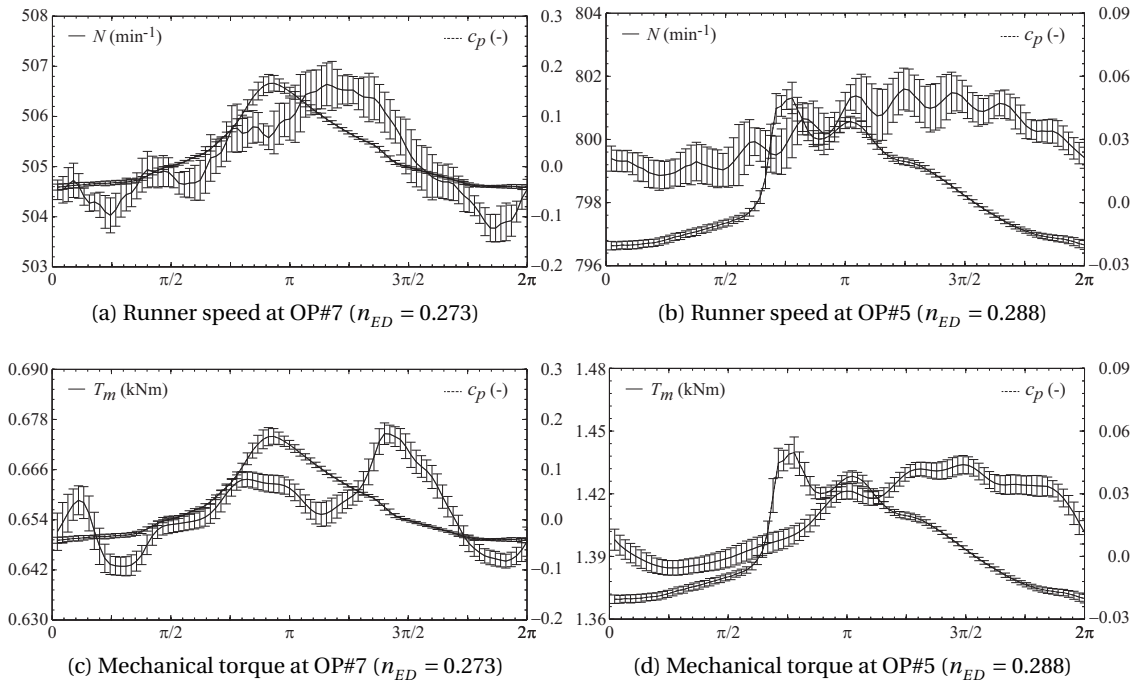
Figure 4.9: Pressure phase averaged runner frequency and mechanical torque at OP#7 ($n_{ED} = 0.273$) and OP#5 ($n_{ED} = 0.288$) together with mean phase averaged c_p at C1N.

4.5 Summary and discussion

Based on the LDV measurements presented in Chapter 3, the draft tube flow swirl is calculated and a significant periodic variation is observed. At the upper measurement section, the swirl peak occurs almost simultaneously with the pressure peak for a higher speed factor of $n_{ED} = 0.288$, whereas it has a short advance on the pressure for $n_{ED} = 0.273$. The swirl maximum corresponds to the vortex rope maximum at $n_{ED} = 0.288$, whereas it coincides with the volume minimum for the lower n_{ED} value.

The cavitation on the runner blades is visualized for $n_{ED} = 0.288$. It is observed that at the pressure peaks, no traces of cavitation are found and that the start of the fluctuating segment of the wall pressure signal coincides with the appearance of the first cavities on the runner blades.

Furthermore it is shown that the swirl modification is accompanied by a modification of the relative flow angle β at several radial positions. The β-profiles along the radius display significant changes, which are more pronounced for $n_{ED} = 0.273$. It is curious that values of the relative flow angle seem generally lower for $n_{ED} = 0.288$, since β should not depend on the operating conditions.

Periodical variations of the instant runner frequency and the mechanical torque are documented. The torque peaks have a slight delay with respect to the maxima of the runner frequency at both speed factor values of $n_{ED} = 0.288$ and $n_{ED} = 0.273$. The amplitude of the fluctuations are $0.5 - 1\%$ for the runner frequency and $4 - 6\%$ for the mechanical torque, indicating significant power swings.

Finally, the presented findings suggest a strong link between the self-sustained pressure oscillations, the flow swirl and the cyclic appearance of cavitation on the runner blades, which needs to be further investigated.

5 Conclusions and perspectives

5.1 Conclusions

At full load operation, characterized by discharge values beyond the best efficiency point, hydraulic machines may experience self-excited pressure and cavitating vortex rope oscillations. The physical properties of this phenomenon differ fundamentally from well documented instabilities involving cavitation at a partial load range. Extensive experimental investigations are therefore performed to increase the understanding of its underlying causes and key sustaining mechanisms.

A detailed characterization of the wall pressure evolution throughout the hydraulic system as well as the flow field in the draft tube cone is performed on a 1:16 reduced scale physical model of a Francis turbine. Furthermore, the interaction with the mechanical system is studied. The use of state of the art measurement techniques, such as Laser Doppler Velocimetry, fluorescent Particle Image Velocimetry and high-speed flow visualization as well as the development of appropriate signal processing tools grants access to the important physical quantities involved. It is hence possible to simultaneously study the wall pressure P, the axial and tangential velocity components Cm and Cu at various streamwise and radial locations, the instant flow rate Q around the vortex rope, the vortex rope volume V_c, the swirl number S, the relative flow angle β, the instant torque T and the runner frequency n for a large range of operating conditions. An averaging of all these signals with respect to a mean phase of the pressure oscillation makes a direct comparison between them possible. The results suggest a strong link between the periodically changing flow configuration in the draft tube cone in terms of the swirl and the cyclic appearance of cavitation on the runner blades. Both the swirl and the blade cavitation have a constant phase relationship with the dominant wall pressure oscillations. This observation is in agreement with the results obtained from recent multi-phase numerical simulations, coupling the draft tube and the runner, which accurately reproduced the pressure fluctuations and the characteristic vortex rope oscillation measured on the reduced scale model. The experiments conducted on the reduced scale model constitute a comprehensive data resource for the validation of analytical and numerical flow models.

In a further effort, self-excited pressure oscillations are reproduced and investigated on a simplified, small scale test facility with a micro-turbine and a horizontal conical diffuser. The unsteady flow rates upstream and downstream of the draft tube are calculated using pressure transducers and the vortex rope volume is estimated from flow visualizations, thus enabling the study of the hydroacoustic draft tube flow parameters found in commonly used one-dimensional models. Representing the vortex rope volume as a function of the mentioned flow rates and the cavitation number suggests that the flow swirl at the runner outlet (draft tube inlet) plays a crucial role in the destabilizing of the system. The cavitation compliance for a given operating point can be approximated by a constant value from a linear fit of the raw data, where as the accuracy of the mass flow gain factor calculation suffers from singularities in the partial derivatives which define them.

It is concluded that the modification of the flow swirl in the draft tube inlet through the appearance of cavitation on the runner blade plays an important role in the feedback mechanism of the self-excited pressure and vortex rope oscillation.

5.2 Perspectives

The vast amount of experimental data collected during this research project allows an extension of the presented analysis to a larger operating range. Given the sometimes divergent behavior between the different speed factors, for instance, in terms of the vortex rope volume and the flow swirl evolution with respect to the pressure signal, additional data points are to be taken into account in order to understand the dependencies of the important variables on certain operating conditions. A systematic comparison of the time for the collapse and the rebuilding of the vortex rope between the various operating points is to be performed.

For future investigations, several strategies should be considered in light of the above findings. The analysis of the hydroacoustic draft tube parameters on a simplified test case yielded encouraging results. Performing this on a reduced scale model may produce a stability map and the definition of stability criteria based on said hydroacoustic model parameters. For this purpose, the upstream and downstream flow rate should be measured on the test rig. The results would also benefit from a slightly more realistic estimation of the vortex rope volume. Finally, the dynamic transfer matrix could be calculated with such an equipment.

Based on the estimation of the instant flow rate from the PIV measurements and the vortex rope volume in the draft tube cone, a local mass balance can be established at several streamwise locations. Moreover, the mass flow gain factor, defined as the change in the vortex rope volume with respect to the flow rate, can be estimated locally for the validation of recently proposed distributed hydroacoustic draft tube flow models (in contrast to the lumped approach presented in Section 1.2.1).

The flow swirl breakdown might be attributed to the modification of the relative flow angle at the runner outlet, due to the formation of cavitation on the blades. The collapse of the blade

cavitation presumably causes a sudden reestablishment of the flow swirl in the draft tube, inducing the reformation of the vortex rope. This should be verified or disproved by additional swirl measurements and simultaneous visualizations of the blade cavitation and the vortex rope, for several operating conditions. The passage from stable to unstable should be included in such a survey, in order to verify if the collapsing blade cavitation causes the self-sustained pressure oscillation or the other way round.

Finally, it needs to be determined to what extent the results presented in this work are valid for the actual prototype by attempting to transpose the measured values of quantities such as the pressure and torque fluctuations.

A Flow visualizations

This chapter contains additional flow visualizations for some of the operating points in Table B.1. In parallel, the corresponding wall pressure coefficients are plotted, showing the chosen period from the high speed video.
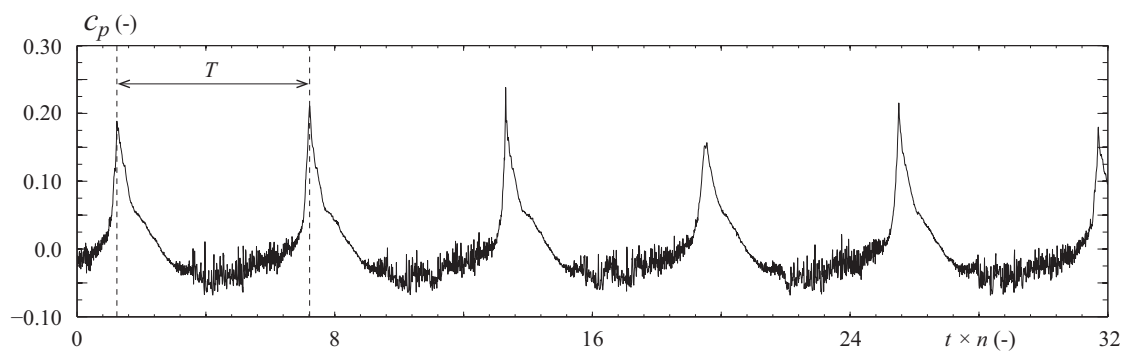
Figure A.1: Wall pressure coefficient at C1N for the visualization in Figure A.3 at OP#2.
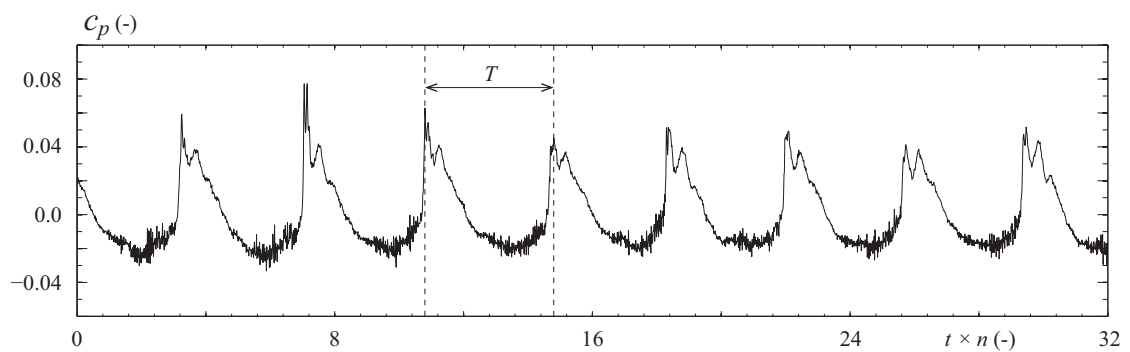
Figure A.2: Wall pressure coefficient at C1N for the visualization in Figure A.4 at OP#5.

Figure A.3: High-speed visualization of the cavitating vortex rope between two pressure peaks at OP#2. The period of the oscillation is $T = 0.711$ s and the time increment between the photos is $\Delta t = 37.4$ ms.
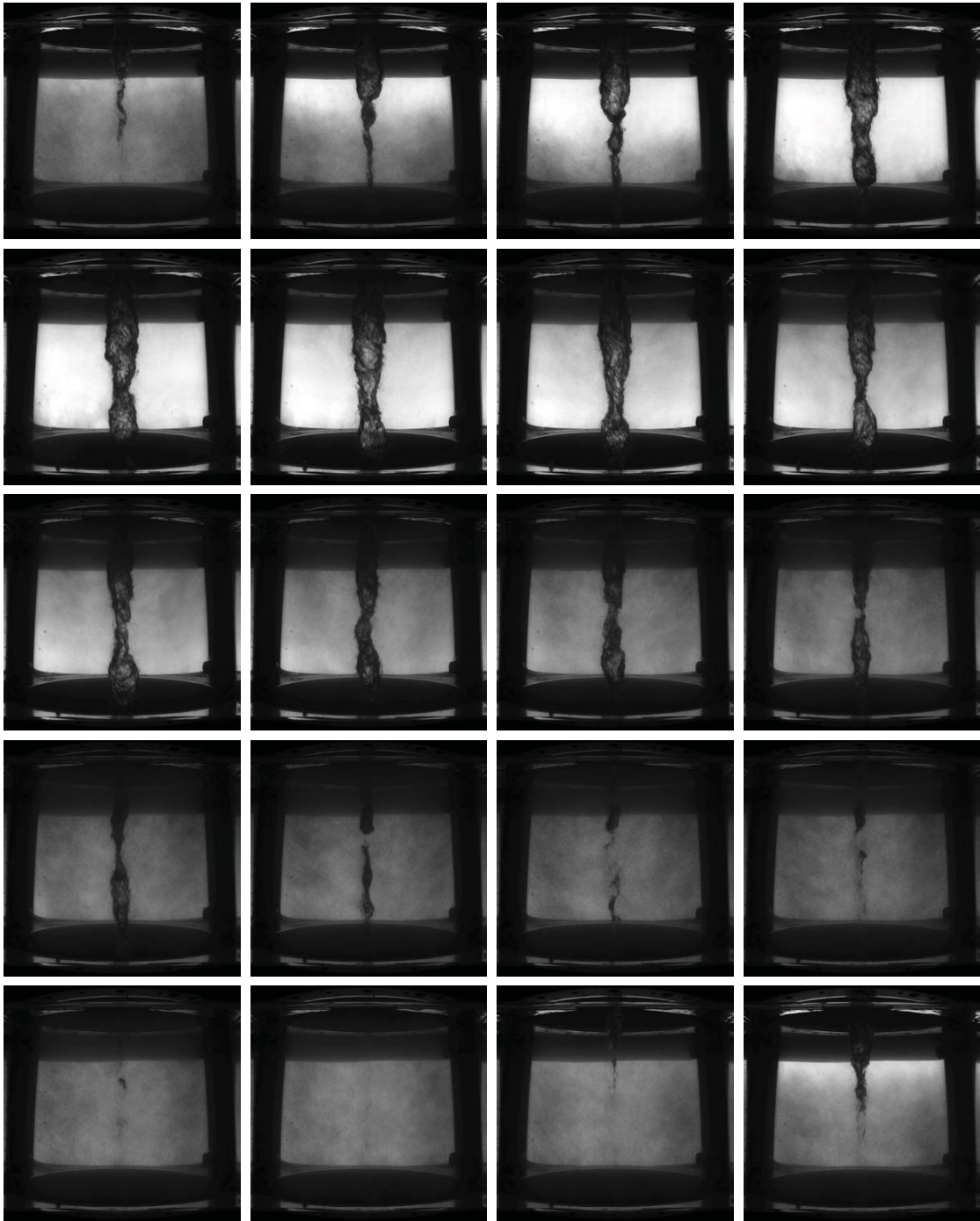
Figure A.4: High-speed visualization of the cavitating vortex rope between two pressure peaks at OP#5. The period of the oscillation is $T = 0.3$ s and the time increment between the photos is $\Delta t = 15.8$ ms.

B List of operating points for reduced scale model tests

Table B.1: Operating conditions for investigation on 1:16 reduced scale physical model.

OP#	n_{ED}	Q_{ED}	σ	N	E	Fr	Q_{ED}/Q_{ED}^* [1]
(-)	(-)	(-)	(-)	(min^{-1})	(J kg^{-1})	(-)	(-)
BEP	0.288	0.200	0.11	800	262.5	8.7	1.000
1	0.288	0.262	0.11	650	173.6	7.1	1.310
2	0.273	0.262	0.10	505	116.0	5.8	1.310
3	0.288	0.253	atm.	800	262.6	8.7	1.265
4	0.273	0.250	atm.	505	115.2	5.8	1.250
5	0.288	0.260	0.11	800	262.7	8.7	1.300
6	0.275	0.268	0.10	505	114.8	5.8	1.340
7	0.273	0.263	0.11	505	116.1	5.8	1.340

_____

[1] Q_{ED}^* is the discharge coefficient at the best efficiency point (BEP)

C List of operating points on the simplified micro-turbine test rig

Table C.1: Operating conditions for investigation on small scale micro-turbine test rig.

OP#	n_{ED}	Q_{ED}	σ	N	E	$Q/Q_{nom.}$[1]
(-)	(-)	(-)	(-)	(min^{-1})	(J kg^{-1})	(-)
A	0.2145	0.2420	0.131	1'000	52.45	2.0
A-1	0.2147	0.2424	1.137	1'000	52.37	2.0
A-2	0.2148	0.2429	0.141	1'000	52.29	2.0
A-3	0.2150	0.2436	0.145	1'000	52.21	2.0
A-4	0.2152	0.2434	0.151	1'000	52.11	2.0
A-5	0.2152	0.2451	0.154	1'000	52.11	2.0
A-6	0.2156	0.2447	0.161	1'000	51.93	2.0
A-7	0.2158	0.2453	0.166	1'000	51.85	2.0
A-8	0.2159	0.2453	0.170	1'000	51.78	2.0
A-9	0.2161	0.2459	0.176	1'000	51.70	2.0
A-10	0.2161	0.2476	0.180	1'000	51.69	2.0
A-11	0.2163	0.2486	0.186	1'000	51.56	2.0
A-12	0.2167	0.2487	0.191	1'000	51.38	2.0
A-13	0.2168	0.2493	0.196	1'000	51.33	2.0
A-14	0.2168	0.2482	0.250	1'000	51.35	2.0
A-15	0.2166	0.2441	0.472	1'000	51.45	2.0

---

[1] The nominal flow rate $Q_{nom.}$ is defined to meet the no-swirl condition in the draft tube, corresponding to a purely axial flow at the turbine outlet. It is $8.33 \cdot 10^{-4}$ m^3s^{-1} for a turbine speed of $N = 1'000$ rpm.

D | Hill chart of the reduced scale model
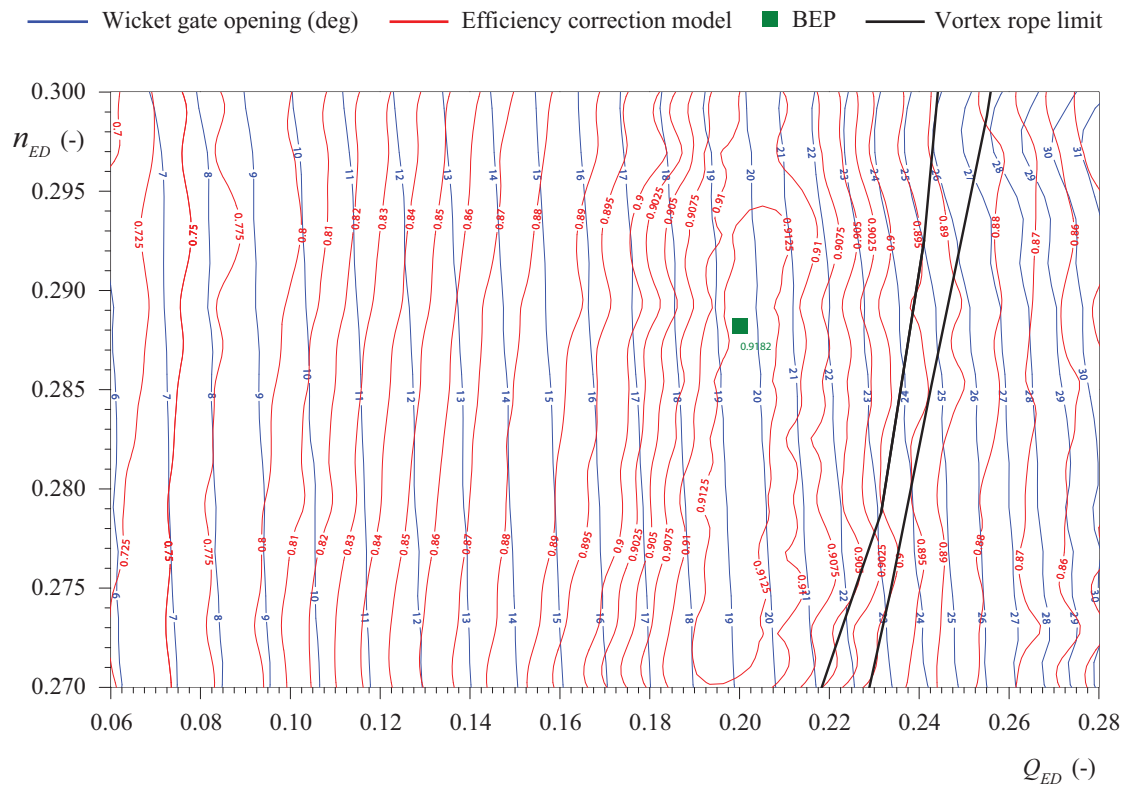
Figure D.1: Hill chart of the reduced scale Francis turbine physical model on the EPFL test rig PF3 as a function of n_{ED} and Q_{ED}.

Bibliography

[1] R.J. Adrian and C.S. Yao. Power spectra of fluid velocities measured by laser doppler velocimetry. *Experiments in Fluids*, 5(1):17–28, 1987.

[2] S. Alligné. *Forced and Self Oscillations of Hydraulic Systems Induced by Cavitation Vortex Rope of Francis Turbines.* PhD thesis, Ecole polytechnique fédérale de Lausanne (EPFL), Laboratory for Hydraulic Machines (LMH), Lausanne, Switzerland, 2011.

[3] S. Alligné, P. Maruzewski, T. Dinh, B. Wang, A. Fedorov, J. Iosfin, and F. Avellan. Prediction of a francis turbine prototype full load instability from investigations on the reduced scale model. In *IOP Conference Series: Earth and Environmental Science*, volume 12, page 012025. IOP Publishing, 2010.

[4] S. Alligné, C. Nicolet, Y. Tsujimoto, and F. Avellan. Cavitation surge modelling in francis turbine draft tube. *Journal of Hydraulic Research*, (ahead-of-print):1–13, 2014.

[5] J. Arpe. *Analyse du champ de pression pariétale d'un diffuseur coudé de turbine Francis.* PhD thesis, Ecole polytechnique fédérale de Lausanne (EPFL), Laboratory for Hydraulic Machines (LMH), Lausanne, Switzerland, 2003.

[6] J. S. Bendat and A. G. Piersol. *Random data: Analysis and measurement procedures.* Wiley, fourth edition, 2010.

[7] D.M. Braisted and C.E. Brennen. Auto-oscillation of cavitating inducers. *Polyphase Flow and Transport Technology*, pages 157–166, 1980.

[8] O. Braun. *Part load flow in radial centrifugal pumps.* PhD thesis, Ecole polytechnique fédérale de Lausanne (EPFL), Laboratory for Hydraulic Machines (LMH), Lausanne, Switzerland, 2009.

[9] O. Braun, A. Taruffi, N Ruchonnet, A. Müller, and F. Avellan. Numerical investigations of the dynamics of the full load vortex rope in a Francis turbine. *Proc. of the 5th Int. Meet. on Cavitation and Dynamic Problems in Hydraulic Machinery and Systems, Lausanne, Switzerland*, 2013.

[10] C. Brennen. Bubbly flow model for the dynamic characteristics of cavitating pumps. *J Fluid Mech*, 89(pt 2):223–240, 1978.

Bibliography

[11] C. Brennen and A.J. Acosta. Theoretical, quasi-static analysis of cavitation compliance in turbopumps. *Journal of Spacecraft and Rockets*, 10(3):175–180, 1973.

[12] C. Brennen and A.J. Acosta. Dynamic transfer function for a cavitating inducer. *Journal of Fluids Engineering, Transactions of the ASME*, 98 Ser 1(2):182–191, 1976.

[13] C. Chen, C. Nicolet, K. Yonezawa, M. Farhat, F. Avellan, and Y. Tsujimoto. One-dimensional analysis of full load draft tube surge. *Journal of Fluids Engineering, Transactions of the ASME*, 130(4):0411061–0411066, 2008.

[14] D. Chirkov, A. Avdyushenko, L. Panov, D. Bannikov, S. Cherny, V. Skorospelov, and I. Pylev. Cfd simulation of pressure and discharge surge in Francis turbine at off-design conditions. In *IOP Conference Series: Earth and Environmental Science*, volume 15, page 032038. IOP Publishing, 2012.

[15] P. Dörfler. Evaluating 1D models for vortex-induced pulsation in Francis turbines. In *Proceedings of the 3rd Meeting IAHR Workgroup on Cavitation and Dynamic Problems in Hydraulic Machinery and Systems, Brno*, 2009.

[16] P. Dörfler, O. Braun, and Y. Tsujimoto. Research on Francis turbine full-load surge. In *Proceedings of the WIMRC 3rd International Cavitation Forum, University of Warwick, UK*, 2011.

[17] P. Dörfler, M. Keller, and O. Braun. Francis full-load surge mechanism identified by unsteady 2-phase cfd. In *IOP Conference Series: Earth and Environmental Science*, volume 12, page 012026. IOP Publishing, 2010.

[18] A. Favrel, C. Landry, A. Müller, and F. Avellan. Experimental identification and study of hydraulic resonance test rig with francis turbine operating at partial load. In *IOP Conference Series: Earth and Environmental Science*, volume 15, page 062064. IOP Publishing, 2012.

[19] Office fédérale de l'énergie (Bundesamt für Energie). *Perspectives énergétiques 2050; résumé*. Schweizerische Bundesverwaltung, Bern, Switzerland, 2013.

[20] Office fédérale de l'énergie (Bundesamt für Energie). *Statistique suisse de l'électricité 2012*. Schweizerische Bundesverwaltung, Bern, Switzerland, 2013.

[21] Renewable Energy Policy Network for the 21st Century. *Renewables 2013; Global status report*. Secretariat of REN21, Paris, France, 2013.

[22] J.P. Franc and J.M. Michel. *Fundamentals of Cavitation*, volume 76 of *Fluid Mechanics and Its Applications*. Springer, 2006.

[23] F.N. Fritsch and R.E. Carlson. Monotone piecewise cubic interpolation. *SIAM Journal on Numerical Analysis*, 17(2):238–246, 1980.

[24] M. Gaster and J.B. Roberts. Spectral analysis of randomly sampled signals. *IMA Journal of Applied Mathematics (Institute of Mathematics and Its Applications)*, 15(2):195–216, 1975.

[25] M. Gaster and J.B. Roberts. Spectral analysis of randomly sampled records by a direct transform. *Proc R Soc London Ser A*, 354(1676):27–58, 1977.

[26] A. K. Gupta, D. G. Lilley, and N. Syred. *Swirl Flows*. Abacus Press, UK, 1984.

[27] IEC standards. 60193: Hydraulic Turbines, Storage Pumps and Pump-Turbines - Model Acceptance Tests, International Electrotechnic Commission, 2nd Edition, 1999.

[28] T. Jacob. Francis turbine surge: discussion and data base. In *Proc. of the 18th IAHR Symposium, Valencia, Spain*, 1996.

[29] T. Jacob, J. Prenat, and D. Maria. Dynamic behavior at high load of a francis water turbine. model/ prototype comparison [comportement dynamique d'une turbine francis a forte charge. comparaisons modèle-prototype]. *Houille Blanche*, (3-4):293–300, 1988.

[30] T. Jacob, J.E. Prenat, G. Vullioud, and B. Lopez Araguas. Surging of a 140 mw francis turbine at high load, analysis and solution. In *Proc. of the 16th IAHR Symposium, Saō Paolo, Brazil*, 1992.

[31] A. Jenkins. Self-oscillation. *Physics Reports*, 525(2):167–222, 2013.

[32] A. Kashima, P. J. Lee, M. S. Ghidaoui, and M. Davidson. Experimental verification of the kinetic differential pressure method for flow measurements. *Journal of Hydraulic Research*, 51(6):634–644, 2013.

[33] J. Koutnik, C. Nicolet, G. A. Schohl, and F. Avellan. Overload surge event in a pumped storage power plant. In *Proc. of the 23th IAHR Symposium on Hydraulic Machinery and Systems, Yokohama, Japan*, 2006.

[34] J. Koutnik and L. Pulpitel. Modeling of the francis turbine full-load surge. *Modeling, Testing and Monitoring for Hydro Power Plants, Lausanne*, 1996.

[35] P. Kuibin, V. Okulov, R. Susan-Resiga, and S. Muntean. Validation of mathematical models for predicting the swirling flow and the vortex rope in a Francis turbine operated at partial discharge. In *IOP Conference Series: Earth and Environmental Science*, volume 12, page 012051. IOP Publishing, 2010.

[36] P. Kuibin, I. Pylev, and A. Zakharov. Two-phase models development for description of vortex-induced pulsation in Francis turbine. In *IOP Conference Series: Earth and Environmental Science*, volume 15, page 022001. IOP Publishing, 2012.

[37] H. Lamb. *Hydrodynamics*. Cambridge University Press, 6th edition, 1932.

[38] C. Landry, C. Nicolet, A. Bergant, A. Müller, and F. Avellan. Modeling of unsteady friction and viscoelastic damping in piping systems. In *IOP Conference Series: Earth and Environmental Science*, volume 15, page 052030. IOP Publishing, 2012.

Bibliography

[39] S. Lawrence Marple. Computing the discrete-time analytic signal via fft. *IEEE Transactions on Signal Processing*, 47(9):2600–2603, 1999.

[40] N.J. Lawson, A. Guerre, J.-L. Liow, and M. Rudman. Experimental and numerical comparisons of the break-up of a large bubble. *Experiments in Fluids*, 26(6):524–534, 1999.

[41] A. Müller, S. Alligné, F. Paraz, C. Landry, and F. Avellan. Determination of hydroacoustic draft tube parameters by high speed visualization during model testing of a francis turbine. *Proc. of the 4th Int. Meet. on Cavitation and Dynamic Problems in Hydraulic Machinery and Systems, Belgrade, Serbia*, 2011.

[42] A. Müller, A. Bullani, M. Dreyer, S. Roth, A. Favrel, C. Landry, and F. Avellan. Interaction of a pulsating vortex rope with the local velocity field in a Francis turbine draft tube. In *IOP Conference Series: Earth and Environmental Science*, volume 15, page 032040. IOP Publishing, 2012.

[43] A. Müller, M. Dreyer, N. Andreini, and F. Avellan. Draft tube discharge fluctuation during self-sustained pressure surge: fluorescent particle image velocimetry in two-phase flow. *Experiments in Fluids*, 54(4):1–11, 2013.

[44] C. Nicolet. *Hydroacoustic Modelling and Numerical Simulation of Unsteady Operation of Hydroelectric Systems*. PhD thesis, Ecole polytechnique fédérale de Lausanne (EPFL), Laboratory for Hydraulic Machines (LMH), Lausanne, Switzerland, 2007.

[45] M. Nishi, S. Matsunaga, T. Kubota, and Y. Senoo. Flow regimes in an elbow-type draft tube. In *Proc. of the 11th IAHR Symposium on Hydraulic Machinery and Systems, Amsterdam, The Netherlands*, pages 1–13, 1982.

[46] B. W. Oppenheim and S. Rubin. Advanced pogo stability analysis for liquid rockets. *Journal of Spacecraft and Rockets*, 30(3):360–373, 1993.

[47] C.W. Oseen. *Über Wirbelbewegung in einer reibenden Flüssigkeit*. Arkiv för matematik, astronomi och fysik. Almqvist & Wiksells, 1911.

[48] N. Otsu. Threshold selection method from gray-level histograms. *IEEE Trans Syst Man Cybern*, SMC-9(1):62–66, 1979.

[49] A. Ouahabi, C. Depollier, L. Simon, and D. Koume. Spectrum estimation from randomly sampled velocity data [ldv]. *Instrumentation and Measurement, IEEE Transactions on*, 47(4):1005–1012, 1998.

[50] O. Pacot. *Large Scale Computation of the Rotating Stall in a Pump-Turbine using an Overset Finite Element Large Eddy Simulation Numerical Code*. PhD thesis, Ecole polytechnique fédérale de Lausanne (EPFL), Laboratory for Hydraulic Machines (LMH), Lausanne, Switzerland, 2014.

[51] European Parliament and Council of the European Union. Directive 2009/28/EC. *Official Journal of the European Union*, 52:L140/16–62, 2009.

[52] J. E. Prenat and T. Jacob. High load behaviour of a Francis turbine model and scale effects. In *Proc. of the 13th IAHR Symposium, section on hydraulic machinery and cavitaion : Progress in Technology, Montréal, Canada*, volume 2, pages 77.1–77.15, 1986.

[53] W. J. Rheingans. Power swings in hydroelectric power plants. *Transactions of the ASME*, 62:171–184, 1940.

[54] S. Rubin. Longitudinal instability of liquid rockets due to propulsion feedback /POGO/. *Journal of Spacecraft and Rockets*, 3:1188–1195, August 1966.

[55] S. Rubin. An interpretation of transfer function data for a cavitating pump. In *Proceedings of the 40th AIAA Joint Propulsion Conference*, 2004.

[56] P. Rudolf and D. Štefan. Decomposition of the swirling flow field downstream of Francis turbine runner. In *IOP Conference Series: Earth and Environmental Science*, volume 15, page 062008, 2012.

[57] J. Stoer, R. Bulirsch, R. Bartels, W. Gautschi, and C. Witzgall. *Introduction to Numerical Analysis*. Texts in Applied Mathematics. Springer, 2002.

[58] R. Susan-Resiga, G.D. Ciocan, I. Anton, and F. Avellan. Analysis of the swirling flow downstream a Francis turbine runner. *Journal of Fluids Engineering*, 128(1):177–189, 2006.

[59] R. Susan-Resiga, S. Muntean, F. Avellan, and I. Anton. Mathematical modelling of swirling flow in hydraulic turbines for the full operating range. *Applied Mathematical Modelling*, 35(10):4759–4773, 2011.

[60] R. Susan-Resiga, S. Muntean, P. Stein, and F. Avellan. Axisymmetric swirling flow simulation of the draft tube vortex in Francis turbines at partial discharge. *International Journal of Fluid Machinery and Systems*, 2(4):295–302, 2009.

[61] Y. Tsujimoto, K. Kamijo, and Y. Yoshida. A theoretical analysis of rotating cavitation in inducers. *Journal of fluids engineering*, 115(1):135–141, 1993.

[62] Y. Tsujimoto, S. Watanabe, K. Kamijo, and Y. Yoshida. A nonlinear calculation of rotating cavitation in inducers. *Journal of fluids engineering*, 118(3):589–594, 1996.

[63] Y. Tsujimoto, Y. Yoshida, Y. Maekawa, S. Watanabe, and T. Hashimoto. Observations of oscillating cavitation of an inducer. *Journal of Fluids Engineering, Transactions of the ASME*, 119(4):775–781, 1997.

[64] P. Welch. The use of fast fourier transform for the estimation of power spectra: a method based on time averaging over short, modified periodograms. *Audio and Electroacoustics, IEEE Transactions on*, 15(2):70–73, 1967.

[65] E.B. Wylie, V.L. Streeter, and L. Suo. *Fluid transients in systems*. Prentice Hall Englewood Cliffs, NJ, 1993.

Bibliography

[66] K. Yamamoto, A. Müller, T. Ashida, K. Yonezawa, F. Avellan, and Y. Tsujimoto. Experimental method for the evaluation of the dynamic transfer matrix using pressure transducers. Article under revision at the Journal of Hydraulic Research.

[67] K. Yamamoto and Y. Tsujimoto (supervisor). Unsteady behavior of cavitating draft tube flow. MSc thesis, Osaka University, Graduate School of Engineering Science, Japan, 2013.

[68] F.R. Young. *Cavitation*. McGraw-Hill, 1989.

Curriculum Vitae

Andres Müller
Mechanical engineer
Born in 1983, Swiss citizen
Living in Lausanne, Switzerland
andres.mueller@a3.epfl.ch

Education

2010 – 2014	**PhD** École polytechnique fédérale de Lausanne (EPFL), Switzerland.
2006 – 2008	**Master of Science MSc** (mechanical engineering) École polytechnique fédérale de Lausanne (EPFL), Switzerland.
2002 – 2006	**Bachelor of Science BSc** (mechanical engineering) École polytechnique fédérale de Lausanne (EPFL), Switzerland.

Professional Experience

2010 – 2014	**Doctoral assistant –** EPFL Laboratory for Hydraulic Machines (LMH). Experimental characterization of oscillatory flow phenomena involving cavitation in hydraulic machines. Participation in teaching activities as an assistant and supervision of master theses.
2008 – 2010	**Development and test engineer** – ABB Schweiz AG, Electrical Machines, Birr, Switzerland. Rotordynamics of high-speed electrical machines < 25 MW (simulation and measurement). Mechanical calculations, machine failure analysis and diagnostics. Project management.
2008 (3 months)	**Scientific assistant –** EPFL Laboratory for Industrial Energy Systems (LENI). Exp. investigation of local physical and electrochemical properties in Solid Oxide Fuel Cells.

Trainee ships and stays abroad

2014 (2 months)	**Visiting research fellow –** University of Osaka, Toyonaka, Japan (Tsujimoto Laboratory). Experimental characterization of unsteady, cavitating draft tube flow in a micro-turbine.
2007 (6 weeks)	**Trainee** – International Rotorcraft R&D Hub, Konkuk University, Seoul, South Korea. Computational flight dynamics.
2006 (10 months)	**Exchange student** – Kungliga Tekniska Högskolan (KTH), Stockholm, Sweden. Department of Aeronautical and Vehicle Engineering, Department of Energy Technology.

Extracurricular interests and activities

- Extensive travelling across Europe, the Middle East, Asia, Australia, North and South America.
- Keen reader of national and international newspapers, journals, periodicals and books.
- Languages, photography, sports.
- Member of the organizing committee of the Festival Balélec between 2007 and 2011, President in 2011.

List of publications

Journal papers

A. Müller, M. Dreyer, N. Andreini and F. Avellan (2013) Draft tube discharge fluctuations during self-sustained pressure surge: fluorescent particle image velocimetry in two-phase flow. *Experiments in Fluids,* volume 54, issue 4, pages 1-11.

K. Yamamoto, A. Müller, T. Ashida, K. Yonezawa, F. Avellan and Y. Tsujimoto (2014) Experimental method for the evaluation of the dynamic transfer matrix using pressure transducers. *Journal of Hydraulic Research* (article under revision).

Z. Wuillemin, A. Nakajo, A. Müller, A. J. Schuler, S. Diethelm, J. Van Herle and D. Favrat (2009) Locally-resolved study of degradation in a SOFC repeat-element. *ECS transactions,* volume 25, number 2, pages 457-466.

Conference papers

A. Müller, A. Favrel, C. Landry, K. Yamamoto, O. Braun and F. Avellan (2014) On the physical mechanisms governing self-excited pressure surge in Francis turbines. *Proceedings of the 27th International Symposium on Hydraulic Machinery and Systems*, Montreal, Canada (article submitted).

A. Müller, A. Bullani, M. Dreyer, S. Roth, A. Favrel, C. Landry and F. Avellan (2012) Interaction of a pulsating vortex rope with the local velocity field in a Francis turbine draft tube. *IOP Conference Series: Earth and Environmental Science*, vol. 15, page 032040.

A. Müller, S. Alligné, F. Paraz, C. Landry and F. Avellan (2011) Determination of hydroacoustic draft tube parameters by high-speed visualization during model testing of a Francis turbine. *Proceedings of the 4th International Meeting on Cavitation and Dynamic Problems in Hydraulic Machinery and Systems*, Belgrade, Serbia.

A. Favrel, C. Landry, A. Müller, K. Yamamoto and F. Avellan (2014) Hydro-acoustic resonance behavior in presence of a precessing vortex rope: the observation of a lock-in effect at partial load Francis turbine operation. *Proceedings of the 27th International Symposium on Hydraulic Machinery and Systems*, Montreal, Canada (article submitted).

C. Landry, A. Favrel, A. Müller, C. Nicolet, K. Yamamoto and F. Avellan (2014) Experimental investigation of the local wave speed in a draft tube with cavitation vortex rope. *Proceedings of the 27th International Symposium on Hydraulic Machinery and Systems*, Montreal, Canada (article submitted).

K. Yamamoto, A. Müller, A. Favrel, C. Landry and F. Avellan (2014) Pressure measurements and high-speed visualizations of the cavitation phenomena at deep part load condition in a Francis Turbine. *Proceedings of the 27th International Symposium on Hydraulic Machinery and Systems*, Montreal, Canada (article submitted).

A. Favrel, C. Landry, A. Müller and F. Avellan (2012) Experimental identification and study of hydraulic resonance test rig with Francis turbine operating at partial load. *IOP Conference Series: Earth and Environmental Science,* vol. 15, page 062064.

C. Landry, C. Nicolet, A. Bergant, A. Müller and F. Avellan (2012) Modeling of unsteady friction and viscoelastic damping in piping systems. *IOP Conference Series: Earth and Environmental Science*, vol. 15, page 052030.

C. Landry, S. Alligné, V. Hasmatuchi, S. Roth, A. Müller and F. Avellan (2011) Non-linear stability analysis of a reduced scale model pump-turbine at off-design operation. *Proceedings of the 4th International Meeting on Cavitation and Dynamic Problems in Hydraulic Machinery and Systems*, Belgrade, Serbia.

Z. Wuillemin, A. Müller, A. Nakajo, N. Autissier, S. Diethelm, M. Molinelli, J. Van Herle and D. Favrat (2008) Investigation of Local Electrochemical Performance and Local Degradation in an Operating Solid Oxide Fuel Cell. *8th European Fuell Cell Forum*, Lucerne, Switzerland.

Presentations and seminars

O. Braun, A. Taruffi, N. Ruchonnet, A. Müller and F. Avellan (2013) Numerical investigations of the dynamics of the full load vortex rope in a Francis turbine. *Proceedings of the 5th International Meeting on Cavitation and Dynamic Problems in Hydraulic Machinery and Systems*, Lausanne, Switzerland.